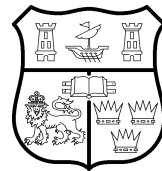


Design and Development of a Catheter Actuation System

Fabian Trauzettel
STUDENT No. 116223196
BE Biomedical Engineering



UNIVERSITY COLLEGE CORK

SCHOOL OF ENGINEERING

**Thesis submitted for the degree of
Master of Engineering Science**

July 2018

Head of School: Prof. William Marnane

Supervisors: Pádraig Cantillon-Murphy, Ph.D.

Contents

List of Figures	iv
List of Tables	xi
Acknowledgements	xiii
Journal and conference publications	xiv
Introduction	xv
1 Literature review	1
1.1 Catheter steering mechanisms	1
1.2 Manually-actuated electrophysiology catheters	2
1.2.1 Lever-couple handles	2
1.2.2 Rotational-style handles	3
1.2.3 Plunger-style handles	4
1.3 Manually-actuated electromagnetic navigation bronchoscopy (ENB) systems	5
1.3.1 SuperDimesion iLogic catheter	8
1.3.2 The View™catheter, Veran medical technologies	9
1.4 Other manual catheter handle designs	9
1.5 Robotic catheter and surgical systems	12
1.6 Conclusion	17
2 Catheter design and modelling	20
2.1 Catheter specification	20
2.1.1 Steering	21
2.1.2 Position sensing	22
2.2 Catheter steering model	24
2.2.1 Single-tendon deflection	24
2.2.2 Multiple-tendon deflection	26
2.2.3 Experimental catheter	30
2.2.3.1 Centroid calculation	30
2.2.4 Catheter model limitations and assumptions	35
2.2.4.1 Axial tendon elongation under load	35

2.2.4.2 Lateral tendon shrinkage under load	37
3 Construction of a catheter testing apparatus	39
3.1 Actuation elements	39
3.2 Tendon force sensing	41
3.2.1 Load cell electronics	42
3.2.2 Load cell calibration	43
3.3 Tip angle measurement	46
3.3.1 Webcam-based tip angle measurement	47
3.3.2 EM-tracked tip angle measurement	51
3.4 Software	55
3.4.1 Graphical user interface (GUI)	56
3.4.2 PID controller	58
4 Catheter testing	60
4.1 Single-tendon loading	60
4.1.1 Method	60
4.1.2 Results	62
4.1.3 Catheter 1	62
4.1.4 Catheter 2	68
4.1.5 Error compensation	72
4.1.6 Tendon load - displacement hysteresis	75
4.1.7 Tip angle - loading relationship	77
4.1.8 Experiment variability	80
4.1.9 Mechanical constraints	80
4.1.10 Limitations	82
4.2 Multi-tendon loading	82
4.2.1 Methods	82
4.2.2 Multi-tendon results	83
4.2.3 Multi-tendon test observations	86

5 Catheter handle design	91
5.1 Preliminary catheter handle design	91
5.2 Catheter handle design A	94
5.2.1 Design A observations	95
5.3 Catheter handle design B	96
5.3.1 Design B observations	100
5.4 Catheter handle design C	101
5.4.1 Design C observations	103
6 Pre-clinical investigation	105
7 Conclusion	109
A Data	111
A.1 Catheter 1 single-tendon deflection	112
A.2 Catheter 2 single-tendon deflection	116
A.3 Catheter 1 hysteresis	120
A.4 Catheter 2 hysteresis	122
A.5 Catheter 1 tip angle - load relationship	124
A.6 Catheter 2 tip angle - load relationship	126
A.7 Multi-tendon error plots	128
B Code	130

List of Figures

1.1	Boston Scientific Blazer Dx-20	3
1.2	US Patent 5,364,351 Fig. 1 - Heinzelman and Brooks, 1992 [12]	3
1.3	Boston Scientific Radia electrophysiology catheter	4
1.4	Boston Scientific Polaris X electrophysiology catheter	4
1.5	Boston Scientific Orbiter ST electrophysiology catheter	5
1.6	Flowchart of a typical ENB procedure	6
1.7	Screenshot from 3DSlicer [20] during an ENB procedure in a live animal model	7
1.8	Covidien / SuperDimension iLogic catheter handle	8
1.9	Covidien / SuperDimension iLogic handle, disassembled to show the actuation mechanism	9
1.10	The View™catheter, Veran medical Technologies	9
1.11	US Patent 6,007,531 (figure 3A-D, Dec. 1999)	10
1.12	US Patent US20100004591A1 (figure 8), 2008 [25]	11
1.13	US patent US20130253469A1 (figure 1), 2013 [26]	11
1.14	Motion rig developed by Ataollahi et al	13
1.15	Motion rig developed by Ataollahi et al, with catheter and adapter in place	13
1.16	CAD model of the catheter connector built by Ataollahi et al	13
1.17	Artisan Extend catheter, attached to a Sensei X, Hansen Medical	14
1.18	US patent D441,076 S - April 2001	15
1.19	Older version Da Vinci connector system, as implemented on the Da Vinci Si.	15
1.20	Da Vinci Xi 5-spool connector	16
1.21	Catheter Robotics' Amigo drive element with attached Boston Scientific Blazer-series catheter	16
1.22	Stereotaxis Niobe and V Drive assembled in a catheter laboratory	17
2.1	Cross-sectional view of the catheter shaft. All dimensions in mm.	21
2.2	Detailed view of the catheter tendons. All dimensions in mm. Figure not to scale.	22

2.3 Close-up photo of the proximal end of the catheter, showing the working channel (center), the two twisted-pair EM sensor wires as well as the four stainless steel tendons.	23
2.4 Longitudinal section of the catheter in relaxed (left), partially deflected (center) and fully deflected state (right)	24
2.5 Simple two (left) and four-tendon (right) catheters. Fig. 2.4 shows the elevation of a two-tendon catheter, while Fig. 2.6 shows the end view of a four-tendon catheter.	26
2.6 Transverse section of a basic four-tendon catheter. The large arrow shows the plane of deflection. Each tendon is perpendicularly projected on to the plane of deflection along the dotted lines.	27
2.7 A plot of the tendon deflection at $\theta = 90^\circ$ and $r_A = r_B = r_C = r_D = 1.5\text{mm}$	29
2.8 Cross-section of catheter, annotated with all dimensions used to locate the section centroid, as well as the centroids of each segment the section was decomposed into (blue dots). Solid areas are shaded grey.	31
2.9 Section of the experimental catheter supplied by Teleflex OEM. Note that the centroid is displaced upwards by 0.041 mm due to the asymmetry of the section.	33
2.10 A plot of the tendon deflection at $\theta = 90^\circ$	34
2.11 Plot of tendon elongation vs force applied	37
3.1 Photograph (left) and rendering (right) showing the actuation assembly	39
3.2 Closeup of the RAMPS 1.4 board used to drive the stepper motors. . .	40
3.3 Rendered image of the whole actuation and force sensing assembly - Stepper motors and transmission on the left, linear motion axis, load cells and tendon attachment clamps on the right.	41
3.4 Closeup photograph showing the load cell and tendon clamp. The leadscrew is visible inside the aluminium profile slot.	41
3.5 INA122 circuit used to amplify the load cell signal.	42
3.6 INA122 circuit used to amplify the load cell signal.	43
3.7 Plot of ADC reading vs. force applied to load cell	44
3.8 Flowchart of the linear interpolation logic used to convert ADC readings to force values	45
3.9 Image of the testing rig machine vision setup, render on the left, photograph on the right. Only the X camera was used to acquire data. . . .	47
3.10 A closeup of the catheter tip with machine vision markers.	47

3.11 A screenshot of the machine vision GUI, showing the original image, the binarised image, the tip angle readout and the thresholding controls	48
3.12 Flowchart of the OpenCV tip angle-finding algorithm	50
3.13 Closeup photograph of a catheter tip with two NDI 610099 5 degree-of-freedom sensors attached.	51
3.14 Graphic showing the interactions between individual testing rig elements	55
3.15 Screenshot of the testing rig's GUI in use	56
3.16 Flowchart of the PID control algorithm - concept on the left, software implementation on the right	59
4.1 Catheter clamped into position on testing rig	60
4.2 Graph of real, predicted and compensated predicted tendon displacement vs. tip deflection angle for Catheter 1, Tendon A	64
4.3 Displacement prediction error for Catheter 1, Tendon A	64
4.4 Graph of real, predicted and compensated predicted tendon displacement vs. tip deflection angle for Catheter 1, Tendon B	65
4.5 Displacement prediction error for Catheter 1, Tendon B	65
4.6 Graph of real, predicted and compensated predicted tendon displacement vs. tip deflection angle for Catheter 1, Tendon C	66
4.7 Displacement prediction error for Catheter 1, Tendon C	66
4.8 Graph of real, predicted and compensated predicted tendon displacement vs. tip deflection angle for Catheter 1, Tendon D	67
4.9 Displacement prediction error for Catheter 1, Tendon D	67
4.10 Graph of real, predicted and compensated predicted tendon displacement vs. tip deflection angle for Catheter 2, Tendon A	68
4.11 Displacement prediction error for Catheter 2, Tendon A	69
4.12 Graph of real, predicted and compensated predicted tendon displacement vs. tip deflection angle for Catheter 2, Tendon B	69
4.13 Displacement prediction error for Catheter 2, Tendon B	70
4.14 Graph of real, predicted and compensated predicted tendon displacement vs. tip deflection angle for Catheter 2, Tendon C	70
4.15 Displacement prediction error for Catheter 2, Tendon C	71
4.16 Graph of real, predicted and compensated predicted tendon displacement vs. tip deflection angle for Catheter 2, Tendon D	71

4.17 Displacement prediction error for for Catheter 2, Tendon D	72
4.18 Force-Displacement graph of Catheter 1, Tendon A showing the data points, regression curves and area between loading and unloading curves	76
4.19 A plot of tendon load over tip angle for catheter 1, tendon A. Note the distinct loading and unloading curves.	78
4.20 Standard ER collet with end mill showing the distribution of clamping points on the cylindrical face of an end mill. Image courtesy of CTC Engineering Ltd, Hong Kong	81
4.21 Overview of the Testing assembly showing the catheter clamp, guide rod and catheter supports	81
4.22 Tendon forces over time	84
4.23 Tendon displacement over time	84
4.24 Tip Deflection over time	85
4.25 Direction of tip deflection over time	85
4.26 Polar plot showing the movement of the distal tip during multi-tendon testing - the radial axis shows the magnitude of deflection θ , while the directional axis shows the direction of tip deflection α	86
4.27 A plot of the data showing the correlation between the predicted and real displacements	87
4.28 Tendon displacement prediction error over time	88
4.29 A plot of prediction error over tendon force.	89
4.30 Axial view of the tracking data showing the movement of sensors A and B.	89
 5.1 Concept 1 designed by The Design Factor. (Rendering courtesy of The Design Factor)	92
5.2 Concept 2 designed by The Design Factor. This version features a straight handle with a clip to attach the handle to the bronchoscope. (Rendering courtesy of The Design Factor)	92
5.3 Concept 3 designed by The Design Factor. To facilitate easier insertion of tools into the working lumen, the handle is angled. (Rendering courtesy of The Design Factor)	93
5.4 Concept 4 designed by The Design Factor. This version is both angled and features a scope attachment clip. (Rendering courtesy of The Design Factor)	93
5.5 Handle Design A : bending handle	94

5.6 A plot of theoretical tendon displacement over handle deflection	95
5.7 Displacement diagram of the cam ring.	96
5.8 Very early design exploration	97
5.9 Scope attachment improvements	97
5.10 Cross-section of the cam ring showing the diagonal cam profile and the rounded outer surface.	98
5.11 CAD image of the the catheter handle showing the cam ring (grey), followers (beige), return springs, and scope clip (blue) inside the handle (transparent grey).	98
5.12 Photograph of the internals of the catheter handle showing the tendons, two sensor cables, and PTFE bowden tubes.	99
5.13 Annotated photograph of handle internals	99
5.14 Render of the final design iteration of handle design B.	100
5.15 Section of handle design C, showing the rack and pinion mechanisms. The catheter is mounted into the handle at an angle at the bottom of the handle.	101
5.16 Side view of one of the geared spools used in design C. Note the V-groove which centers the tendon on the spool.	102
5.17 Photograph of design C in the hand.	103
5.18 Variant of design C	104
6.1 Overview of the experimental procedure.	106
6.2 Screenshot of the CustusX navigation screen during navigation to a tumour in the lower right lobe. The bronchoscope view, segmented airway with real-time position, CT slices and CT volume render are all visible.	107
6.3 CT slice showing the embolisation coil (visible as a bright object in the centre of the image), the shortest distance to the tumour model (d5), the distance to the centre of the tumour model(d4), and the distance to the opposite side of the tumour model (d6).	107
A.1 Catheter 1, tendon A raw data plots	112
A.2 Catheter 1, tendon B raw data plots	113
A.3 Catheter 1, tendon C raw data plots	114
A.4 Catheter 1, tendon D raw data plots	115
A.5 Catheter 2, tendon A raw data plots	116

A.6 Catheter 2, tendon B raw data plots	117
A.7 Catheter 2, tendon C raw data plots	118
A.8 Catheter 2, tendon D raw data plots	119
A.9 Force-Displacement graph of Catheter 1, Tendon A showing the data points, regression curves and area between loading and unloading curves	120
A.10 Force-Displacement graph of Catheter 1, Tendon B showing the data points, regression curves and area between loading and unloading curves	120
A.11 Force-Displacement graph of Catheter 1, Tendon C showing the data points, regression curves and area between loading and unloading curves	121
A.12 Force-Displacement graph of Catheter 1, Tendon D showing the data points, regression curves and area between loading and unloading curves	121
A.13 Force-Displacement graph of Catheter 2, Tendon A showing the data points, regression curves and area between loading and unloading curves	122
A.14 Force-Displacement graph of Catheter 2, Tendon B showing the data points, regression curves and area between loading and unloading curves	122
A.15 Force-Displacement graph of Catheter 2, Tendon C showing the data points, regression curves and area between loading and unloading curves	123
A.16 Force-Displacement graph of Catheter 2, Tendon D showing the data points, regression curves and area between loading and unloading curves	123
A.17 A plot of tendon load over tip angle for catheter 1, tendon A. Note the distinct loading and unloading curves.	124
A.18 A plot of tendon load over tip angle for catheter 1, tendon B. Note the distinct loading and unloading curves.	124
A.19 A plot of tendon load over tip angle for catheter 1, tendon C. Note the distinct loading and unloading curves.	125
A.20 A plot of tendon load over tip angle for catheter 1, tendon D. Note the distinct loading and unloading curves.	125
A.21 A plot of tendon load over tip angle for catheter 2, tendon A. Note the distinct loading and unloading curves.	126

A.22 A plot of tendon load over tip angle for catheter 2, tendon B. Note the distinct loading and unloading curves.	126
A.23 A plot of tendon load over tip angle for catheter 2, tendon C. Note the distinct loading and unloading curves.	127
A.24 A plot of tendon load over tip angle for catheter 2, tendon D. Note the distinct loading and unloading curves.	127
A.25 Plots of real and predicted deflection, as well as the prediction error over time	128
A.26 Plots of displacement prediction error vs: direction of tip deflection, magnitude of tip deflection, individual tendon force, and total tendon force.	129

List of Tables

1.1	Summary of reviewed catheter systems	19
2.1	List of NDI EM tracking sensors available for purchase [40]	23
2.2	Segment areas (A_i), segment centroid positions (C_{i_x}, C_{i_y}), and weighted segment centroid positions	32
3.1	load cell calibration data	44
4.2	Catheter 1 key data	62
4.1	List of figures for single-tendon testing	63
4.3	Catheter 2 key data	68
4.4	Prediction Error data	73
4.5	Mean Absolute Error data before and after error compensation	75
4.6	Area of hysteresis curves	77
4.7	Polynomial regression coefficients for tendon loading curves. Matching tendons in separate catheters are grouped to facilitate easy comparison.	79
4.8	Polynomial regression coefficients for tendon unloading curves. Matching tendons in separate catheters are grouped to facilitate easy comparison.	79
4.9	Tendon displacement prediction errors	88
6.1	Closest distance between tumour model and embolisation coil position	108

I, Fabian Trauzettel, certify that this thesis is my own work and I have not obtained a degree in this university or elsewhere on the basis of the work submitted in this thesis.

Fabian Trauzettel

Acknowledgements

I'd like to thank everyone who has lent me their support and knowledge over past 22 months, both at UCC and IHU, with special thanks to:

Pádraig Cantillon-Murphy, for his hard work keeping me focused on my project and for giving me this incredible chance;

Alex Jaeger, for his technical support, fantastically nerdy conversations and being a good friend;

Liane Trauzettel, for being her usual, infinitely giving self;

Silvana Peretta, Bernard Dallemande and Lee Swanström, for their advice, collaboration and vast combined experience;

The IRCAD / IHU staff for their assistance in this project and several others;

Michael O'Shea and **Timothy Power** at UCC for their top-notch fabrication and machining skills, and

The IRCAD / IHU fellows for always being there to bounce ideas off of and share a beer with.

Journal and conference publications

Trauzettel, F., Jaeger, H. A., & Cantillon-Murphy, P., **Mechanical catheter navigation with electromagnetic tracking to peripheral airway targets**, Conference: *Annual Meeting of the International Society for Medical Innovation and Technology (iSMIT)*, Nov. 2017, Torino, Italy

Cantillon-Murphy, P., Trauzettel, F., & Jaeger, H. A., **Electromagnetic instrument tracking in the hybrid OR**, Conference: *Surgetica*, Nov. 2017, Strasbourg, France

Jaeger, H. A., Franz, A. M., O'Donoghue, K., Seitel, A., Trauzettel, F., Maier-Hein, L., & Cantillon-Murphy, P. (2017). **Anser EMT: the first open-source electromagnetic tracking platform for image-guided interventions.**, *International Journal of Computer Assisted Radiology and Surgery*, 12(6), 1059–1067.

<https://doi.org/10.1007/s11548-017-1568-7> [Accessed: 2018-07-05]

Jaeger, H. A., Trauzettel, F., Fagertun Hofstad, E., Kennedy, M. P., Leira, H. O., Langø, T., & Cantillon-Murphy, P., **Open source airway navigation: initial experiences with CustusX and Anser EMT.**, Conference: *Annual Meeting of the International Society for Medical Innovation and Technology (iSMIT)*, Nov. 2017, Torino, Italy

McCarthy, C., Kanterman, I., Trauzettel, F., Goetz, A.-A., Jaeger, H. A., Colvard, B., & Cantillon-Murphy, P., **Autonomous Balloon Management for Endovascular Occlusion.**, Conference: *Annual Meeting of the International Society for Medical Innovation and Technology (iSMIT)*, Nov. 2017, Torino, Italy

Jaeger, H. A., Trauzettel, F., Nardelli, P., Davrieux, F., Fagertun Hofstad, E., Leira, H. O., ... Cantillon-Murphy, P., **Peripheral tumour targeting using open-source virtual bronchoscopy with electromagnetic tracking: a multi-user pre-clinical study.** *Minimally Invasive Therapy & Allied Technologies.*, 2018, In press.

Introduction

Lung cancer represents one of the most commonly-diagnosed and lethal forms of cancer in the world. The American Cancer Society estimates that about 234,000 patients will be diagnosed in the US this year, and approximately 154,000 Americans are expected to die of lung cancer in the same period. This makes lung cancer more lethal than colon, breast and prostate cancers combined [1]. The disease is divided in two main branches; small cell lung cancer (SCLC) and non-small cell lung cancer (NSCLC). NSCLC takes the lion's share of incidences, totalling about 85% of diagnoses [2]. Since NSCLC initially appears in the peripheral airways, a method to perform biopsies on these lesions is desirable, especially if such a solution limits radiation exposure and avoids unnecessary surgical intervention. Currently available solutions in this space, such as the superDimension system (Medtronic Inc., Dublin, Ireland) or the SpIN system (Veran Medical, St. Louis, USA), leverage electromagnetic tracking for virtualised bronchoscopic navigation. Both of these solutions possess their own weaknesses: The SuperDimension, for example, relies on a tracked probe within a guide sheath. To take a biopsy, the probe has to be withdrawn from the sheath to accommodate the biopsy tool. This means that at the moment the biopsy is taken, the sheath is effectively "lost", and assumed to be in its last known location. The SpIN system avoids this by using tip-tracked instruments - a design choice that results in a higher per-operation cost for the hospital.

The objective of this work was to study a novel, steerable, electromagnetically-tracked bronchoscopy catheter and to develop a suitable actuation mechanism for it, with a view to facilitating tip-tracked navigation without the need for proprietary instruments or probe exchange. To achieve this objective, a number of smaller targets were set:

1. Create a kinematic model of catheter behaviour;
2. Verify this model using empirical data;
3. Use this information to create a manually-operated catheter handle;
4. Evaluate the efficacy of the catheter / handle assembly in a pre-clinical trial.

The project began by examining a similar, albeit less complex catheter system previously designed by the UCC Biodesign group, which also featured four tendons but only a 2.8 mm OD, one 5-DOF electromagnetic sensor and a 1.5 mm lumen. This catheter was used as a qualitative reference at the beginning of the project, as the delivery of the newly-designed version was delayed by several months.

A testing rig and desktop control software were built to acquire catheter data pertaining to the relationship between the magnitude and direction of catheter tip deflection, tendon displacement, and tendon force. A kinematic catheter model was established to attempt a prediction of this relationship. Several handle prototypes were designed based on this model and tested as soon as the catheters became available. Two investigations in live pigs were conducted with catheter / handle assemblies developed as part of this project, in conjunction with the CustusX [3] imaging platform and the Anser open-source electromagnetic tracking system [4] developed by the UCC Biodesign group. The remaining unused catheters were tested using the testing rig, and the data was compared to predictions made based on the kinematic model.

It was found that under ideal conditions, the prediction of the tendon displacement with respect to tip angle position was adequate - the error between prediction and empirical data was relatively large (average mean absolute error (MAE) of 2.28 mm (min: 1.03 mm, max: 3.01 mm)), but it scaled linearly with catheter tip angle (mean R-squared value of 0.98(min: 0.9607, max: 0.9925)). A lumped error compensation was therefore undertaken by subtracting the mean error regression line from the tendon displacement prediction. This reduced the average MAE to 0.3829 mm. The hysteresis between loading and unloading phases was quantified, with a mean energy loss due to friction in the system of 0.0237 Joules (min: 0.0166 J, max: 0.0293 J). Testing of the catheter under load from multiple tendons simultaneously showed that while the tip was practically steerable, the model developed earlier in the project broke down, with the source of error being related to movement of the catheter in the rigid section.

This work may serve as a jumping-off point to create a new specification for electro-magnetic navigation bronchoscopy catheters by incorporating the data and experience gathered over the course of this project. Ideally, a simpler but equally or more functional catheter could be designed and constructed using the recommendations set out in the conclusion on page 109.

Chapter 1

Literature review

This literature review presents similar systems of steerable sheaths and catheters found in the published body of work, and analyses their comparative strengths and weaknesses in order to gain insight into possible improvements or design lessons.

Steerable catheters have seen rapid development over the last decade, and the systems used to deflect the catheter are reaching ever greater complexity. Nevertheless, searching for the terms "steerable catheter" in the IEEEXplore database yielded only 68 results (as of 12th June 2018), and very few of these documents focused on the actual design of a catheter system. Searching on-line for existing catheter and sheath systems (such as those offered by Boston Scientific, St. Jude Medical and Covidien / Medtronic, among others) as well as performing patent searches proved more successful in finding various catheter actuation systems and control handles. During the review, it became clear that the majority of catheter systems use less than four pull wires, are not actuated electronically, and possess handles which are permanently attached to the catheter shaft. Furthermore, almost all steerable catheters found (with or without permanently attached control handles / actuation systems) are designed for single use only, such as the Merit medical SwiftNinja intravascular microcatheters [5], or the range of steerable electrophysiology catheters offered by Boston Scientific [6].

1.1 Catheter steering mechanisms

In April 2016, Ali et al [7] published a detailed paper reviewing over 500 different steerable catheter designs, and classified them into two main design philosophies: force generation at the tip of the catheter, or force transmission to the tip.

There are several methods of generating forces at the tip of a catheter. Some catheters, such as those modelled by Liu et al [8] use current-carrying coils within the magnetic field of an MRI scanner to generate forces which deflect the tip of the catheter. Others, such as those patented by Philippe Chastagner in 1991 [9] make use of the pronounced thermal expansion of some materials to elongate selected sections of the catheter in order to effect a bending of the shaft. Another type makes use of electroactive polymers which expand or contract when electrical current is applied to them [10], causing a deformation at the tip.

Conversely, force transmitting systems are by far the more common type of actuation mechanism for steerable catheters [7], and invariably use tension on tendons in various configurations to achieve the desired deflection. Pullwire catheters depend on the transmission of force from the proximal (user-side) to the distal (patient-side) ends of the catheter, implying that this force must be generated in the control handle of the catheter. The exact mechanism by which this force is generated varies from design to design, varying in complexity from electromechanical sources (in robotic systems), to manual exertion of force.

1.2 Manually-actuated electrophysiology catheters

Electrophysiology catheters are utilised for the intravascular mapping of electrical activity in the heart. They tend to be uni- or bidirectional catheters (deflecting in one or two opposing directions in the same plane), and can occasionally be asymmetrical, meaning their radius and angle of curvature is not the same in both directions of deflection. As a result their control unit only needs to apply tension on a maximum of two tendons at a time, limiting the complexity of the required mechanism. Three general design philosophies appear in this genre of catheter: (1) Lever-couple, (2) rotational and (3) plunger designs.

1.2.1 Lever-couple handles

The Blazer Dx-20 (Boston Scientific [11]) is a duodecapolar electrophysiology catheter with a coupled-lever deflection mechanism. It deflects bidirectionally, and with symmetrical curves.

The design itself relies on the user first turning the catheter handle to select the correct plane of deflection, and then rotating the lever couple to deflect the tip. Once in the desired position, the deflection can be locked by means of a rotating lock knob



Figure 1.1: Boston Scientific Blazer Dx-20

on the top of the handle, relieving the user of the fatigue caused by maintaining the deflection.

A similar design is found in a 1992 Patent by Heinzelman and Brooks [12]. Fig. 1.2 shows the inner workings of this type of handle.

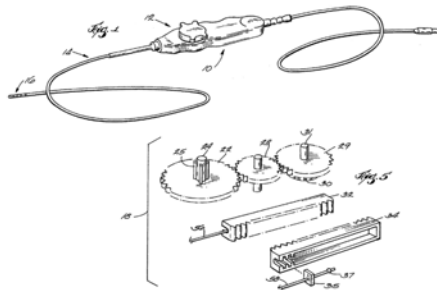


Figure 1.2: US Patent 5,364,351 Fig. 1 - Heinzelman and Brooks, 1992 [12]

This design has the added benefit of being able to generate a mechanical advantage through its use of gearing in the handle, further reducing the torque required by the operator. However, this system is limited to bidirectional catheters since the mechanism can only actuate one antagonistic pair of tendons at a time. Integrating a matched second mechanism to control the third and fourth tendon is difficult to achieve due to the handle's limited internal space and its ergonomic requirements.

1.2.2 Rotational-style handles

The Boston Scientific Radia [13] system is an electrophysiology catheter with bidirectional steering and asymmetrical curvature.

Unlike other bidirectional catheters, the Radia possesses only one tendon; the initial curvature is created by a pre-bent spring core. When the control knob (white portion in Fig. 1.3) is rotated clockwise or counterclockwise the tension is adjusted. Relaxing the tension allows the catheter to return to its preformed shape, and increasing it causes the catheter to bend the other direction. This design has the advantage of being a very mechanically simple assembly - there is only one tendon to actuate, and



Figure 1.3: Boston Scientific Radia electrophysiology catheter

the control mechanism only consists of a threaded portion of the handle. When the control knob is turned, the thread causes the actuation element to move forward or backward, thus applying or relieving the tension on the tendon.

1.2.3 Plunger-style handles

Plunger-style actuation systems are another variant of manual control handles. Their design is even simpler than the rotating-knob style and is usually limited to unidirectional catheter applications. The Polaris X catheter [14] (Fig. 1.4), also used for electrophysiology, is one such example.



Figure 1.4: Boston Scientific Polaris X electrophysiology catheter

The handle consists of a simple plunger, which is moved forward or backward to increase or decrease the tension on the tendons, which in turn changes the degree of deflection at the tip.

The Orbiter ST [15] (Fig. 1.5) is an amalgam of the simple unidirectional plunger-style handle of the Polaris X and the pre-curved shaft of the Radia system (Fig. 1.3).

The Orbiter's user interface is a variation of the plunger concept: instead of a full plunger, the handle features a sliding switch on one side of the handle. Moving the switch forward or backward will result in the catheter either deflecting forward or backward.



Figure 1.5: Boston Scientific Orbiter ST electrophysiology catheter

The remaining steerable catheters produced by Boston Scientific feature control handles which show only minor variants of the three design patterns outlined above. The EP XT features unidirectional steering and a twisting control knob handle. The Dynamic XT has the same catheter shaft as the EP XT, but instead of a rotating knob features a plunger-style handle, and the SteeroCath DX as well as the new electromagnetically-guided IntellaNav XP and IntellaNav MiFi XP [16; 17] cardiac mapping and ablation catheters all feature handles similar to the Blazer Dx (see Fig. 1.1).

1.3 Manual electromagnetic navigation bronchoscopy (ENB) systems

An important class of catheters for this work is those which include electromagnetic tracking sensors. These are already used widely in bronchoscopy. Electromagnetically guided bronchoscopy is a bronchoscopy procedure which makes use of electromagnetic fields to guide and position a tool within the airways. The procedure generally takes place in the following order: First, the patient undergoes a CT scan. The scan provides a series of "slices" of the patient's thorax in the three principal planes of the body. These slices are composited into a three-dimensional model of the organ. During the procedure (see Fig. 1.6), the patient is placed within an electromagnetic field projected by an emitter. This field induces a small voltage in a sensor attached to the catheter or surrounding guide sheath. The magnitude and phase of the induced voltage is used to determine the sensor's position within the magnetic field.

When the bronchoscope and catheter/sheath are introduced, the sensor is used to make a survey of the airway, allowing the attached computer to register the computed 3D model of the lung to coordinate space of the tracking system. This technique

allows procedures to be performed beyond-line-of-sight in the outer airway, where the size of the lumen no longer permits a conventional bronchoscope to fit. Other than during the initial CT scan, the tracking system also does not emit any harmful ionising radiation, unlike conventional fluoroscopy-based procedures.

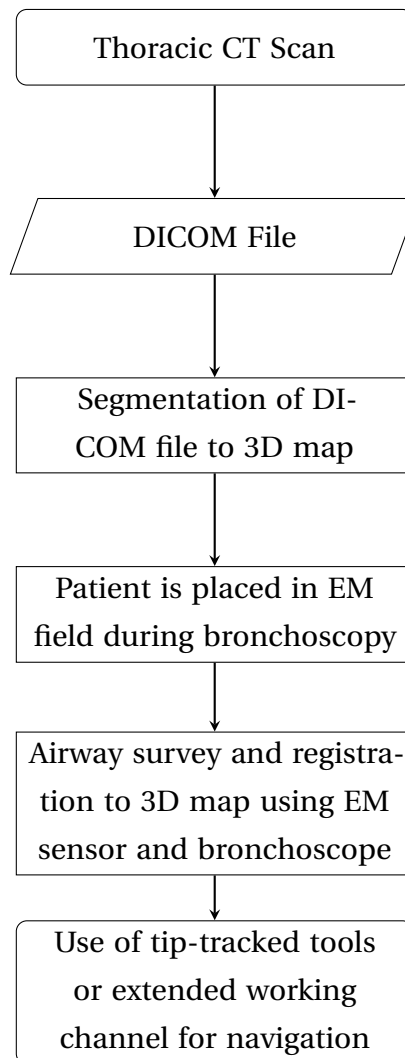


Figure 1.6: Flowchart of a typical ENB procedure

The advantage of ENB over other types of interventions (such as surgery, percutaneous procedures or standard bronchoscopy) lies in the combination of tip-tracked instruments and computer image guidance to reach lesions beyond the line-of-sight of the bronchoscope itself. To reach these, a bronchoscopist would normally move the endoscope as far forward as the length of the scope and the size of the airway permit. The tool, usually a biopsy forceps or aspiration needle, would be inserted through the working channel and forwarded until it has passed far enough into the airway that it is no longer be visible from the tip of the bronchoscope. Once visual

contact has been lost the bronchoscopist must rely on a fluoroscopic image, meaning increased patient and operator radiation dose, bulky protective equipment and the loss of depth perception associated with projecting a three-dimensional anatomy into a two-dimensional image.

ENB (see Fig. 1.7) yields more information on tool position. The sensor's location is marked on the CT images (see the lower three panels of Fig. 1.7), as well as in the 3D model of the airways (Fig. 1.7, top right). All of this information is relayed to the operator in real time, with the only exposure to ionising radiation being a preoperative CT scan.

Baaklini et al [18] reported the diagnostic yield for peripheral lesions at 53%, dropping to 14% for lesions of less than 2cm in diameter. By comparison, Gildea et al [19] were able to achieve diagnostic yields as high as 74% using the electromagnetically-guided SuperDimension Bronchus system.

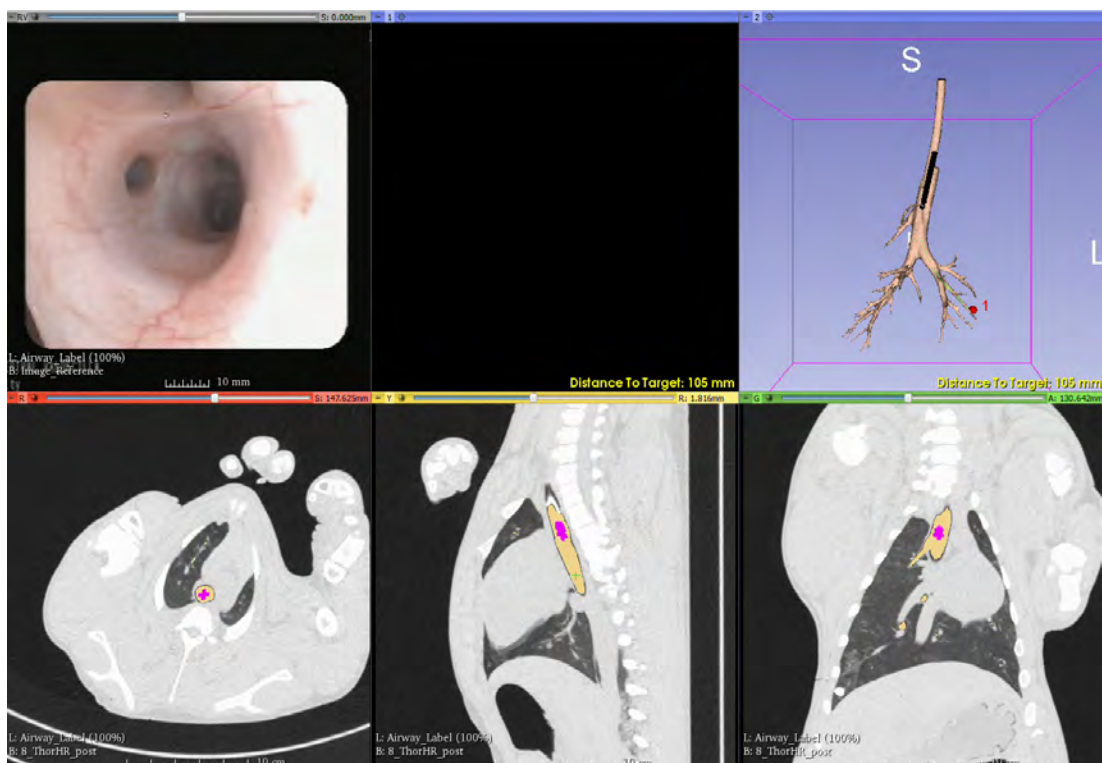


Figure 1.7: Screenshot from 3DSlicer [20] during an ENB procedure in a live animal model

1.3.1 SuperDimension iLogic catheter

The SuperDimension iLogic catheter (Covidien as of 2012, Medtronic as of 2015) is one of the few omnidirectionally-steerable catheters found which is currently being

sold. The catheter itself is designed without any working channel, and exists purely as an electromagnetic guide. In use, the catheter is inserted through the working channel of an endoscope, along with a sheath. The catheter allows the sheath to be navigated to the desired position within the lung. Once the position is reached, the catheter is withdrawn, leaving the sheath in place. A biopsy tool such as a forceps or cytology brush is then inserted to take the tissue sample for pathological analysis.

In contrast to the previously-reviewed catheters, the iLogic features four tendons. The wires are tensioned by a plunger-style handle. In order to select the plane of deflection, the plunger is rotated to select which tendon to tension. The handle allows the actuation of individual tendons separately, but also features selector positions which permit two tendons to be tensioned at once, allowing deflection in eight unique planes, each separated by a 45-degree angle.

It could be said that this selectable actuation makes the catheter a unidirectional catheter with a selectable plane of deflection, as another plane cannot be selected without first releasing the tension on all tendons and rotating the selector on the plunger to a new position.



Figure 1.8: Covidien / SuperDimension iLogic catheter handle

Disassembling the catheter exposed the actuation mechanism within (see Fig 1.9): each tendon terminates in a terminal block. This block, quarter-cylindrical in cross-section, features a lug on the exterior round surface. The lug engages a matching shelf on the selector ring when the ring has been rotated to select the tendon. When the plunger is actuated, it takes the selected block with it, thus applying tension to the selected tendon.



Figure 1.9: Covidien / SuperDimension iLogic handle, disassembled to show the actuation mechanism

1.3.2 The View™ catheter, Veran medical technologies

Veran Medical Technologies created a bidirectionally-steerable catheter for ENB. The system consists of a disposable, endoscope-style handle, with a lever actuator to control the deflection of the catheter's tip. This catheter is unique in that it possesses its own lumen. It therefore does not require a separate guide sheath. Instead, the catheter is also designed to work with disposable instruments which also have tracking sensors embedded in their tips, allowing the bronchoscopist to maintain position at all times, rather than relying on an untracked guide sheath which may lose position while the tracking probe is exchanged for an instrument.



Figure 1.10: The View™ catheter, Veran medical Technologies

1.4 Other manual catheter handle designs

Generally speaking, existing products such as those by St Jude Medical [21], Merit Medical [22] and Medtronic [23] follow a narrow range of design patterns. The control handles for catheter products by these companies all use some variant of either lever, plunger, twisting knob, or sliding switch designs.

Conversely, a large number of patents surrounding the design of handles for manual steerable catheter control exist, including designs for uni-, bi- and omnidirectional

catheters. Patents mentioned in this review were selected due to their potential applicability as engineering solutions to the design requirements of this project. For example, US patent 6,007,531 by Snoise, Mark and Rowley (Dec 1999) [24] describes a novel manual control handle for a bidirectional catheter. The proposed design differs from other manual handles in that it actually incorporates an adapter into the catheter shaft, with the intention of enabling sterilisation and re-use of the handle section. It differs further from conventional designs by using a pistol-grip layout combined with a rotating knob style actuator.

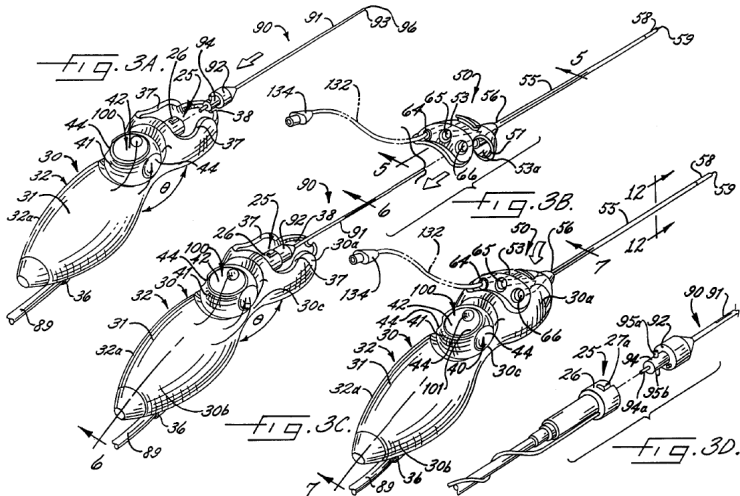


Figure 1.11: US Patent 6,007,531 (figure 3A-D, Dec. 1999)

Another interesting patent is US20100004591A1 (2008) [25], issued to Boston Scientific Scimed Inc. The design described within the patent document consists of an endoscope-like handle, axially aligned with the shaft of the catheter. The handle is designed for a bidirectional, tendon-actuated system, but also describes how the design could be modified to accommodate omnidirectional deflection.

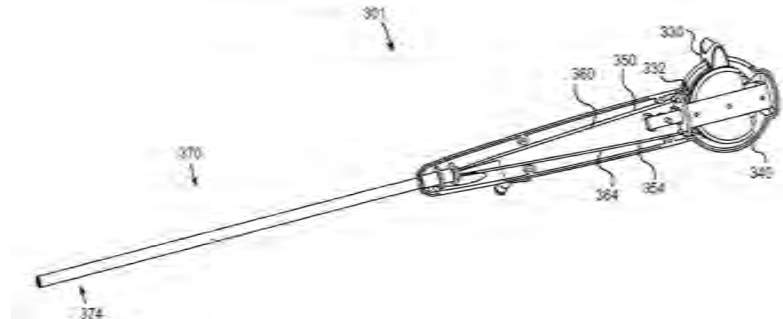


FIG.8

Figure 1.12: US Patent US20100004591A1 (figure 8), 2008 [25]

Boston Scientific Scimed also filed a patent application [26] in 2013, describing a joystick-based steering mechanism for an omnidirectional catheter (US patent US20130253469A1). The joystick is attached to a rotating sphere which allows a swashplate to pivot with the joystick's movement. The catheter's tendons are spaced at 90 degrees around the swashplate. It should be noted that the handle, in its current layout, will always apply tension to the wire opposite to the direction in which the joystick is pushed. For example, if the joystick is pushed upwards the catheter will deflect downwards, and vice versa. This may make for a non-intuitive user interface.

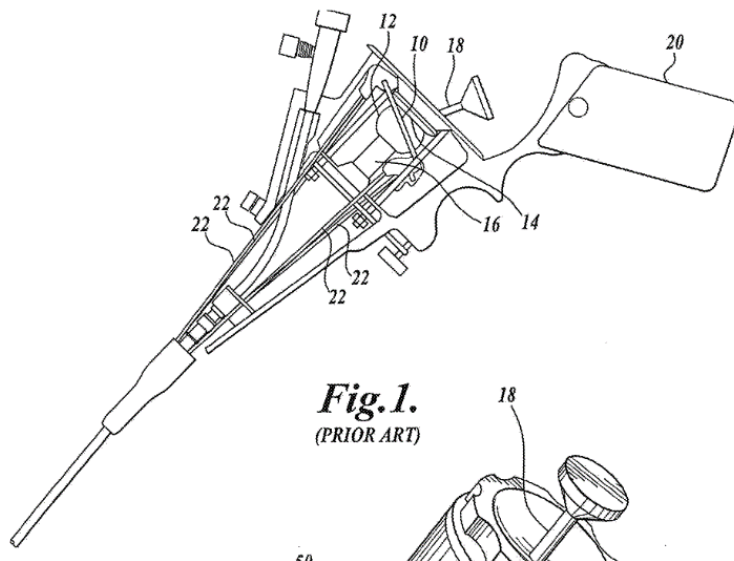


Figure 1.13: US patent US20130253469A1 (figure 1), 2013 [26]

1.5 Robotic catheter and surgical systems

Robotic catheter systems are rapidly following in the wake of advances in robotic surgery (e.g. the first robotic telesurgery [27]) in the early 2000's. Currently, intravascular robotic systems are used mainly for diagnostic procedures, for example the Sensei X (Hansen Medical), which is purpose-built for ICE (intracardiac echocardiography) and EP(electrophysiology)/mapping. However, these systems are also beginning to see use as therapeutic devices, for example for endovascular aneurysm repair (EVAR) [28].

Khoshnam et al, 2014 [29] investigated the robotic control of intravascular catheters to improve catheter-tissue contact during cardiac tissue ablation. The catheter handle and shaft that was chosen for automation was an unnamed unidirectional plunger-type catheter. For the experiment, the catheter handle was clamped into a linear motion apparatus which could advance the catheter as well as move the plunger to modify the deflection at the tip of the catheter. A subsequent paper published by the same team (Khoshnam et al, 2015 [30]), used a similar actuation setup, again using a unidirectional, plunger type catheter, this one identified as a product of Biosense Webster, model D7TFL252RT.

Ataollahi et al, 2015 [31] took a different approach, developing both their own catheter and actuation system. The prototype described in the paper made use of four tendons to omnidirectionally deflect the catheter's tip. The test rig (Fig. 1.14) features a set of four stepper motors, mounted to a motion rig that allows linear motion (advancing the catheter) as well as rotation of the catheter about its long axis. One of the more interesting facets of this approach is the novel catheter adapter used to removably attach the catheter to the actuation base.

The adapter itself (Fig. 1.16) consists of a set of four splined shafts which mate with a matching set of splined sockets in the bottom of the adapter. When the adapter is fitted on to the base (Fig. 1.15), the stepper motors can directly actuate the spools in the adapter. Each tendon is wound about one spool inside the adapter. The stepper motors can then tension each tendon individually, permitting full control over each of the wires.

A commercial example of a robotic catheter system can be found in the Sensei and Magellan systems, developed by Hansen Medical. These robots are both designed for intravascular interventions, however the Sensei is limited to performing intracardial electrophysiology, while the Magellan is designed for general-purpose intravascular

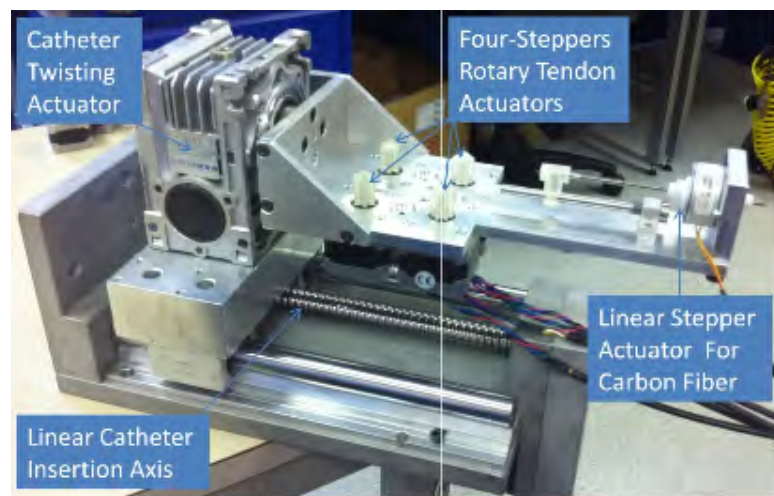


Figure 1.14: Motion rig developed by Ataollahi et al

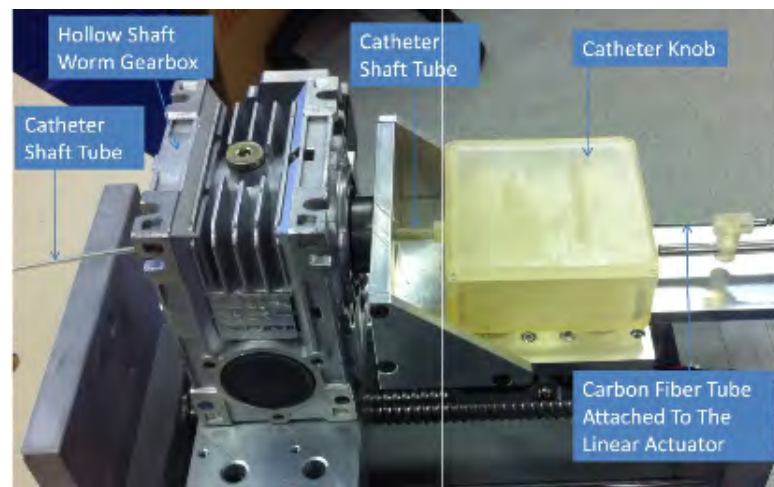


Figure 1.15: Motion rig developed by Ataollahi et al, with catheter and adapter in place

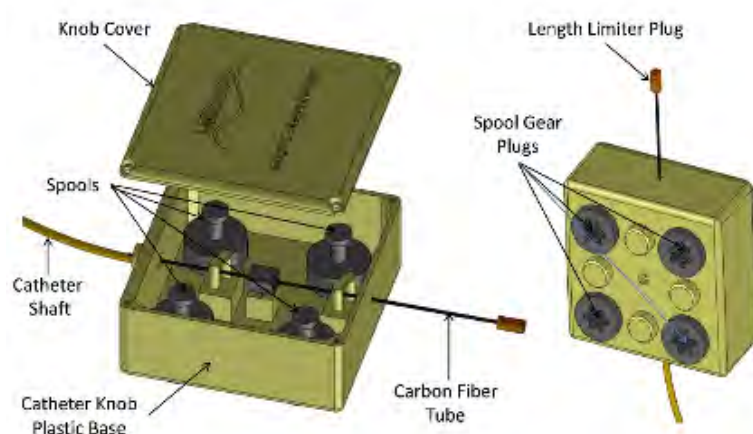


Figure 1.16: CAD model of the catheter connector built by Ataollahi et al

surgery. These robots comprise two catheter adapters; the first is attached to an omnidirectionally-steerable sheath, while the second operates an electrophysiology catheter (also omnidirectional) inside the sheath.



Figure 1.17: Artisan Extend catheter, attached to a Sensei X, Hansen Medical

In either case, the adapter used by the system to connect or disconnect the disposable section of the robotic catheter is quite simple, and follows the layout described in the paper by Ataollahi et al [31], namely a housing containing a set of four spools attached to the proximal end of the catheter. The housing clips onto a mating surface on the robot, which features a matching set of four motors to actuate the spools and thereby deflect the catheter.

The Da Vinci robotic surgery system developed by Intuitive Surgical Inc, has a similar adapter system to allow articulation at the tip of its rigid tools. The Da Vinci system is a fully robotic laparoscopic surgery system which allows a surgeon to operate remotely on the patient. A 2001 patent by Cooper, Julian and Blumenkranz [32] and granted to Intuitive Surgical, Inc describes an adapter for a medical device with just such a four-spool arrangement of tendons. (See Fig. 1.18 and Fig. 1.19)

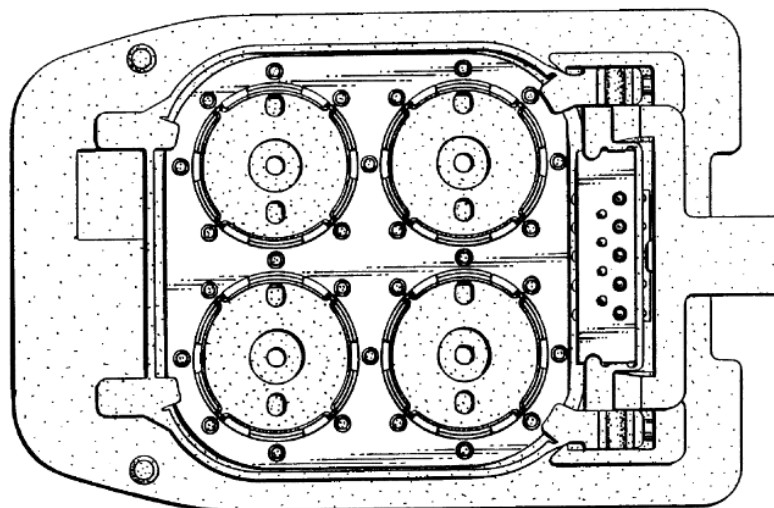


Figure 1.18: US patent D441,076 S - April 2001



Figure 1.19: Older version Da Vinci connector system, as implemented on the Da Vinci Si.

This connector design was a slide-in variant, designed to facilitate the easy change of tools during surgery. When the tool is detached from the base unit, the clips at the top of the adapter shell (Fig. 1.19) are pressed in, disengaging the locking tabs and allowing it to slide out unhindered.

The more recent Da Vinci Xi model is equipped with a relative of this connector, featuring a five-spool system rotated 90 degrees, so that the axes of the spools lie parallel to the axis of the instrument shaft (Fig. 1.20). As a result, when the instrument is slid into place, spools and actuators are already aligned and need only be clipped on.



Figure 1.20: Da Vinci Xi 5-spool connector

Other robotic catheter intervention systems exist which have foregone the creation of their own catheters and adapter systems, opting instead to go the somewhat more convenient route of using existing manufacturers' catheter handles as their catheter / drive element interface.

Catheter Robotics, Inc. has developed a robotic catheter system called Amigo [33]. The Amigo is a dedicated robotic Electrophysiology platform, designed to work with Boston Scientific's Blazer series or with Biosense-Webster's EZ steer line of catheters. Both catheters possess a lever-couple style of handle. The robot interfaces with the catheter simply by using fixtures which allow the robot's drive elements to mate with the actuation lever on the handle, see Fig. 1.21. As a user interface, the system uses a remote control which mimics the control layout of the catheter handle, possessing a wheel to select tip deflection, a rotating dial to select catheter rotation, and two buttons to advance or retract the catheter.



Figure 1.21: Catheter Robotics' Amigo drive element with attached Boston Scientific Blazer-series catheter

Similarly, Stereotaxis, Inc. chose to use third-party catheters and matching adapters with the Niobe and V drive system[34]. The Niobe system is a magnetic navigation

system used for electrophysiology which uses a strong magnetic field to deflect the magnetic tip of the catheter inside the patient. The catheter is tracked using a fluoroscope, and advanced or retracted by the V Drive system.



Figure 1.22: Stereotaxis Niobe and V Drive assembled in a catheter laboratory

Fig. 1.22 shows the complete Stereotaxis system in place with the Niobe (left), and V Drive (right). Stereotaxis sells various adapter kits that allow the user to select different catheters for use with the system, including adapters for Biosense Webster SoundStar or Siemens AcuNav Intracardiac Echocardiography Catheters, Biosense Webster LASSO 2515 circular mapping catheters and LASSO 2515 NAV catheters.

1.6 Conclusion

While many steerable catheters exist on the market, the majority are designed for use in cardiovascular applications, where tortuous vessel anatomy necessitates steerability. Specifically, these catheters are designed for use in electrophysiology, intracardiac ablation (the practice of selectively ablating tissue to rectify arrhythmia) or ICE (Intracardiac Echocardiography). This field also showed well-developed and marketed robotic navigation systems, such as the SenseiX / Artisan Catheter (Fig. 1.17) and the Magellan System from Hansen Medical, the Amigo system by Catheter Robotics, Inc (Fig. 1.21), or the Niobe / Vdrive magnetic navigation system by Stereotaxis, Inc.

In the field of electromagnetic navigation bronchoscopy (ENB), two main competitors exist: iLogic / SuperDimension (now Covidien/Medtronic) (Fig. 1.8) and Veran Medical Technologies (Fig. 1.10). While ENB technology and electromagnetic tracking systems as a whole are promising, the existing systems have certain weaknesses. The iLogic system is used to position a guide sheath, and once the sheath is in position, the catheter is withdrawn to allow a tool to be inserted through the lumen of the guide, losing tracking during the part of the procedure where there is the greatest risk

of inadvertent displacement. On the other hand, The View catheter by Veran Medical Technologies tracks both the sheath and the instrument, increasing the cost of the operation as both the tracked sheath and the tracked instrument are single use and far more expensive than their conventional, untracked, alternatives. Additionally, The View catheter is only bidirectionally deflectable.

The market demand for simplicity and lower cost seems to have led catheter manufacturers to be more conservative, causing the industry to settle into a narrow range of user interfaces and mechanical actuation designs. Even where omnidirectional steering is a requirement, such as with the iLogic catheter, the handle design does not stray far from other plunger-based designs (such as the Boston Scientific Polaris X (Fig. 1.4)). A similar process seems to have taken place in robotic catheter systems, with manufacturers either creating very simple shaft-to-shaft couplings, or foregoing custom catheter designs altogether and creating adapters to interface the robot with a catheter designed for manual use. Recent research in robotic catheter systems has not bucked this trend; projects such as those by Ataollahi et al [31] or Khoshnam et al [29] have either designed their automation system around the manufacturer's manual handle, or emulated the connectors seen in systems such as the Da Vinci robot (Fig. 1.20))or the Sensei X.

The design created as part of this project could be seen as an attempt to combine the best aspects of the SuperDimension and Veran medical products. It has a tracked sheath like The View catheter, but omnidirectional steering like SuperDimension, with a not-dissimilar user interface.

Table 1.1: Summary of reviewed catheter systems

System	Manufacturer / Designer	Application	No. of tendons	Directionality	Automated/Manual	Working Channel	Tracking	Patent Reference	Commercially Available
Blazer Dx	Boston Scientific	Electrophysiology / Ablation	2	Bidirectional	Manual, also used in Amigo system	No	Fluoroscopy	US5254088 A (expired)	Yes
(Unnamed)	Ep Technologies	Catheter handle design	2	Bidirectional	Manual	N/A	N/A	US5364351 A (expired)	N/A
Radia	Boston Scientific	Electrophysiology	1	Bidirectional	Manual	No	Fluoroscopy		Yes
Polaris X	Boston Scientific	Electrophysiology	1	Unidirectional	Manual	No	Fluoroscopy		Yes
Orbiter ST	Boston Scientific	Electrophysiology	1	Bidirectional	Manual	No	Fluoroscopy		Yes
EP XT	Boston Scientific	Electrophysiology	1	Unidirectional	Manual	No	Fluoroscopy		Yes
Dynamic XT	Boston Scientific	Electrophysiology	1	Unidirectional	Manual	No	Fluoroscopy		Yes
Stereocath Dx	Boston Scientific	Electrophysiology	2	Bidirectional	Manual	No	Fluoroscopy		Yes
IntellaNav XP	Boston Scientific	Electrophysiology / Ablation	2	Bidirectional	Manual	No	Fluoroscopy / Electromagnetic Tracking	/	Yes
IntellaNav MiFi XP	Boston Scientific	Electrophysiology / Ablation	2	Bidirectional	Manual	No	Fluoroscopy / Electromagnetic Tracking	/	Yes
SwiftNinja	Merit Medical	Vascular Microcatheterisation	2	Bidirectional	Manual	No	Fluoroscopy / Electromagnetic Tracking	/	Yes
iiLogic	SuperDimension (Covidien/Medtronic)	Electromagnetic Navigation Bronchoscopy	4	Omnidirectional (unidirectional with selectable direction)	Manual	Yes	Fluoroscopy		Yes
The View	Veran Medical Technologies	Electromagnetic Navigation Bronchoscopy	2	Bidirectional	Manual	Yes	EM tracked		No
(Unnamed)	Catheter Imaging Systems, Inc.	Catheter handle design	2	Bidirectional	Manual	Yes	EM tracked		Yes
(Unnamed)	Boston Scientific Scimed	Catheter handle design	2-4	Bidirectional or Omnidirectional	Manual	Yes	N/A	US6007531 A (expired)	No
(Unnamed)	Boston Scientific Scimed	Catheter handle design	4	Omnidirectional	Manual	Yes	N/A	US2010004591 A1	No
(Unnamed)	Atollah et al	Research project	4	Omnidirectional	Automated	Yes	N/A	US20130253469 A1	No
Artisan Extend	Hansen Medical	Electrophysiology	4	Omnidirectional	Robotic system using either Blazer Dx or Biosense Webster EZ steer	Yes	Fluoroscopy		Yes
Amigo	Catheter Robotics	Electrophysiology	2	Bidirectional	No	Fluoroscopy			Yes
Niobe/V Drive	Stereotaxis, Inc	Electrophysiology; Intracardiac echocardiogram	N/A (magnetic actuation)	Omnidirectional	Automated	N/A (depends on catheter being used with the system)	Fluoroscopy		Yes

Chapter 2

Catheter design and modelling

2.1 Catheter specification

This project was based around the development of a system for electromagnetic navigation bronchoscopy (ENB), with a view to creating a steerable catheter assembly amenable to autonomous or semi-autonomous navigation. The system's purpose was primarily to facilitate precise placement of biopsy tools such as forceps or cytology brushes, up to a tool diameter of 1.2 mm.

A prior catheter design by the UCC Biomedical Design Lab and manufactured by Vention Medical was sized to emulate the function of a bronchoscopy guide sheath, such as the Olympus K-201 kit, with an outer diameter of 2.6 mm, 1.5 mm working channel, and length of 1050 mm [35]. It was steered using four tendons, but possessed only one sensor lumen. The 2.6 mm outer diameter allowed this catheter to fit through the 2.8 mm working channel of a regular bronchoscope. The catheter developed as part of this project had to be large enough to accommodate an additional sensor, increasing its outer diameter to 3 mm, while keeping the same 1.5 mm inner lumen and 1050 mm length. Unfortunately, this limits the catheter to use in specialised therapeutic bronchoscopes with 3.2 mm working channels, such as the Olympus BF-XT160 [36], the Pentax EB-1970TK [37], or the Fujifilm EB-530XT [38]. The final catheter was specified for manufacture at the Biomedical Design lab in UCC and was manufactured and assembled by Teleflex OEM, Co. Limerick.

The catheter designed for this project was a multi-lumen extrusion possessing three main feature groups:

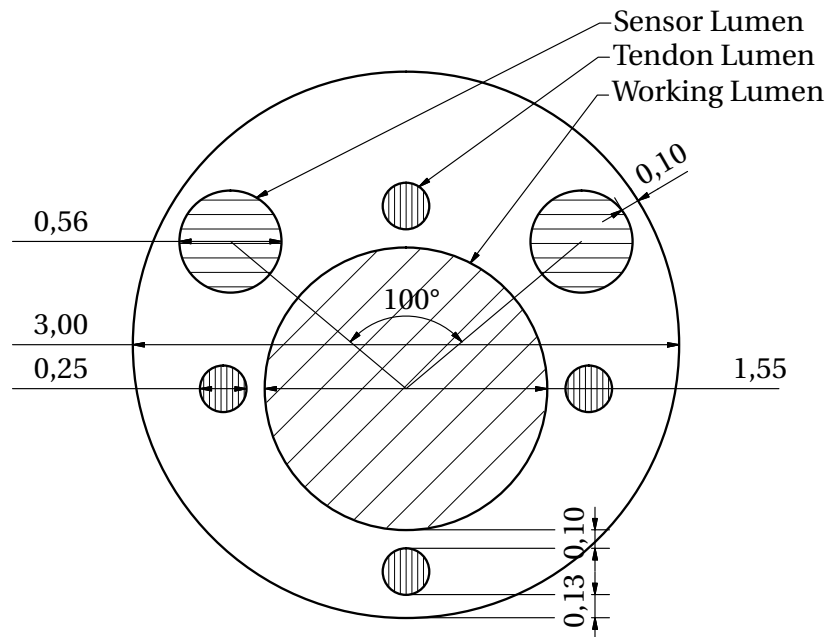


Figure 2.1: Cross-sectional view of the catheter shaft. All dimensions in mm.

- The working lumen (Fig. 2.1, diagonal hatching)
- The tendons, positioned around the lumen (Fig. 2.1, vertical hatching)
- The sensor lumens, for the two 5-DOF position sensors (Fig. 2.1, horizontal hatching)

2.1.1 Steering

A catheter inside a flexible endoscope cannot easily be rotated within the working channel to change its roll angle, as the friction between the catheter and the endoscope lumen causes unpredictable slip-stick movement of the catheter tip. Without this control, the design philosophy of the uni-or-bidirectional catheters (the majority of which were designed to be operated without endoscopes) reviewed in chapter 1 could not be applied here. Instead, it was decided that fully omnidirectional steering had to be implemented using four tendons, based on preliminary clinical user feedback.

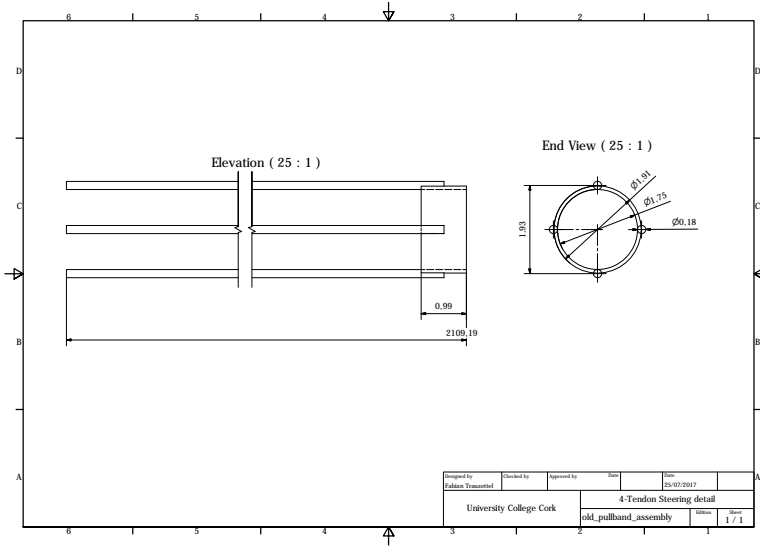


Figure 2.2: Detailed view of the catheter tendons. All dimensions in mm. Figure not to scale.

Fig. 2.2 shows a detailed view of the stainless steel tendon / pullband assembly used to anchor the tendons at the distal tip. The pullband itself serves to anchor the tendons into the rigid tip, distal to the articulated section. The four tendons are 0.1778 mm in diameter and are welded to the pullband, providing a solid mechanical joint. The tendon positions are highlighted in red in Fig. 2.1.

2.1.2 Position sensing

Tracking of the catheter in 3D space is achieved by means of the Anser electromagnetic tracking (EMT) system developed by UCC's Biomedical Design Lab [4], [39]. This tracking system makes use of EM sensor coils manufactured by Northern Digital, Inc. Due to the nature of the system, a single-coil sensor may only capture its own position in five degrees of freedom - X, Y, Z, pitch and yaw. The roll angle can only be determined through the use of a second sensing coil. Accordingly, Northern Digital manufactures 5DOF and 6DOF sensors, consisting of one and two coils, respectively (see table 2.1).

Table 2.1: List of NDI EM tracking sensors available for purchase [40]

Degrees of Freedom	Part number	Dimensions (diameter x length)
5	610099	0.5 mm x 8 mm
5	610090	0.8 mm x 11 mm
5	610057	0.9 mm x 12 mm
5	610058	0.9 mm x 6 mm
6	610059	0.8 mm x 9 mm
6	610029	1.8 mm x 9 mm

As the catheter's inner and outer diameters were limited to 1.5 and 3 mm, and to constrain costs, it was decided to use two 610099 5DOF sensors in this catheter. Their positions are highlighted in yellow in Fig. 2.1, and visible in Fig. 2.3

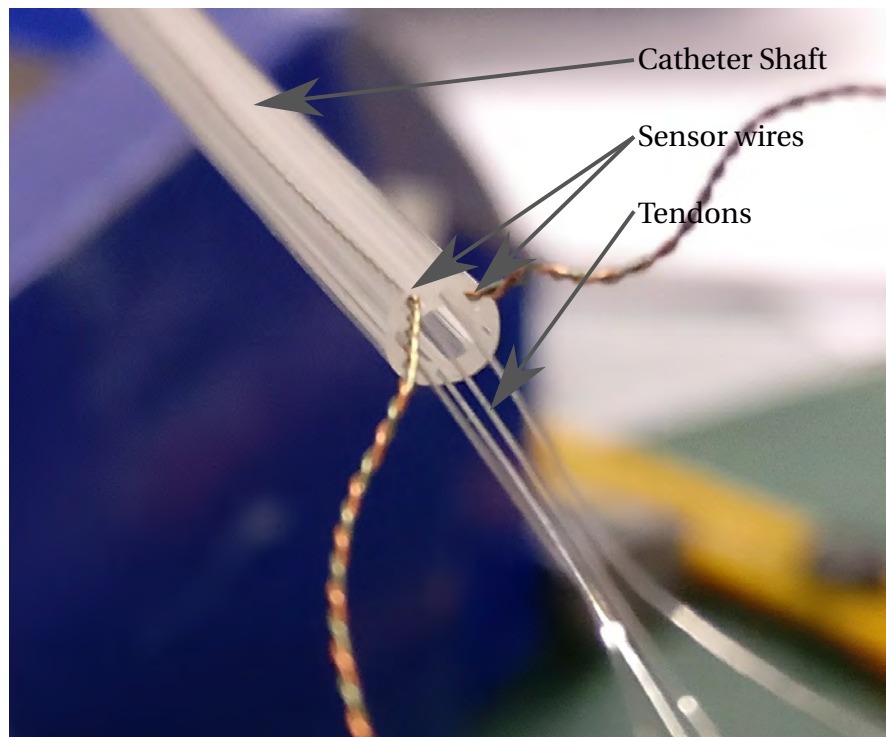


Figure 2.3: Close-up photo of the proximal end of the catheter, showing the working channel (center), the two twisted-pair EM sensor wires as well as the four stainless steel tendons.

2.2 Catheter steering model

2.2.1 Single-tendon deflection

As one of the end goals of this project is to create a steering assembly for ENB catheter navigation, it is of some importance to develop a model of the relationship between the catheter deflection and their displacement. To this end, a rudimentary model was created by inspection of the geometry of the catheter's articulated section.

Consider the articulating section of the catheter as a beam of uniform cross-section. When the tip is deflected, the new shape of the section describes a sector of a circle. Fig. 2.4 shows the basic geometry of the articulating section. Note from Fig. 2.4 that the innermost curve has a reduced arc length when compared to the neutral axis L , while the outer curve increases in length. The neutral axis L , does not change in length, regardless of the state of deflection. These geometric properties can be used to determine a basic relationship between tendon displacement and the magnitude of tip deflection.

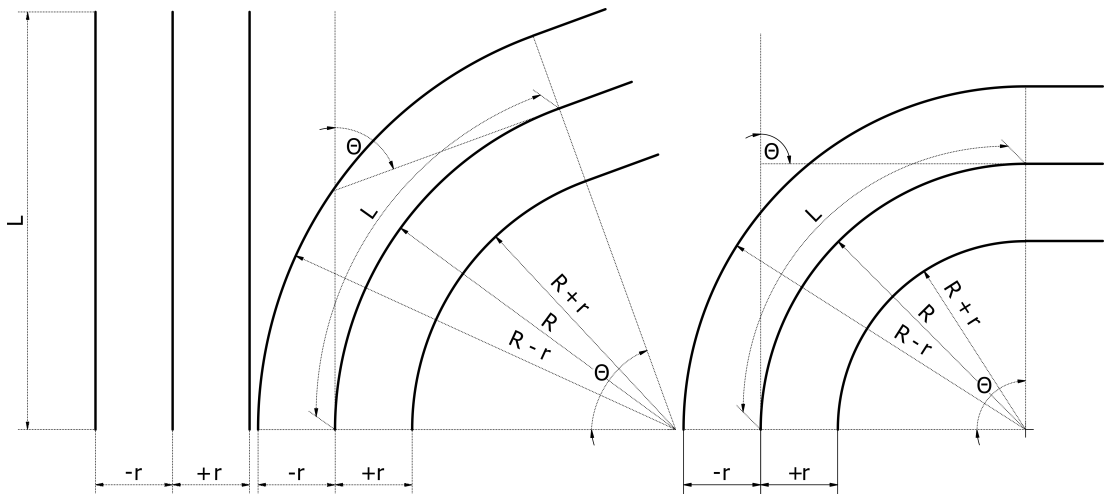


Figure 2.4: Longitudinal section of the catheter in relaxed (left), partially deflected (center) and fully deflected state (right)

The geometric terminology used in Fig. 2.4 and Eqns. 2.1 - 2.4 is as follows:

θ is the magnitude of deflection in degrees, measured as the deviation from the undeflected (straight) position ($0^\circ \leq \theta \leq 90^\circ$),

L is the length of the neutral axis of the section and is equal to the undeflected length of the articulating section,

R is the radius of curvature of the neutral axis,

r is the offset between the neutral axis of the articulating section and any parallel axis in the same section, e.g. a steering tendon running through a parallel lumen.

Arc Length is expressed as:

$$L = \pi R \left(\frac{\theta}{180} \right) \quad (2.1)$$

Bearing in mind that the distance from any tendon to the neutral axis is known (see Fig. 2.9), the offset r can be combined with Eqn. 2.1 to derive an expression linking the magnitude of catheter deflection, θ and the change in tendon position, D_T :

$$D_T = \pi(R - r) \frac{\theta}{180} - L \quad (2.2)$$

where:

D_T is the displacement of any tendon with offset r from the neutral axis, in the plane of deflection.

Note that r is subtracted from R as a result of the sign convention distinguishing the direction of the tendon's movement; if r is offset to the right in Fig. 2.4 it is positive, and to the left it is negative.

Rearranging Eqn. 2.1 to isolate the arc radius of curvature R gives

$$R = \frac{180L}{\pi\theta} \quad (2.3)$$

Substituting Eqn. 2.3 into Eqn. 2.2 allows us to simplify Eqn. 2.2 to:

$$D_T = -\frac{\pi r \theta}{180} \quad (2.4)$$

Perhaps counterintuitively, Eqn. 2.4 shows that the length of the articulating section has no bearing on the displacement of the tendon at any given value of θ . This is because we are mostly interested in the change in length of the tendon channel, not its absolute length. In this representation, the only variables relevant to tendon displacement are r , the radial distance between the neutral axis and tendon, and θ , the magnitude of deflection.

2.2.2 Multiple-tendon deflection

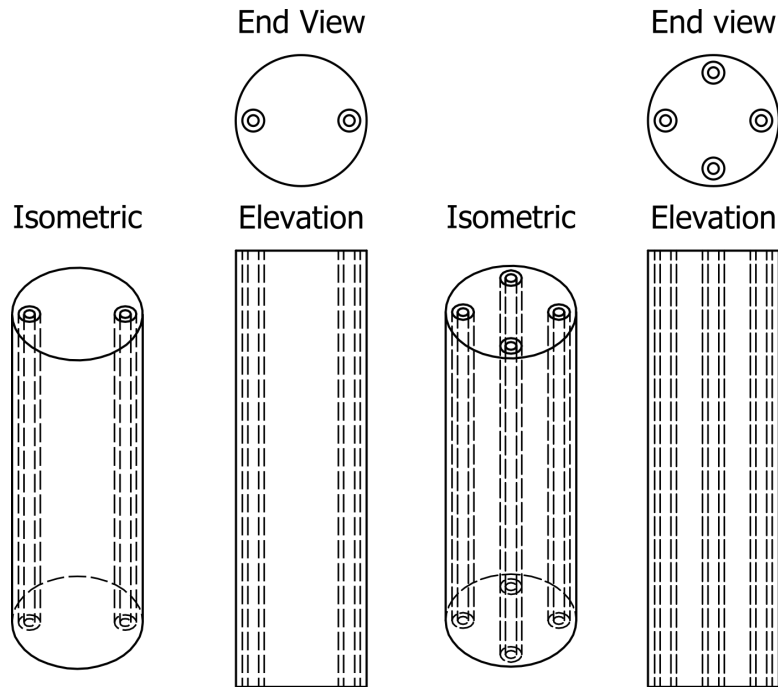


Figure 2.5: Simple two (left) and four-tendon (right) catheters. Fig. 2.4 shows the elevation of a two-tendon catheter, while Fig. 2.6 shows the end view of a four-tendon catheter.

The approach described in section 2.2.1 describes only the basic tendon displacements if the tendons are in the plane of deflection and therefore fails to describe any catheter with more than two tendons. In order to expand this model to any catheter with more than two tendons, we must first consider the transverse section of the catheter and the position of the tendons within it.

Fig. 2.5 serves as a visualisation aid to the reader. The catheter depicted on the left need not consider a *direction* of deflection, because the two tendons are in line with each other and the centroid of the section. Therefore the plane of deflection will always be collinear with the line orthogonally joining the two tendons. Conversely, the 4-tendon catheter depicted on the right is free to deflect in any given direction, as it will always have tendons that are not aligned with the current plane of deflection.

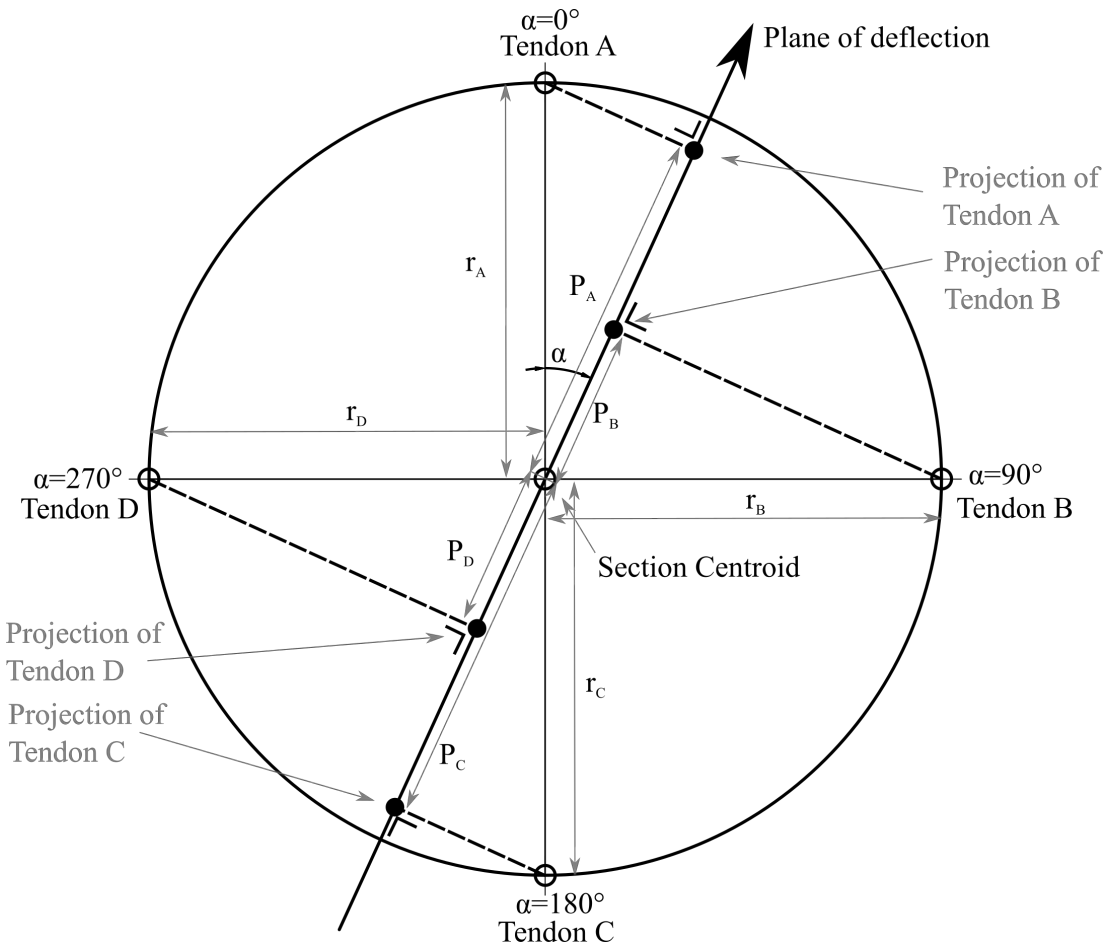


Figure 2.6: Transverse section of a basic four-tendon catheter. The large arrow shows the plane of deflection. Each tendon is perpendicularly projected on to the plane of deflection along the dotted lines.

In Fig. 2.6:

α represents the angle of the plane of deflection, as measured clockwise from the 12 o'clock position in Fig. 2.6;

r_A, r_B, r_C, r_D represent the distance between each tendon and the centroid;

P_A, P_B, P_C, P_D are the distances between the centroid and the point at which the projection of each tendon meets the plane of deflection

The catheter shown in Fig. 2.6 represents a specific design simplification as the tendon positions are equidistant from the centroid, with a symmetrical cross-section and equal 90° radial displacement between the tendons.

In order to obtain the tendon displacement for a given catheter tip deflection (θ) in a plane of deflection defined by α , we must first calculate the distances P_A, P_B, P_C and P_D which lie between the centroid and each of the points at which the tendons are

projected on to the plane of deflection. The large diagonal arrow in Fig. 2.6 shows an example plane of deflection. The dotted lines show the lines of projection from each tendon to the plane of deflection. These lines of projection are always perpendicular to the plane, regardless of the value of α .

If we examine the geometry of the cross-section in Fig. 2.6, we will find the following expressions to be true:

$$P_A = r_A \cos(\alpha) \quad (2.5)$$

$$P_B = r_B \cos(90 - \alpha) \quad (2.6)$$

$$P_C = r_C \cos(180 + \alpha) \quad (2.7)$$

$$P_D = r_D \cos(270 - \alpha) \quad (2.8)$$

Using the trigonometric identity

$$\cos(A \pm B) = \cos(A) \cdot \cos(B) \mp \sin(A) \cdot \sin(B)$$

these can be further simplified to:

$$P_A = r_A \cos(\alpha) \quad (2.9)$$

$$P_B = r_B \sin(\alpha) \quad (2.10)$$

$$P_C = -r_C \cos(\alpha) \quad (2.11)$$

$$P_D = -r_D \sin(\alpha) \quad (2.12)$$

We previously determined that the displacement of the tendon is given by Eqn. 2.4. Since r in Eqn. 2.4 represents the distance between the tendon and the centroid, and P_A through P_D represent the distance between the *projected* tendon and the centroid

as shown in Fig. 2.6, we can substitute for r in 2.4 with expressions 2.9 - 2.12, yielding expressions for tendon displacement at any angle of deflection along any plane of deflection.

$$D_A = -\frac{\pi\theta r_A \cos(\alpha)}{180} \quad (2.13)$$

$$D_B = -\frac{\pi\theta r_B \cos(90 - \alpha)}{180} = -\frac{\pi\theta r_B \sin(\alpha)}{180} \quad (2.14)$$

$$D_C = -\frac{\pi\theta r_C \cos(180 + \alpha)}{180} = \frac{\pi\theta r_C \cos(\alpha)}{180} \quad (2.15)$$

$$D_D = -\frac{\pi\theta r_D \cos(270 - \alpha)}{180} = \frac{\pi\theta r_D \sin(\alpha)}{180} \quad (2.16)$$

Tendon displacement for any plane of deflection ($0^\circ \leq \alpha \leq 360^\circ$) at $\theta = 90^\circ$

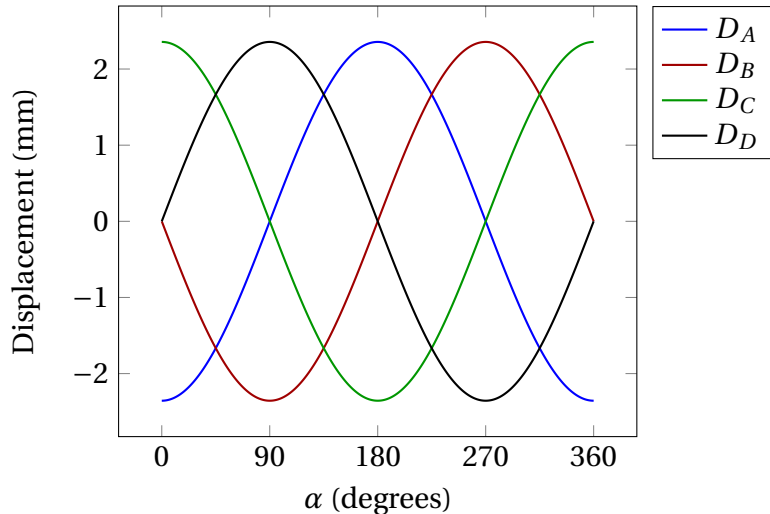


Figure 2.7: A plot of the tendon deflection at $\theta = 90^\circ$ and $r_A = r_B = r_C = r_D = 1.5\text{mm}$

In this simplistic model, tendon movement is entirely antagonistic, that is to say for any given direction and magnitude of tip deflection, opposite tendons along α will move the same distance in opposite directions; e.g. if $\alpha = 0^\circ$ and $\theta = 90^\circ$, tendons B and D will not move, but tendon A will be maximally shortened and tendon C will be maximally extended.

2.2.3 Experimental catheter

The idealised example in section 2.2.2 serves to illustrate the approach used in creating the deflection model for the actual catheter as built by Teleflex OEM (Teleflex Medical Ireland Ltd., Annacotty Business Park, Limerick). In this case, the measurements in Fig. 2.8 were used to adjust the formulae derived for the simple example in section 2.2.2.

2.2.3.1 Centroid calculation

As the cross-section of this catheter (see Fig. 2.8) is not symmetrical about the horizontal axis, the position of the section centroid must be found before we can proceed. In this case it is easiest to compute using the process of geometric decomposition. In geometric decomposition, the figure to be analysed is divided into a number of smaller, more easily-calculated segments. The centroid of each segment is located, as well as its area. Voids in the figure can be taken into account by counting the void as a negative area. Once each centroid is found relative to some reference point, the centroid of the main figure is the weighted average of the x and y coordinates, according to Eqns. 2.17 and 2.18.

$$C_x = \frac{\sum C_{i_x} \cdot A_i}{\sum A_i} \quad (2.17)$$

$$C_y = \frac{\sum C_{i_y} \cdot A_i}{\sum A_i} \quad (2.18)$$

where:

C_x = Figure centroid x coordinate

C_y = Figure centroid y coordinate

C_{i_x} = Segment centroid x coordinate

C_{i_y} = Segment centroid y coordinate

A_i = Area of segment

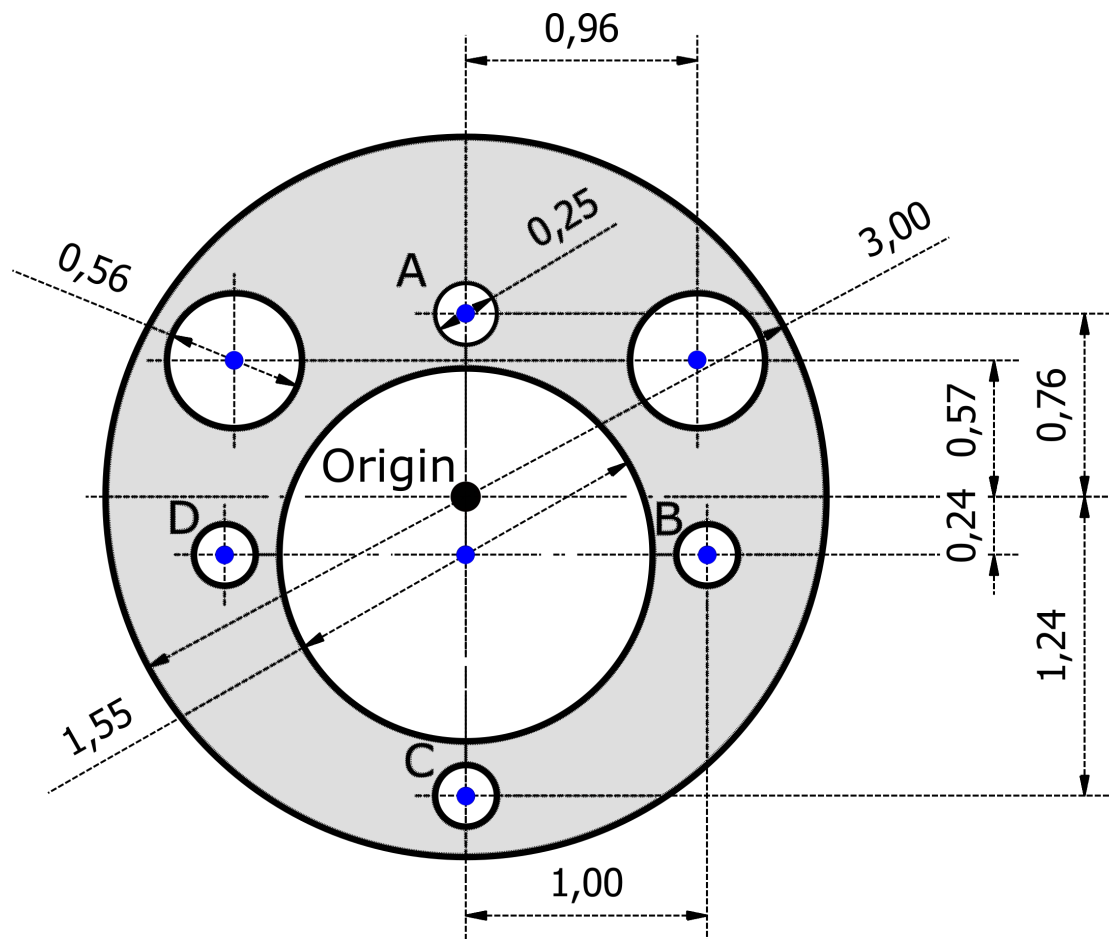


Figure 2.8: Cross-section of catheter, annotated with all dimensions used to locate the section centroid, as well as the centroids of each segment the section was decomposed into (blue dots). Solid areas are shaded grey.

The diagram in Fig. 2.8 was decomposed into the following components:

- The \varnothing 3 mm circle of the catheter shaft
- The \varnothing 1.55 mm circle of the working channel
- The \varnothing 0.25 mm circle of tendon A's lumen
- The \varnothing 0.25 mm circle of tendon B's lumen
- The \varnothing 0.25 mm circle of tendon C's lumen
- The \varnothing 0.25 mm circle of tendon D's lumen
- The \varnothing 0.56 mm circle of sensor A's lumen (left sensor)
- The \varnothing 0.56 mm circle of sensor B's lumen (right sensor)

Next, we calculate the area of each segment, as well as the location of its centroid relative to the reference point (labelled "origin" in Fig. 2.8). Fortunately, our section consists entirely of circular elements, making the location of each centroid very straightforward. The results of this step are shown in Tbl. 2.2.

Table 2.2: Segment areas (A_i), segment centroid positions (C_{i_x} , C_{i_y}), and weighted segment centroid positions

Segment	$A_i(\text{mm}^2)$	C_{i_x} (mm)	C_{i_y} (mm)	$A_i \cdot C_{i_x}$	$A_i \cdot C_{i_y}$
Shaft	7.07	0.00	0.00	0.00	0.00
Channel	-1.77	0.00	-0.24	0.00	0.42
Tendon A	-0.05	0.00	0.76	0.00	-0.04
Tendon B	-0.05	1.00	-0.24	-0.05	0.01
Tendon C	-0.05	0.00	-1.24	0.00	0.06
Tendon D	-0.05	-1.00	-0.24	0.05	0.01
Sensor A	-0.25	-0.96	0.57	0.24	-0.14
Sensor B	-0.25	0.96	0.57	-0.24	-0.14
Summation	4.61			0.00	0.19

Looking at Tbl. 2.2 above in conjunction with Fig. 2.9, it becomes clear how the geometric decomposition approach works. Take the "Shaft" element in Tbl. 2.2, for example. It represents the only solid section, and its centroid lies on the origin. Its position is not corrected by the weighting process, as it already lies on the reference origin. Conversely, the "channel" element represents the largest void, the working channel. Its centroid lies on the y-axis, in the lower half of the section, at (0,-0.24). This implies that the lower half of the section has less "solid" area than the top half. When we weight the centroid by the area, we get a positive displacement in the y-direction. Averaging the two segments' centroid positions would show that it has shifted upwards on the y-axis, away from the void's centroid, and towards the concentration of "solid" area near the top of the section.

Once all of the segments have been found and weighted, they are averaged to find the centroid coordinates as indicated in Tbl. 2.2.

$$C_x = \frac{-0.05 + 0.05 + 0.24 - 0.24}{4.61} = 0\text{mm} \quad (2.19)$$

$$C_y = \frac{0.42 - 0.04 + 0.01 + 0.06 + 0.01 - 0.14 - 0.14}{4.61} = 0.041\text{mm} \quad (2.20)$$

Therefore, the centroid of the section lies at $(0, 0.041)$, i.e. on the vertical centreline and just above the origin. With the location of the centroid, we can modify Eqns. 2.13 - 2.16.

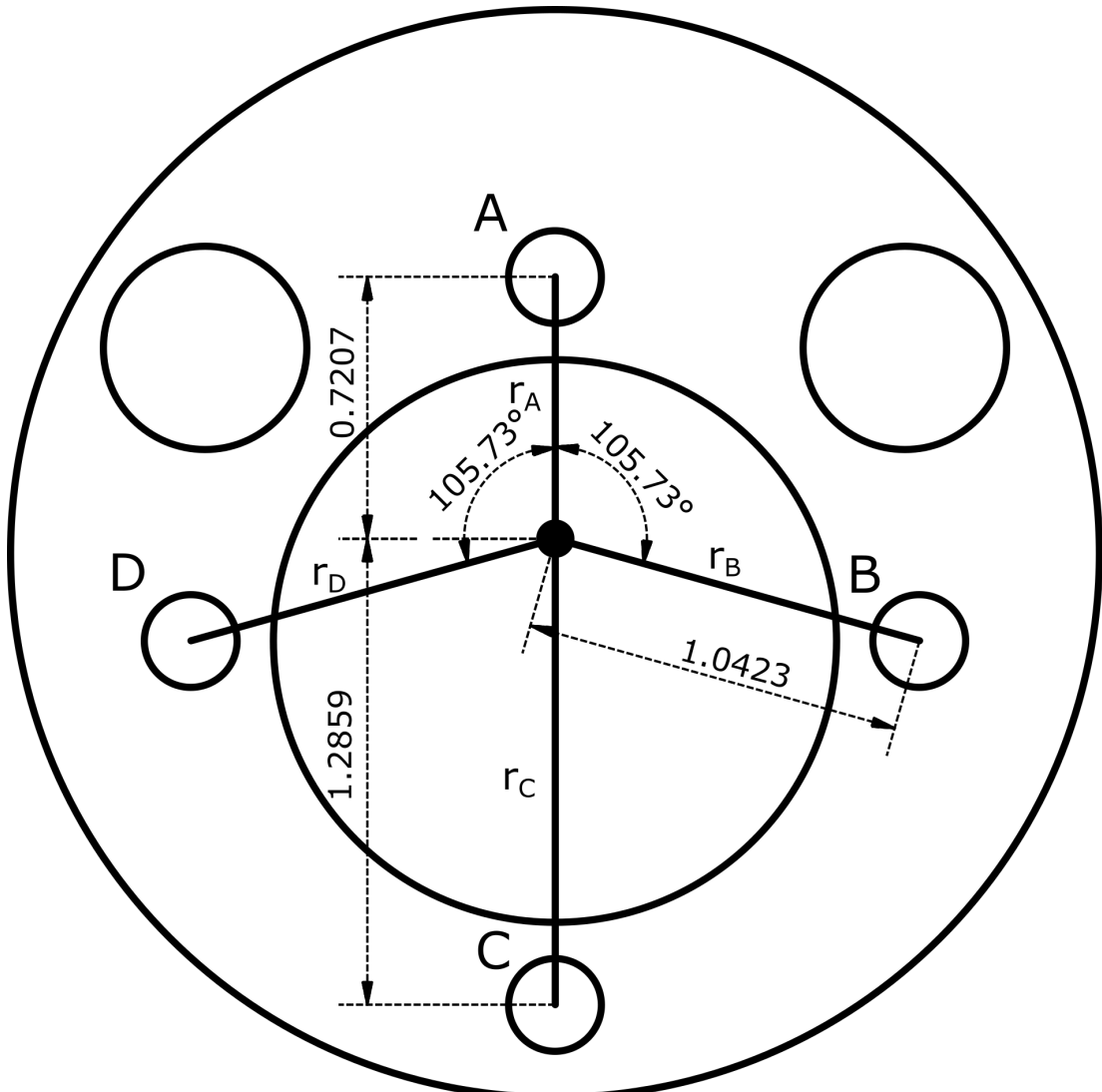


Figure 2.9: Section of the experimental catheter supplied by Teleflex OEM. Note that the centroid is displaced upwards by 0.041 mm due to the asymmetry of the section.

D_A changes little; the only difference is that $r_A = 0.72$ mm:

$$D_A = -\frac{\pi\theta 0.72 \cos(\alpha)}{180} \quad (2.21)$$

Tendon B is no longer separated from tendon A through an offset of 90° (see Eqn. 2.14), but through 105.73° . $r_B = 1.04$ mm.

$$D_B = -\frac{\pi\theta 1.04 \cos(105.73 - \alpha)}{180} \quad (2.22)$$

Tendon C is located at 180° , and $r_C = 1.29$ mm.

$$D_C = \frac{\pi\theta 1.29 \cos(\alpha)}{180} \quad (2.23)$$

Finally, tendon D is located at 254.27° from tendon A, and $r_D = 1.04$ mm

$$D_D = -\frac{\pi\theta 1.04 \cos(254.27 - \alpha)}{180} \quad (2.24)$$

Graphing equations 2.21 through 2.24 shows a similar pattern to Fig 2.7

Tendon displacement for any direction ($0^\circ \leq \alpha \leq 360^\circ$) at $\theta = 90^\circ$

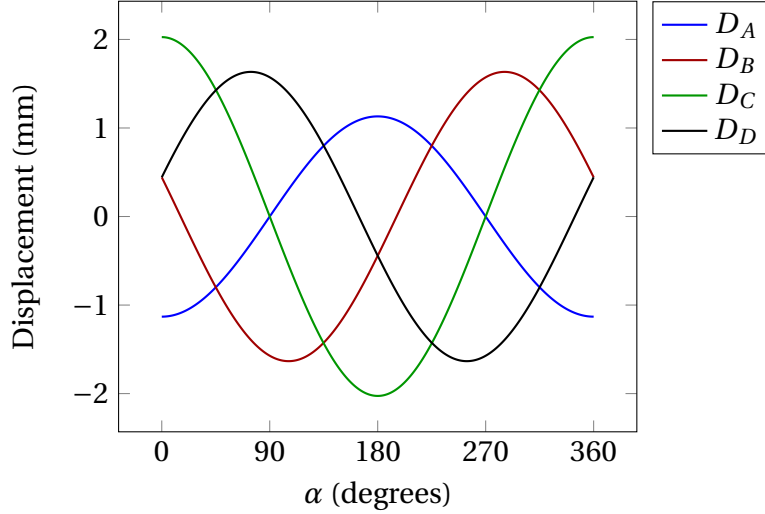


Figure 2.10: A plot of the tendon deflection at $\theta = 90^\circ$

2.2.4 Catheter model limitations and assumptions

The model detailed in section 2.2.2 suffers from certain limitations arising out of the manner in which the geometry of the articulating section is analysed (see Fig. 2.6 and

Fig. 2.9). It does not, for example, take into account the elongation of the tendons due to the tensile loading they are exposed to, nor does it consider the possibility of the catheter being bent anywhere other than at the articulating section - both are problems, as in the real world, the tendons do stretch under load, and the catheter is almost never straight along its whole length. Furthermore, the shaft and articulating section will compress due to the axial force of the tendon.

2.2.4.1 Axial tendon elongation under load

The catheter tendons, pictured in Fig. 2.2, are 0.007" (0.1778 mm) in diameter, and constructed of stainless steel grade 304. Tendons, as the name implies, can actuate the tip of the catheter only using tension (that is, we cannot push on the wire to cause a tip deflection). As a result, we only need to consider the tensile load on the tendon as governed by Young's modulus, E in Eqn. 2.25.

$$E = \frac{\sigma}{\epsilon} \quad (2.25)$$

where:

E = Young's Modulus (Pa)

σ = Stress (Pa)

ϵ = Strain (m/m)

In direct tension,

$$\sigma = \frac{F}{A} \quad (2.26)$$

and

$$\epsilon = \frac{\Delta L}{L} \quad (2.27)$$

where:

F = Force (N)

A = Cross-sectional area of tendon (m^2)

L = Initial length of the tendon(m)

ΔL = Change in length of the section (m)

Substituting Eqns. 2.26 and 2.27 into Eqn. 2.25 and simplifying yields the following expression for tendon elongation ΔL due to tensile loading:

$$E = \frac{F}{\frac{A}{\frac{\Delta L}{L}}} \quad (2.28)$$

$$\Delta L = \frac{FL}{AE} \quad (2.29)$$

Assuming the following values for each tendon:

F The tendon force should not exceed 10N

L Tendon Length is approximately 1.05m (see Fig. 2.2)

A Tendon diameter is 0.1778 mm - its cross-sectional area is 24.829×10^{-9} m²

E For Stainless Steel 304 is between 193 and 200 GPa [41]

At peak expected load and lowest Young's modulus (conservative estimate) this can cause an elongation of up to:

$$\Delta L = \frac{(10)(1.05)}{(24.829 \times 10^{-9})(193 \times 10^9)} = 2.191\text{mm} \quad (2.30)$$

Needless to say, this cannot simply be ignored - the peak change in length alone is comparable to the entire tendon displacement required for a 90° deflection (See Fig. 2.11). Clearly, the model needs to be amended to reflect this change in length.)

Fortunately, Eqn. 2.30 is relatively easy to incorporate into Eqns. 2.21 to 2.24:

$$D_A - \Delta L_A = -\frac{\pi\theta0.72\cos(\alpha)}{180} - \frac{F_AL}{AE} \quad (2.31)$$

$$D_B - \Delta L_B = -\frac{\pi\theta1.04\cos(105.73 - \alpha)}{180} - \frac{F_BL}{AE} \quad (2.32)$$

$$D_C - \Delta L_C = \frac{\pi\theta1.29\cos(\alpha)}{180} - \frac{F_CL}{AE} \quad (2.33)$$

$$D_D - \Delta L_D = -\frac{\pi\theta1.04\cos(254.27 - \alpha)}{180} - \frac{F_DL}{AE} \quad (2.34)$$

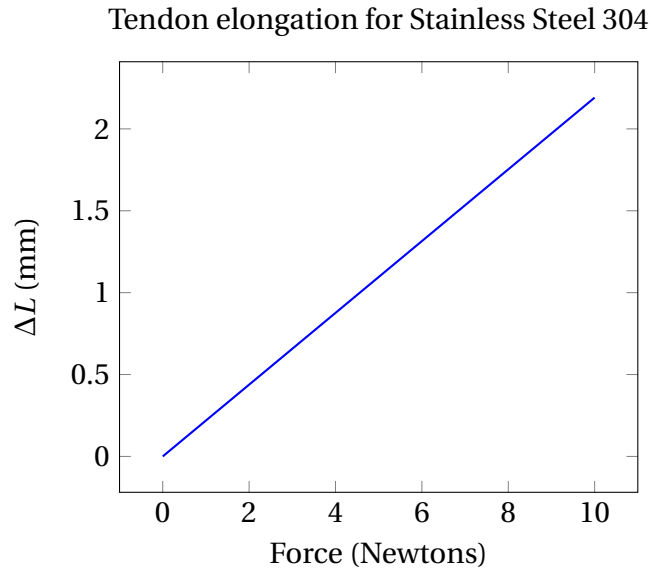


Figure 2.11: Plot of tendon elongation vs force applied

2.2.4.2 Lateral tendon shrinkage under load

The tendon's cross-sectional area may decrease with increasing force. As an isotropic material is stretched, its cross-section will shrink, as governed by Poisson's ratio ν (the ratio of transverse to axial strain).

$$\nu = \frac{\epsilon_{Transverse}}{\epsilon_{Axial}} \quad (2.35)$$

For a tendon of circular cross-section,

$$\nu = \frac{\frac{\Delta d}{d}}{\frac{\Delta L}{L}} \quad (2.36)$$

$$\nu \frac{\Delta L}{L} = \frac{\Delta d}{d} \quad (2.37)$$

$$\Delta d = -d\nu \frac{\Delta L}{L} \quad (2.38)$$

Note that the right hand-term in Eqn. 2.38 is negative due to the direction of change; an increase in tendon length causes a decrease in diameter.

Substituting the formula for the area of a circle into Eqn. 2.29:

$$\Delta L = \frac{4FL}{\pi d^2 E} \quad (2.39)$$

Substituting Eqn. 2.39 into 2.38:

$$\Delta d = -d \nu \frac{\frac{4FL}{\pi d^2 E}}{L} \quad (2.40)$$

Simplifying:

$$\Delta d = -\frac{4\nu F}{\pi d E} \quad (2.41)$$

Assuming typical values for the mechanical properties of AISI 304 stainless steel [41] used in the tendon design:

E 193-200 GPa

ν 0.29

As well as the maximum expected force (F) of approximately 10N and the tendon diameter (d) of 0.1778 mm specified in Fig. 2.2:

$$\Delta d = -\frac{4 \cdot 0.29 \cdot 10}{\pi \cdot 0.1778 \times 10^{-3} \cdot 193 \times 10^9} \quad (2.42)$$

$$\Delta d = -0.0001076 \text{ mm} \quad (2.43)$$

As the tendon material has a Young's modulus on the order of gigapascals, and the highest expected loading is in the low tens of newtons, Δd will remain on the order of tenths of microns. At this order of magnitude, the details of the change in tendon diameter are quite inconsequential, and can be safely ignored.

Chapter 3

Construction of a catheter testing apparatus

To validate the functionality of the catheter design and steering model outlined in sections 2.1 and 2.2, a testing rig was designed and built.

3.1 Actuation elements

The actuation assembly of the testing rig consists of four parallel linear motion axes, each comprising a RS Pro hybrid stepper motor (model no. 191-8340) and a metric size M6 threaded rod, coupled using an endless synchronous belt (ContiTech SynchroFlex 10/T5/150 SS) (See Fig. 3.1).

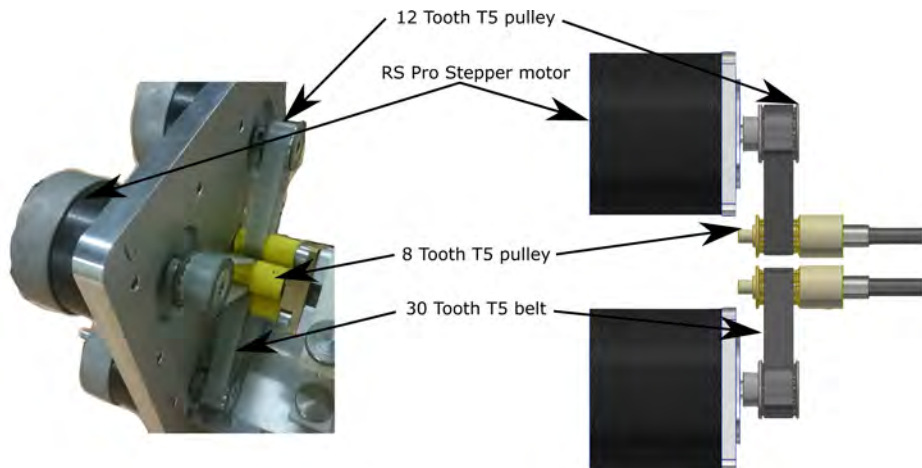


Figure 3.1: Photograph (left) and rendering (right) showing the actuation assembly.

The stepper motors are operated using a RAMPS (RepRap Arduino Mega Pololu Shield) 1.4 stepper motor carrier. These carrier boards interface with an Arduino Mega 2560, allowing the Arduino to neatly control up to five stepper motors. RAMPS 1.4 boards are widely used in open-source 3D printers, and are designed to operate at 12V. They can carry different types of stepper motor driver breakouts manufactured by Pololu Corp (Las Vegas, USA), such as those for the Texas Instruments DRV8825, which were used in this design. The DRV 8825 was chosen due to its high current capability (rated for 1.5A/coil, up to 2.2A/coil with adequate heat management, see [42]), and drop-in compatibility with the RAMPS board. Even though the DRV8825 is capable of microstepping up to 1/32, it was decided to keep the system in single-step mode, to maximise the motors' available torque output, thereby reducing the odds of inadvertently skipping steps and losing positional reference.

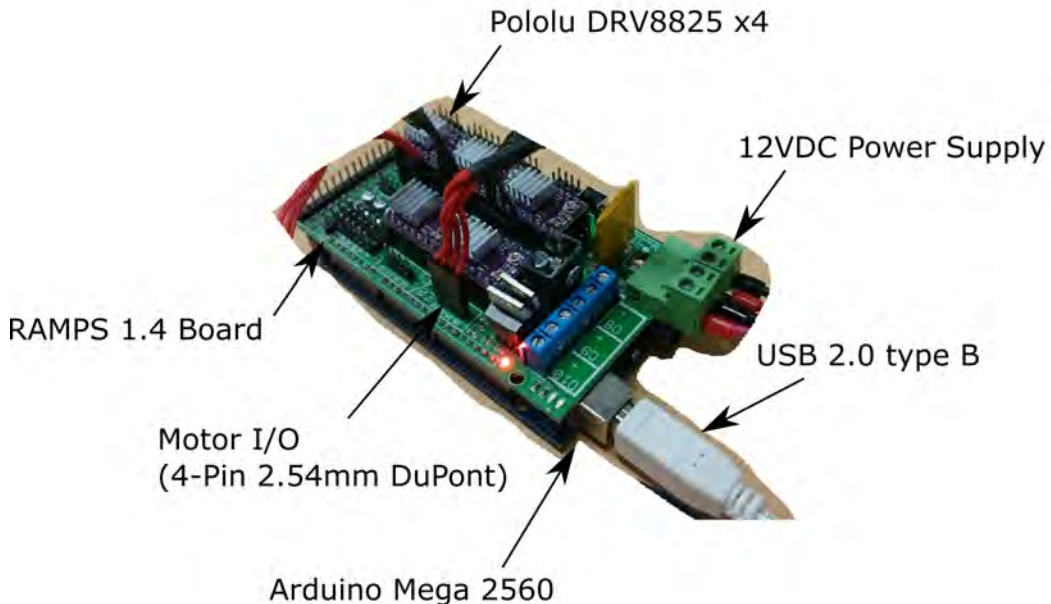


Figure 3.2: Closeup of the RAMPS 1.4 board used to drive the stepper motors.

As shown in Fig. 3.1, the motor and driven pulleys possess 12 and 8 teeth, respectively. This creates a transmission ratio - the output shaft spins faster than the input shaft, at a ratio of 12/8, i.e. every rotation of the *input* shaft causes the *output* shaft to rotate 1.5 times. As 200 steps of the motor equal 1.5 rotations of the leadscrew, one rotation of the leadscrew is equal to $\frac{200}{1.5} = 133.3\dot{3}$ steps. The pitch of the lead screw is 1 mm, meaning the linear axis travels one millimeter every 133.3 $\dot{3}$ steps.

3.2 Tendon force sensing

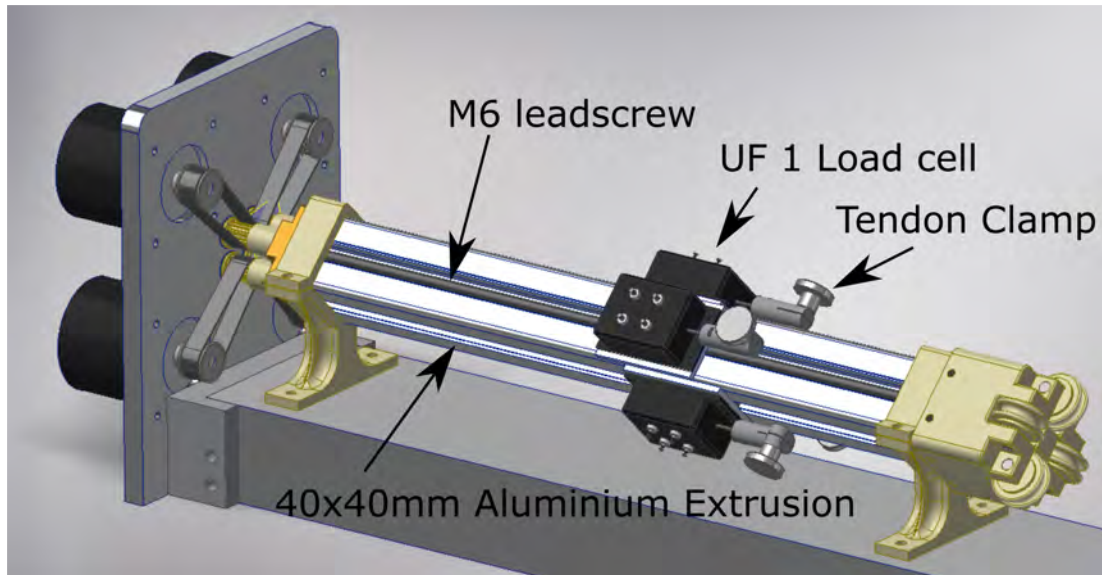


Figure 3.3: Rendered image of the whole actuation and force sensing assembly - Stepper motors and transmission on the left, linear motion axis, load cells and tendon attachment clamps on the right.

The force acting on each tendon was recorded using four UF1 Force sensors (LCM systems Ltd., Newport, Isle of Wight, UK). These force sensors have a range of 25g - 1500g (0.0245N-14.715N) and were positioned on the end of the linear axes, each with a 3D printed clamp to attach the tendons.

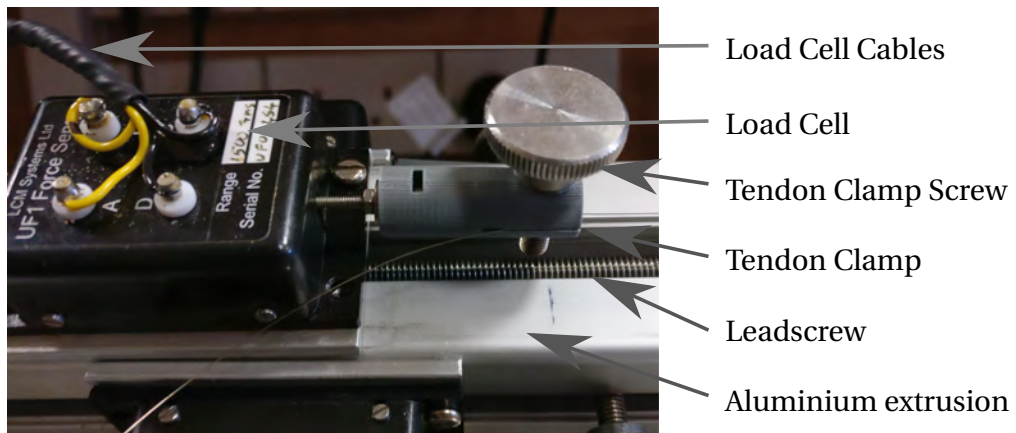


Figure 3.4: Closeup photograph showing the load cell and tendon clamp. The lead-screw is visible inside the aluminium profile slot.

3.2.1 Load cell electronics

The UF-1 load cells are a standard Wheatstone bridge-type sensor. Therefore, an INA 122 (Texas Instruments, Dallas, TX, USA) instrumentation amplifier was used to amplify the signal before feeding it to the ADS1015 analogue-to-digital converter. The circuit used is shown in Fig. 3.5. As the ADC is a sensitive component, it was decided to add a voltage divider to the output of the amplifier to limit the ADC input.

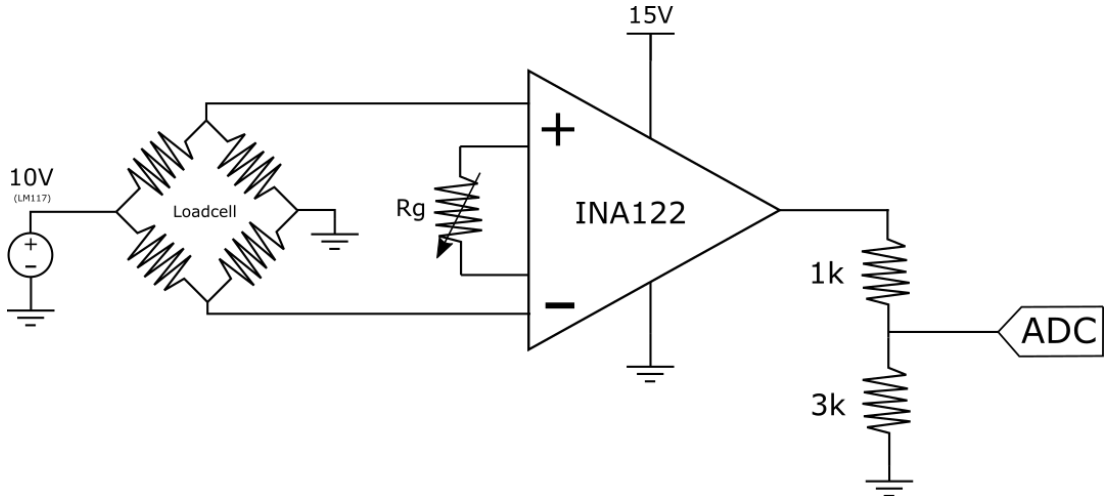


Figure 3.5: INA122 circuit used to amplify the load cell signal.

The 10V excitation voltage used for the load cells was supplied by a Texas Instruments LM117 adjustable regulator, configured as a high-stability 10V regulator, as suggested in the application notes on page 18 of the LM117 datasheet application notes [43]. As the output voltage of the load cell is directly dependent on the excitation voltage, it is highly important that this voltage is stable.

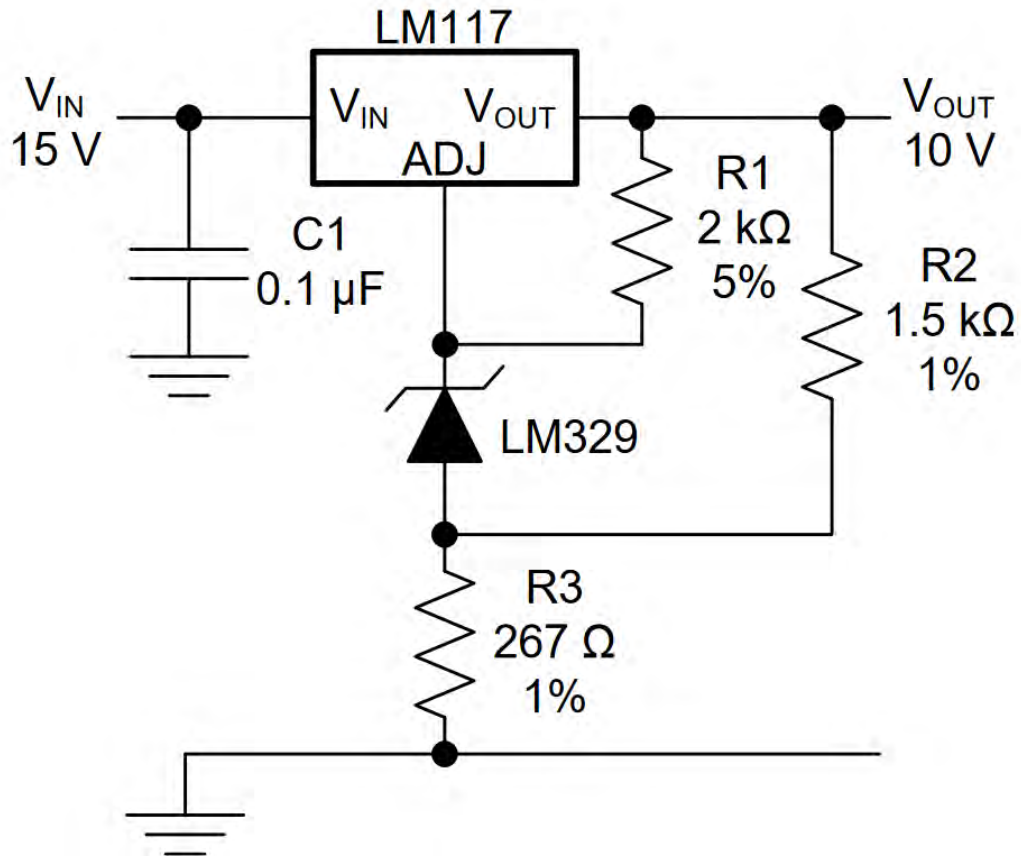


Figure 3.6: INA122 circuit used to amplify the load cell signal.

3.2.2 Load cell calibration

The load cells were calibrated using a simple set of laboratory weights, from 0g-1025g (0N-10.05N). In each case, the load cells were first loaded up to the full 10.05N, and the amplifier gain was adjusted until the ADS 1015 analogue-to-digital converter reached its maximum input reading. Next, the load cell was completely unloaded, and a zero reading was taken. Then the hanger (weighing 25g) was added, and another reading taken. Finally, weights were added and readings taken in 100g increments until the full load was again reached. This procedure was repeated for each load cell, and the results graphed in Fig. 3.7.

Table 3.1: load cell calibration data

Force (N)	0	0.25	1.23	2.21	3.19	4.17	5.15	6.13	7.11	8.09	9.07	10.05
Cell A	1	1	63	234	388	564	716	866	1030	1192	1336	1508
Cell B	1	1	60	240	405	554	707	879	1070	1239	1358	1511
Cell C	1	1	66	230	390	565	722	903	1048	1249	1379	1506
Cell D	83	98	255	383	510	665	870	1053	1183	1353	1429	1510

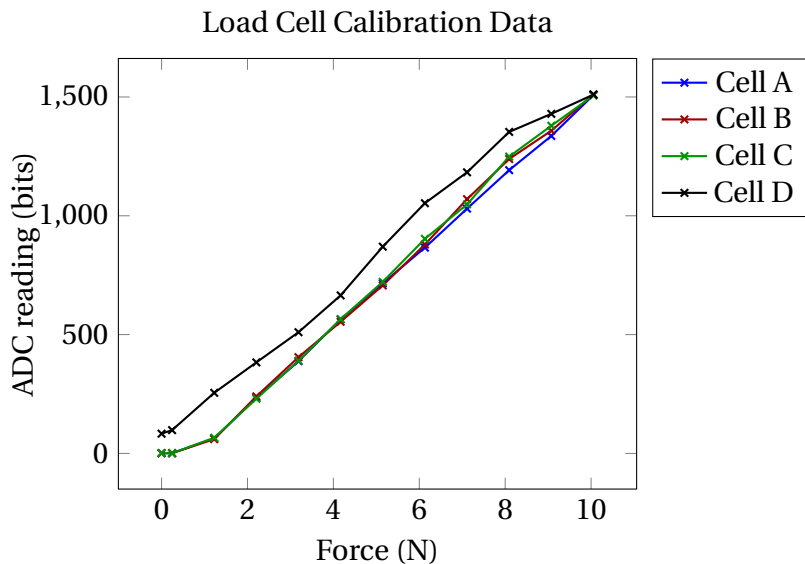


Figure 3.7: Plot of ADC reading vs. force applied to load cell

To convert the ADC reading back into a force value, a simple linear interpolation algorithm was used. In this implementation, the Arduino stores the data in Tbl.3.1 in five arrays, one for each row of the table. Each time the Arduino takes in an analogue reading from the ADC, it runs a series of comparisons which are detailed in Fig. 3.8.

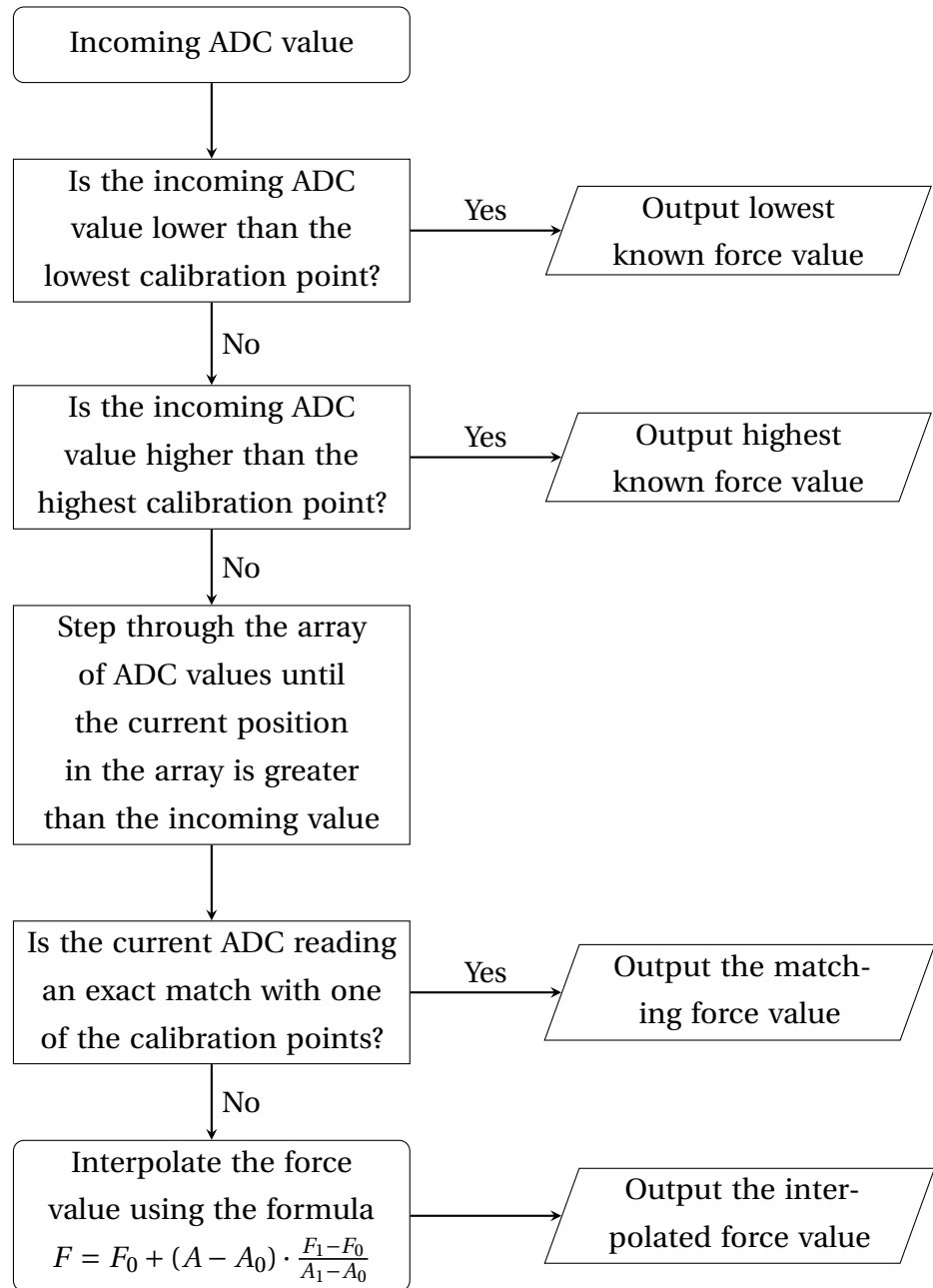


Figure 3.8: Flowchart of the linear interpolation logic used to convert ADC readings to force values

To save computing power and help prevent errors, the algorithm in Fig. 3.8 does not simply interpolate every incoming reading. Instead, it first looks at the available data and decides whether the incoming value falls within the calibrated range. If this is not the case, the highest or lowest available calibration point is sent to the output, as appropriate. Furthermore, if the incoming ADC reading exactly matches one of the calibration points, then that point is returned. Only after these logical checks have been completed does the algorithm continue to the interpolation step.

The interpolation formula seen in Fig. 3.8 refers specifically to linear interpolation between two known points, (A_0, F_0) and (A_1, F_1) .

The interpolation formula is as follows:

$$F = F_0 + (A - A_0) \cdot \frac{F_1 - F_0}{A_1 - A_0} \quad (3.1)$$

where:

F is the interpolated Force value in Newtons,

A is the incoming ADC reading in bits,

F_0 is the next lowest known force value in Newtons,

F_1 is the next highest known force value in Newtons,

A_0 is the next lowest ADC reading corresponding to a known force, and

A_1 is the next highest ADC reading corresponding to a known force.

For example, if $A = 1000$, $F_0 = 6.13$, $F_1 = 7.11$, $A_0 = 866$, and $A_1 = 1030$:

$$F = 6.13 + (1000 - 866) \cdot \frac{7.11 - 6.13}{1030 - 866} = 6.93\text{N} \quad (3.2)$$

Thereby interpolating a force reading from the calibration data and ADC reading.

3.3 Tip angle measurement

The final sensing components of the catheter testing rig serve to measure the angle of the catheter tip. It was originally planned to use three perpendicular cameras to track the catheter tip and retrieve both the angle representing the magnitude of deflection (θ), as well as its direction (α). This computer vision system was to be built using OpenCV in Visual Basic, using the OpenCV .NET wrapper EmguCV. Unfortunately, due to a combination of difficult-to-find documentation, time constraints and general unfamiliarity with machine vision systems, the functionality of this system was limited to just using one camera to measure the magnitude of tip deflection in single-tendon actuation mode. To supplement this shortcoming and provide tip position data tracking with more than just single-tendon actuation, it was instead decided to use the new Anser v1.0 electromagnetic tracking system built by UCC's Biodesign group.

3.3.1 Webcam-based tip angle measurement

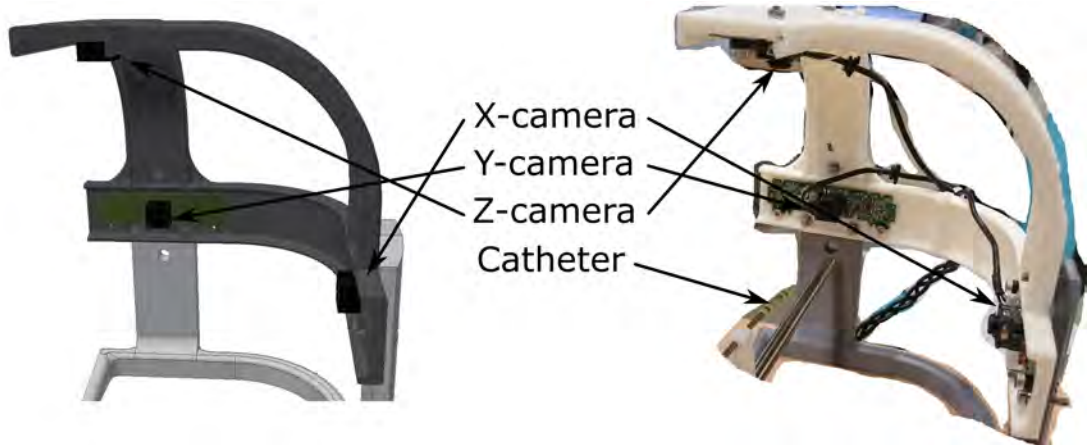


Figure 3.9: Image of the testing rig machine vision setup, render on the left, photograph on the right. Only the X camera was used to acquire data.

The camera rig in Fig. 3.9 consisted of three Logitech C920 webcams. The cameras were removed from their housings, leaving only the bare PCB with the camera module and supporting circuitry. The PCB was measured and matching recesses were modelled into the camera holder, which was subsequently 3D printed in Polylactide (PLA). The existing PCB mounting holes were used to mount the cameras in the 3D printed holder.

The catheter tip was marked using four rings of coloured heatshrink tubing, one pair on each side of the articulating section, with the rings of each pair separated by approximately 1 cm.

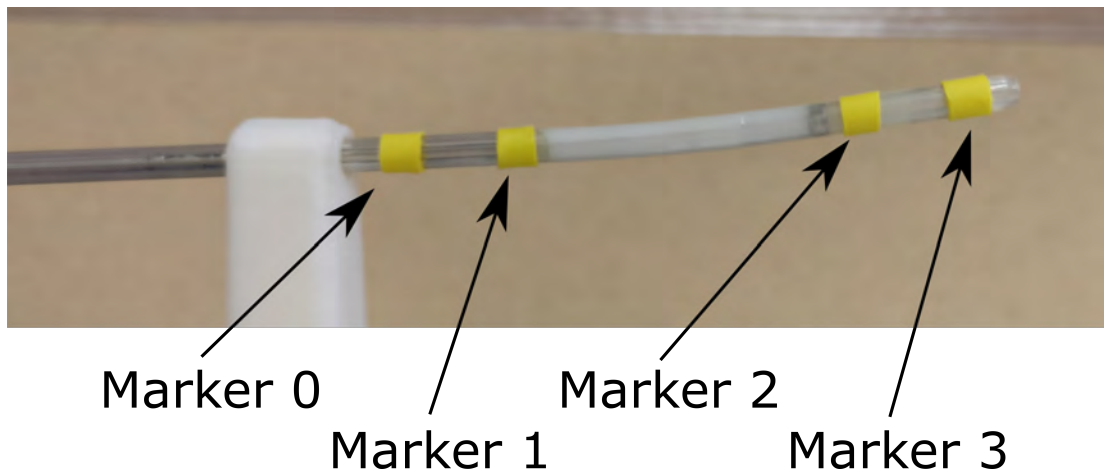


Figure 3.10: A closeup of the catheter tip with machine vision markers.

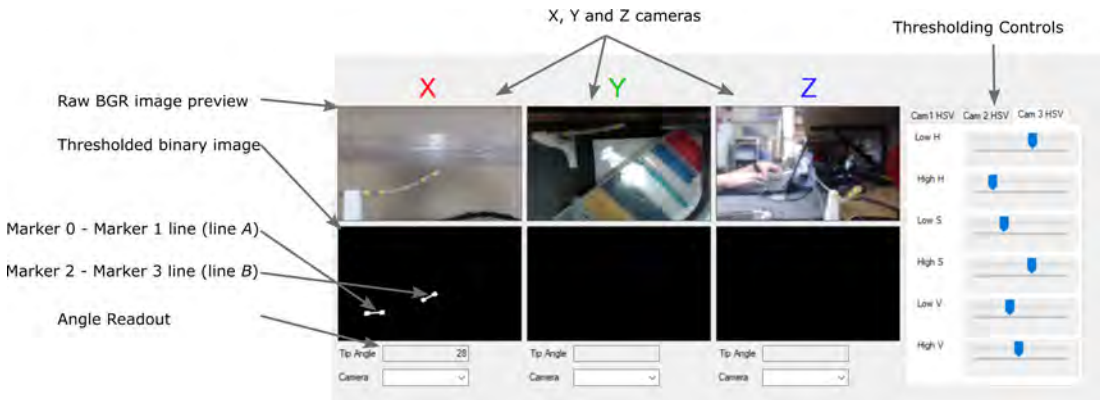


Figure 3.11: A screenshot of the machine vision GUI, showing the original image, the binarised image, the tip angle readout and the thresholding controls

The camera was set to capture frames at 20 frames per second. Each image is first directly sent to the GUI to permit the user a preview of the camera frame, and to allow any necessary angle or position adjustments to be made on-the-fly.

Next, the captured frame is converted from its current encoding (Blue-Green-Red, BGR) to (Hue-Saturation-Value, HSV) format. The GUI is polled to check the position of the thresholding sliders. These sliders set the minimum and maximum Hue, Saturation, and Value (brightness) levels. The thresholds specified by the user are applied by the program to binarise the image, i.e. convert it to a purely black and white image, with no intermediate brightness levels. If a pixel falls within the user-specified HSV range, it is given a 1, i.e. white. If it does not, it is assigned a 0 (black). This permits the system to distinguish features of the correct colour (namely, the marker rings) from features of the wrong colour (everything else).

Next, the binarised image is dilated and eroded; dilation causes all areas with a positive (white) pixel to swell, while erosion causes these areas to shrink again. When this process is iterated several times, noise is reduced and individual areas of the selected colour are isolated.

Once the dilate/erode operation is complete, the binary image is also sent to the GUI. This allows the user to dial in the HSV thresholds to home in on the selected marker colour.

By now, if the thresholds were set correctly, the binarised image of the catheter tip and markers has been reduced to only four "blobs" in an otherwise black frame. Each of these blobs possesses a contour - a curve around the boundary of the blob. The program uses these boundaries to identify each blob as a cohesive mass, and not just

an otherwise disparate group of white pixels. If the program has found four of these (one for each marker), it continues to find the centre of mass of each contour, and returns its X and Y coordinates in the frame. (OpenCV defines its coordinate origin as the top left corner of the image; the X-axis is positive to the right, while the Y axis is positive downward.) The centre of mass of each contour is then stored in an array for the next step.

As we know that the first two markers are part of the catheter shaft and the other two are affixed to the distal tip, we assume collinearity between markers 0 and 1 (line *A*), and between markers 2 and 3 (line *B*) (see Fig. 3.11). The angle θ_{xi} of line *i* between the points (x_{0i}, y_{0i}) and (x_{1i}, y_{1i}) relative to the *X* axis is described by the inverse tangent function:

$$\theta_{xi} = \tan^{-1}\left(\frac{y_{0i} - y_{1i}}{x_{0i} - x_{1i}}\right) \quad (3.3)$$

Finally, the angle θ between lines *A* and *B* is calculated by taking the absolute difference of their respective angles to the *X* axis (θ_{xA} and θ_{xB}) (see Eqn. 3.4).

$$\theta = |\theta_{xA} - \theta_{xB}| \quad (3.4)$$

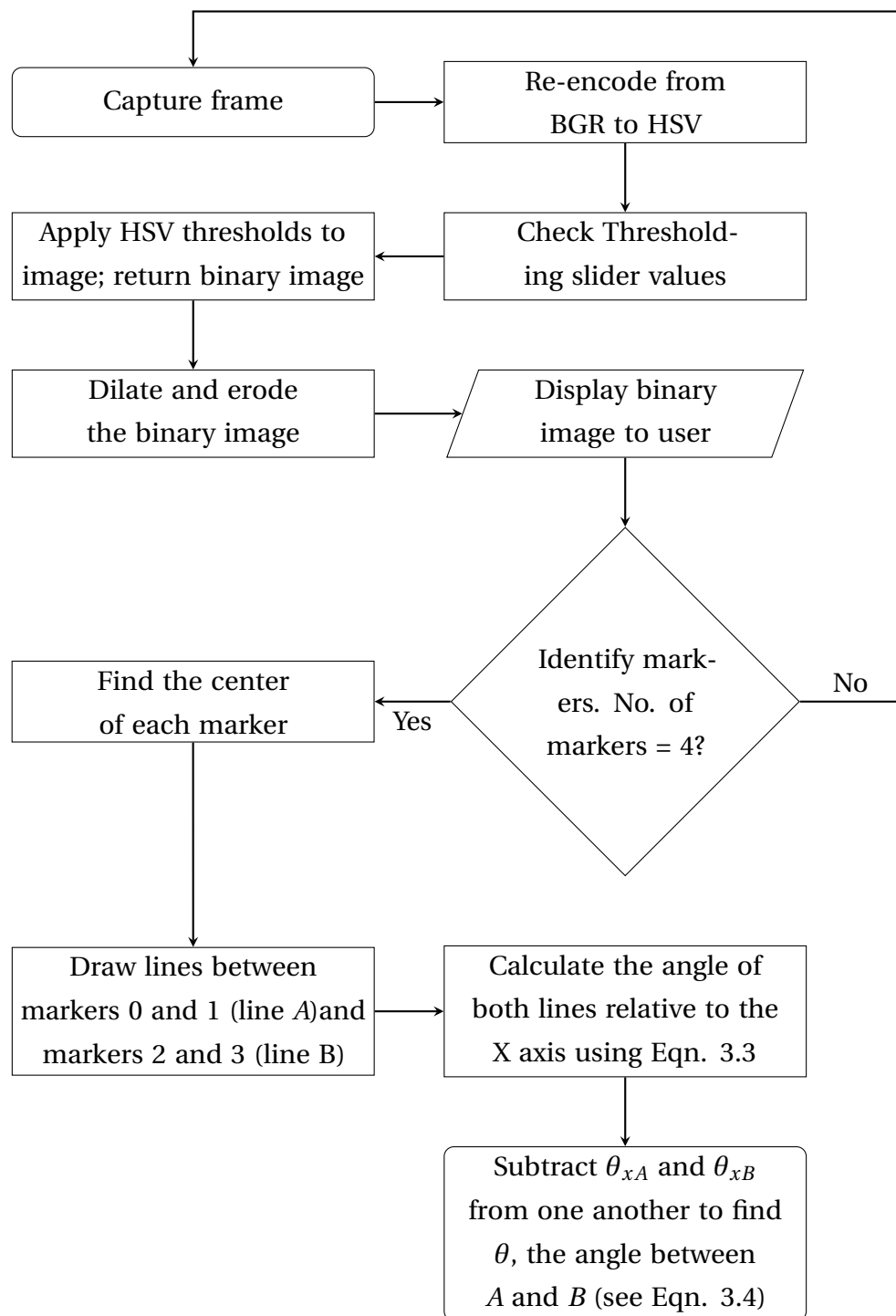


Figure 3.12: Flowchart of the OpenCV tip angle-finding algorithm

3.3.2 EM-tracked tip angle measurement

In order to gather data on the catheter's behaviour under multi-tendon deflection, the Anser electromagnetic tracking system was used. Two 5 degree-of-freedom sensors (NDI Inc., part no. 610099) were attached to the catheter, immediately proximal and distal to the articulating section (see Fig. 3.13). Sensor position was tracked at a rate of 60 Hz, and logged to a .csv file. Sensor position and attitude was represented using a combination of Cartesian and spherical coordinates, taking the form of a vector (x, y, z, θ, ϕ) (where x, y and z are the traditional 3-dimensional coordinates, and θ and ϕ are the elevation (pitch) and azimuth (yaw) angles of the sensor, respectively).

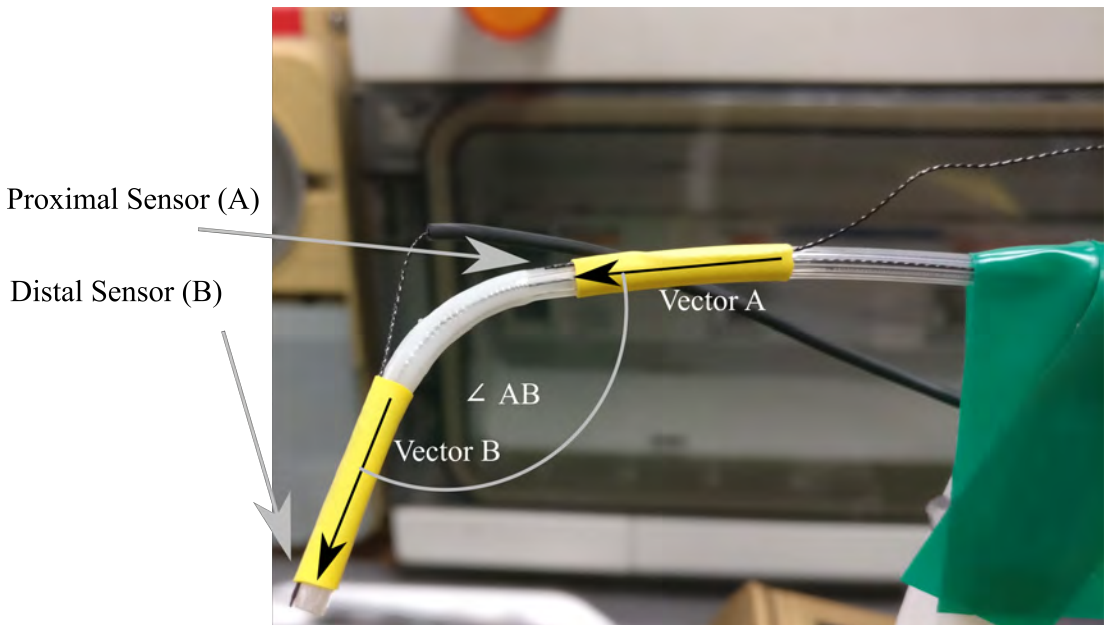


Figure 3.13: Closeup photograph of a catheter tip with two NDI 610099 5 degree-of-freedom sensors attached.

Once the coordinates of the two sensors have been found, the angle between them must be calculated. To this end, the vector components along the x , y and z axes must first be extracted from the elevation and azimuth data.

$$i = \cos(\phi) \cdot \sin(\theta) \cdot r \quad (3.5)$$

$$j = \sin(\phi) \cdot \sin(\theta) \cdot r \quad (3.6)$$

$$k = \cos(\theta) \cdot r \quad (3.7)$$

where:

- r is the magnitude of the vector,
- i is the vector component along the x axis,
- j is the vector component along the y axis,
- k is the vector component along the z axis,
- θ is the elevation angle (in radians) of the vector, and
- ϕ is the azimuthal angle (in radians) of the vector.

With the vector components we can find the dot product of \vec{A} and \vec{B} :

$$\vec{A} \cdot \vec{B} = i_A i_B + j_A j_B + k_A k_B \quad (3.8)$$

The angle of tip deflection can be calculated as follows:

$$\vec{A} \cdot \vec{B} = \|\vec{A}\| \cdot \|\vec{B}\| \cdot \cos(\angle AB) \quad (3.9)$$

where:

- \vec{A} is the vector of the catheter shaft proximal to the articulating section,
- \vec{B} is the vector of the catheter tip, distal to the articulating section,
- $\|\vec{A}\|$ is the magnitude of \vec{A} ,
- $\|\vec{B}\|$ is the magnitude of \vec{B} , and
- $\angle AB$ is the angle between \vec{A} and \vec{B} , i.e. the angle of tip deflection.

As the length of the vector representing a sensor is arbitrary and does not hold any inherent significance, it was simply fixed at $r = \|\vec{A}\| = \|\vec{B}\| = 1$ for the sake of convenience.

Rearranging Eqn. 3.9 to isolate $\angle AB$ yields:

$$\angle AB = \cos^{-1} \left(\frac{\vec{A} \cdot \vec{B}}{\|\vec{A}\| \cdot \|\vec{B}\|} \right) \quad (3.10)$$

As an example calculation, consider the two vectors \vec{A} and \vec{B} , expressed in the format $\vec{n} = (x, y, z, \theta, \phi)$:

$$\vec{A} = (0.048, 0.027, 0.163, 1.526, 3.113)$$

$$\vec{B} = (0.014, 0.035, 0.168, 1.429, 2.922)$$

First, the vector components along the x , y and z axes must be calculated using Eqns. 3.5 to 3.7:

$$\begin{aligned} i_A &= \cos(3.113) \cdot \sin(1.526) \cdot 1 = -0.999 \\ j_A &= \sin(3.113) \cdot \sin(1.526) \cdot 1 = 0.029 \\ k_A &= \cos(1.526) \cdot 1 = 0.045 \\ i_B &= \cos(2.922) \cdot \sin(1.429) \cdot 1 = -0.966 \\ j_B &= \sin(2.922) \cdot \sin(1.429) \cdot 1 = 0.216 \\ k_B &= \cos(1.429) \cdot 1 = 0.141 \end{aligned} \tag{3.11}$$

Next, the vector components are used to find $\vec{A} \cdot \vec{B}$:

$$\begin{aligned} \vec{A} \cdot \vec{B} &= i_A i_B + j_A j_B + k_A k_B \\ \vec{A} \cdot \vec{B} &= (-0.999)(-0.966) + (0.029)(0.216) + (0.045)(0.141) \\ \vec{A} \cdot \vec{B} &= 0.978 \end{aligned} \tag{3.12}$$

Finally, we can substitute this information into Eqn. 3.10. Recall that the vectors are of unit length, i.e. $\|\vec{A}\| = \|\vec{B}\| = 1$:

$$\begin{aligned} \angle AB &= \cos^{-1} \left(\frac{\vec{A} \cdot \vec{B}}{\|\vec{A}\| \cdot \|\vec{B}\|} \right) \\ \angle AB &= \cos^{-1} \left(\frac{0.978}{1} \right) \\ \angle AB &= 12.03^\circ \end{aligned} \tag{3.13}$$

Finding the direction of deflection of the catheter tip is somewhat more complicated. First, a reference plane is chosen. This reference plane represents the plane of

deflection where α (as defined in section 2.2.2) is zero. The reference plane normal \vec{N} is the cross product of \vec{A} to \vec{B} when the catheter is deflected only by tendon A (as indicated in Fig. 2.9), with all other tendons slack:

$$\vec{N} = \vec{A}_{ref} \times \vec{B}_{ref} \quad (3.14)$$

During testing \vec{A} and \vec{B} are recorded, and the normal of each plane, \vec{n} , is calculated again by taking the cross product of \vec{A} to \vec{B} .

$$\vec{n} = \vec{A} \times \vec{B} \quad (3.15)$$

Typically, the angle of the plane of deflection to the reference plane is just:

$$\alpha = \cos^{-1}\left(\frac{\vec{n} \cdot \vec{N}}{\|\vec{n}\| \cdot \|\vec{N}\|}\right) \quad (3.16)$$

Due to the mathematical limitations of this formula, α will always be less than 180°. In this case, however, we also need to know the *direction* of the angle. To solve this problem, we first project \vec{n} and \vec{N} on to a plane defined by \vec{A} as its normal vector:

$$\vec{n}_{proj} = \vec{n} - \frac{\vec{n} \cdot \vec{A}}{\|\vec{A}\|^2} \vec{A} \quad (3.17)$$

$$\vec{N}_{proj} = \vec{N} - \frac{\vec{N} \cdot \vec{A}}{\|\vec{A}\|^2} \vec{A}$$

Next, we find the angle α between \vec{n}_{proj} and \vec{N}_{proj} :

$$\alpha = \cos^{-1}\left(\frac{\vec{n}_{proj} \cdot \vec{N}_{proj}}{\|\vec{n}_{proj}\| \cdot \|\vec{N}_{proj}\|}\right) \quad (3.18)$$

Finally, we must find the direction of the angle. To this end, we use the triple product

$$\vec{A} \cdot (\vec{N}_{proj} \times \vec{n}_{proj}) \quad (3.19)$$

If the triple product is negative, α has passed the 180° point as defined in Fig. 2.6,

and is subtracted from 360° to calculate the direction of deflection.

3.4 Software

The testing rig is controlled by a central GUI program written in Visual Basic. This program coordinates all of the rig's actions and gives the user real-time information on the rig's status. The program's functions include:

- Serial communication with load cell microcontroller
- Serial communication with stepper motor microcontroller
- Real-time display of testing data
- User input of tendon force setpoints
- PID control of tendon forces
- Data logging
- Computer vision data display
- Computer vision thresholding user interface

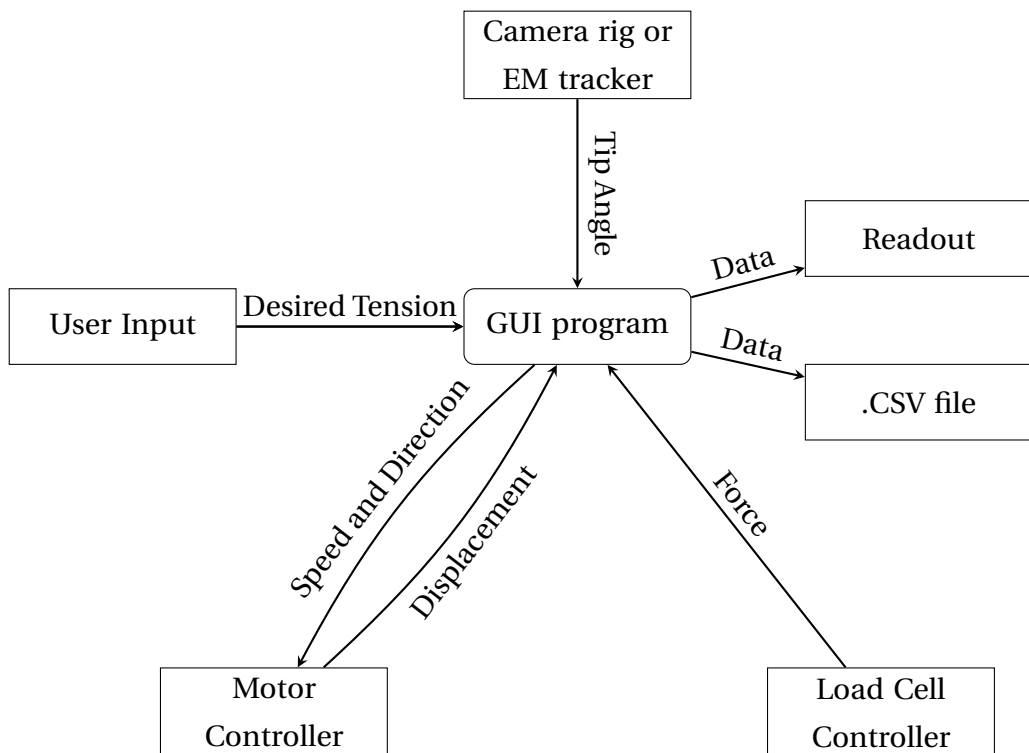


Figure 3.14: Graphic showing the interactions between individual testing rig elements

3.4.1 Graphical user interface (GUI)

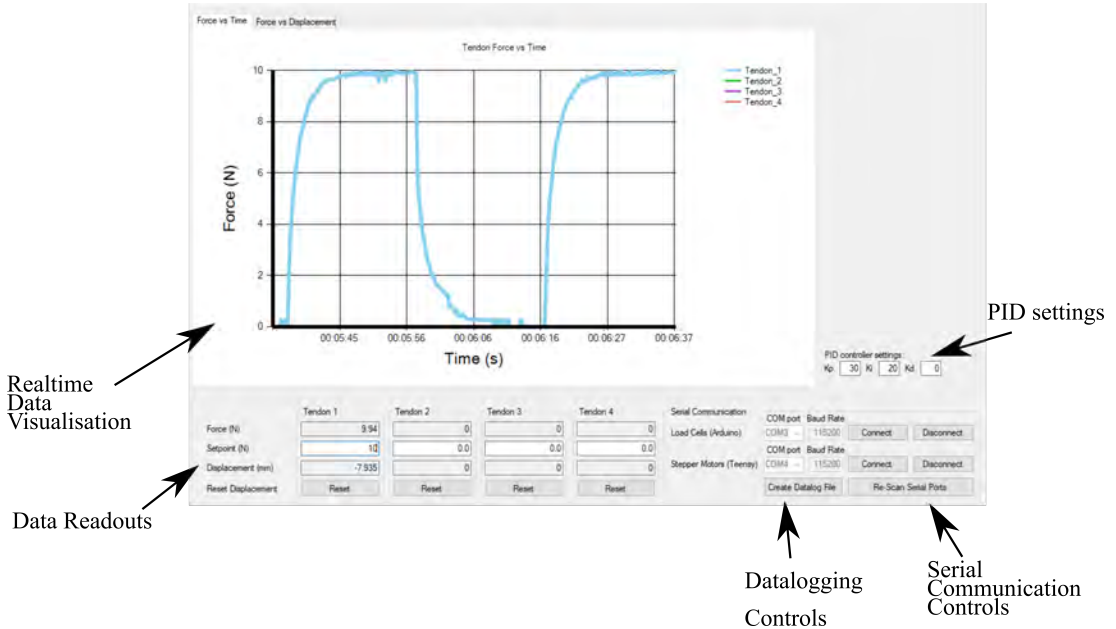


Figure 3.15: Screenshot of the testing rig's GUI in use

The GUI app's key functionality and layout is depicted in Figs. 3.14 and 3.15. It operates asynchronously, meaning that the user inputs and the individual segments of the testing rig do not need to coordinate their respective timings - each event is simply triggered when a new force measurement is received. Operating cycles take place in the following order:

1. The Arduino attached to the load cell takes a force reading
2. The GUI takes the incoming string, parses the separate force readings, and stores them in individual variables.
3. The Refresh_PID function is invoked into a parallel thread
 - (a) It polls the UI for the current PID controller gains as well as the current force setpoints,
 - (b) The PID controllers' outputs are then recalculated and stored in variables for later use.
 - (c) End thread
4. The Update_UI function is invoked into a parallel thread
 - (a) It updates the numeric force readouts
 - (b) It updates the tendon displacement readouts

- (c) It plots the newest force and displacement readings on the graph
 - (d) It removes data older than one minute from the graph, giving the illusion of the graph scrolling along the time axis
 - (e) It pushes the updated graph to the GUI, updating what the user can see.
 - (f) End thread
5. The Send_Motor_Control function is invoked into a parallel thread
- (a) It determines the direction of the PIDs' outputs (Increase / Decrease tension)
 - (b) It turns the absolute values of the PID outputs into a speed setting for the motors
 - (c) It polls the GUI to determine if any of the "Reset Displacement" buttons have been pushed and sets the reset flags accordingly
 - (d) It concatenates the speed, direction and displacement reset data into a string
 - (e) It sends this string to the arduino controlling the motors.
 - (f) It un-sets any displacement reset flags to ensure that each button press is only transmitted once.
 - (g) End thread
6. The Log_Data function is invoked into a parallel thread
- (a) It writes the current values for force, displacement and tip angle to a .csv file, followed by a newline character.

Tip angle is measured by the same program in a second window, shown in Fig. 3.11, using the algorithm described in section 3.3.1. This process takes place in a parallel thread to the main GUI.

3.4.2 PID controller

The testing rig controls the tension on the individual tendons of the catheter using the four linear axes described in sections 3.1 and 3.2. To achieve this force control, a simple pseudo-PID controller was implemented. This controller closely emulates the behaviour of a PID in a reasonably robust and performant way without the need for reliable timing. As an added benefit, it is exceedingly simple to code.

When the Arduino controlling the load cells sends a data packet to the PC running the GUI application, all the actions listed in section 3.4.1 are fired off in rapid succession. This leads to a brief loading spike on the CPU queue, made worse by the fact that all of these tasks have to spawn their own CPU thread that requires time to receive its RAM allocation on opening, and more time to release it on closing. While these issues are not particularly severe and still allow adequate performance, it does make accurate timing comparatively unreliable. As a result, it is far easier to implement a simplistic type of controller that disregards the time elapsed between PID calculations, and only works iteration-to-iteration.

A true PID controller's output is the sum of the proportional, integral and derivative terms multiplied by their respective gains. In operation, the time integral of the error signal is used to accumulate an offset on the controller's output to reduce or eliminate steady-state error. Likewise, the time derivative of the error signal is used to adjust controller output to reduce overshoot and provide damping. Finally, the proportional term is simply the product of the error and the proportional gain.

The pseudo-PID controller works mostly in the same manner. Its output is also the sum of three terms multiplied by their respective gains. Crucially however, it does not possess a time axis and is designed to be run at discrete times instead of continuously. This does not affect the proportional term - it is still just the product of the proportional gain and the error value. The "integral" term is calculated using a simple summation of all previously measured error values, and the "derivative" is the difference between the previous error and the current error. Its operational flow is depicted in Fig. 3.16.

Integral windup is managed by an additional logic step in the controller implementation. Before the final controller output summation, the controller checks the integral value. If it exceeds or falls under certain pre-set levels, the integral term will be set equal to the limit value. Furthermore, if the setpoint is changed, both the integral and derivative terms are re-initialised to 0.

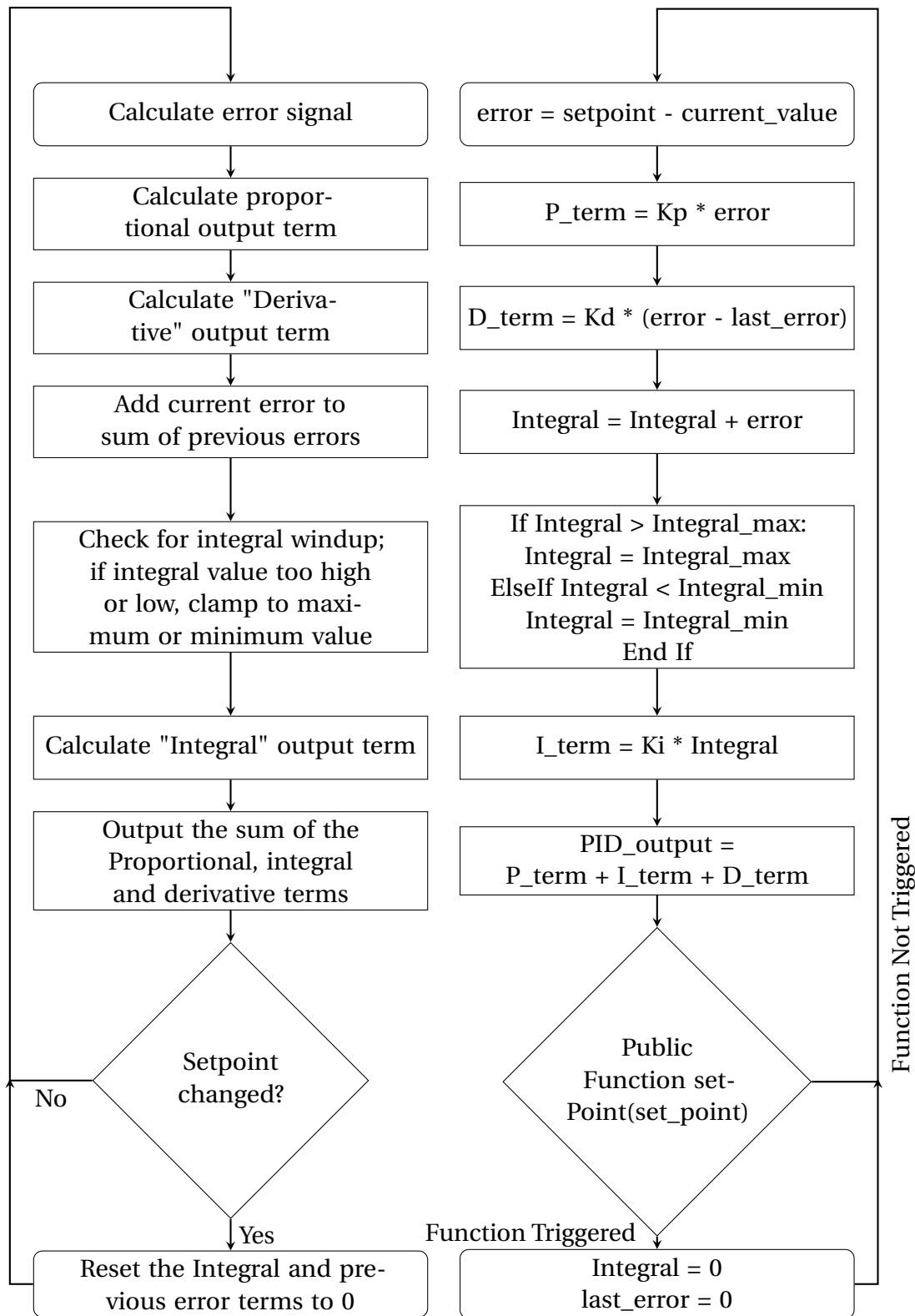


Figure 3.16: Flowchart of the PID control algorithm - concept on the left, software implementation on the right

Chapter 4

Catheter testing

4.1 Single-tendon loading

The catheter was tested in single tendon loading mode to compare the performance of a real catheter to the hypothesis established in section 2.2.

4.1.1 Method

First, the catheter to be tested was visually inspected for damage or manufacturing defects. Next, the catheter was fed through the alignment guides (one of which is visible to the left of Fig. 3.10) along its length and clamped into place on the proximal end to prevent axial motion of the shaft during testing (Fig. 4.1):

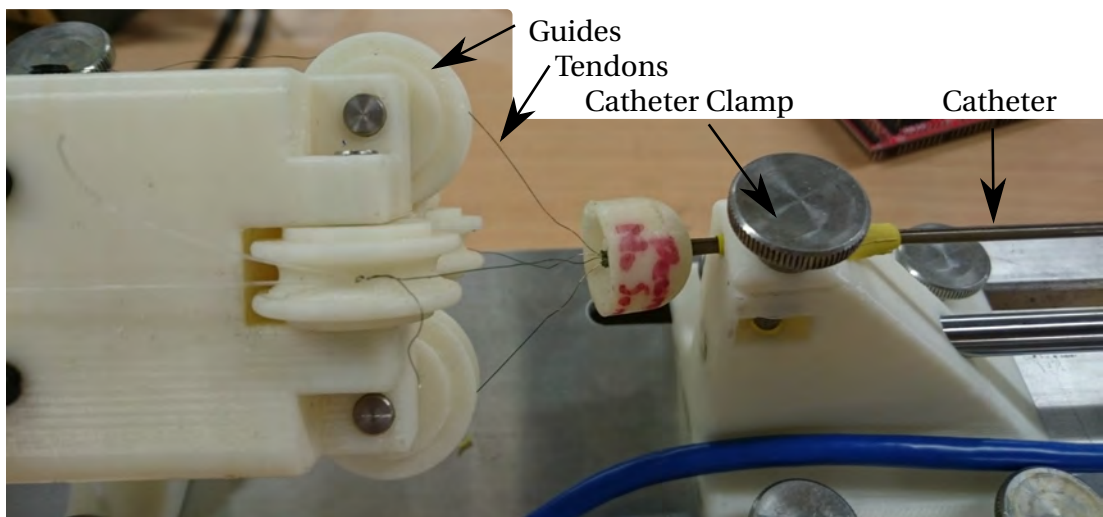


Figure 4.1: Catheter clamped into position on testing rig

Once the catheter was securely in place, the tendons themselves were attached to

the load cells by inserting the tendon through the slot of the tendon clamp (Fig. 3.4), taking care that the tendon was axially aligned with the load cell. The tendon being tested was then loaded to 2N to pre-tension the wire. Once the force reading stabilised, the tendon was unloaded to zero newtons, thereby removing any slack in the tendon.

The catheter tip was set up with coloured markers as shown in Fig. 3.10, and the camera thresholding was adjusted to include only the hue, saturation and value of the coloured markers (see Fig. 3.11).

With the tendon in place and prepared, the testing itself commenced. The tendon was loaded and unloaded between 10N and 0N for 25 iterations using an AutoHotkey (a programming language that permits automated keystroke simulation) script to automatically modify the setpoints input on the GUI. The script is shown in pseudocode below:

```

1 ^j::                      'when ctrl+J is pressed
2 n = 25                      'target number of iterations
3 i = 0                        'iterator
4 delay = 20000                'settling time in ms
5
6
7 while(i<n){
8 Send, 10                      '10N setpoint
9 Sleep %delay%                  'wait for the settling time
10 Send {BackSpace}               'delete the text in the input box
11 Send {BackSpace}
12 Send, 0                        '0N setpoint
13 Sleep %delay%                  'wait for the settling time
14 Send {BackSpace}               'delete the text in the input box
15 i++                           'increment counter
16 }
17 Send {BackSpace}               'delete everything when done
18 Send {BackSpace}
19 Send {BackSpace}
20 Send, 0                        'Finally relax the tendon
21
22 Return

```

4.1.2 Results

As the tension rig collects a large volume of data, the results shown here are limited to those used for the comparison between empirical data and the hypothetical model developed in section 2.2. Two catheters were tested. Tbl. 4.1 lists the graphs used to visualise the test results for each of the four tendons for both catheter units. Additional results are included in appendices A.1 and A.2.

There are two types of graph for each tendon. The first type (Figs. 4.2, 4.4, 4.6, 4.8, 4.10, 4.12, 4.14 and 4.16) shows the relationship between tendon displacement and tip deflection. The red series on these graphs show the tendon displacement as predicted by the unmodified tendon displacement model. The blue series show the real displacement of the tendon as measured during the experiment, and the green series show the predicted tendon displacement after lumped error compensation (this correction is explained in detail in section 4.1.5). The second type (Figs. 4.3, 4.5, 4.7, 4.9, 4.11, 4.13, 4.15 and 4.17) shows the prediction error over tip deflection. In this case, the blue series show the prediction error before compensation, and the green series show the prediction error after lumped error compensation.

4.1.3 Catheter 1

Table 4.2: Catheter 1 key data

Value	Tendon A	Tendon B	Tendon C	Tendon D
Avg. displacement at 10N (mm)	-6.7973	-8.6900	-8.5286	-7.0865
Avg. displacement at 0N (mm)	-0.6163	-1.5616	-0.7753	-0.8160
Avg. tip angle at 10N (°)	71.4224	88.8002	89.2466	70.2696
Avg. tip angle at 0N (°)	33.6658	28.1306	10.3164	12.0000

Table 4.1: List of figures for single-tendon testing

Catheter / Tendon	Fig.	Description
1A	4.2	Shows the real, predicted and compensated tendon displacement against tip angle for Catheter 1, Tendon A
1A	4.3	Shows the error in tendon displacement prediction for Catheter 1, Tendon A
1B	4.4	Shows the real, predicted and compensated tendon displacement against tip angle for Catheter 1, Tendon B
1B	4.5	Shows the error in tendon displacement prediction for Catheter 1, Tendon B
1C	4.6	Shows the real, predicted and compensated tendon displacement against tip angle for Catheter 1, Tendon C
1C	4.7	Shows the error in tendon displacement prediction for Catheter 1, Tendon C
1D	4.8	Shows the real, predicted and compensated tendon displacement against tip angle for Catheter 1, Tendon D
1D	4.9	Shows the error in tendon displacement prediction for Catheter 1, Tendon D
2A	4.10	Shows the real, predicted and compensated tendon displacement against tip angle for Catheter 2, Tendon A
2A	4.11	Shows the error in tendon displacement prediction for Catheter 2, Tendon A
2B	4.12	Shows the real, predicted and compensated tendon displacement against tip angle for Catheter 2, Tendon B
2B	4.13	Shows the error in tendon displacement prediction for Catheter 2, Tendon B
2C	4.14	Shows the real, predicted and compensated tendon displacement against tip angle for Catheter 2, Tendon C
2C	4.15	Shows the error in tendon displacement prediction for Catheter 2, Tendon C
2D	4.16	Shows the real, predicted and compensated tendon displacement against tip angle for Catheter 2, Tendon D
2D	4.17	Shows the error in tendon displacement prediction for Catheter 2, Tendon D

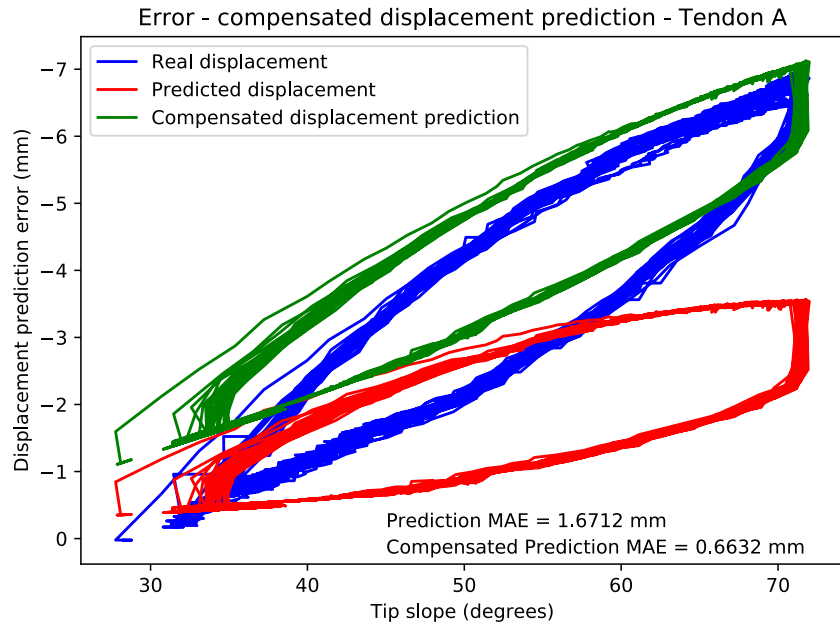


Figure 4.2: Graph of real, predicted and compensated predicted tendon displacement vs. tip deflection angle for Catheter 1, Tendon A

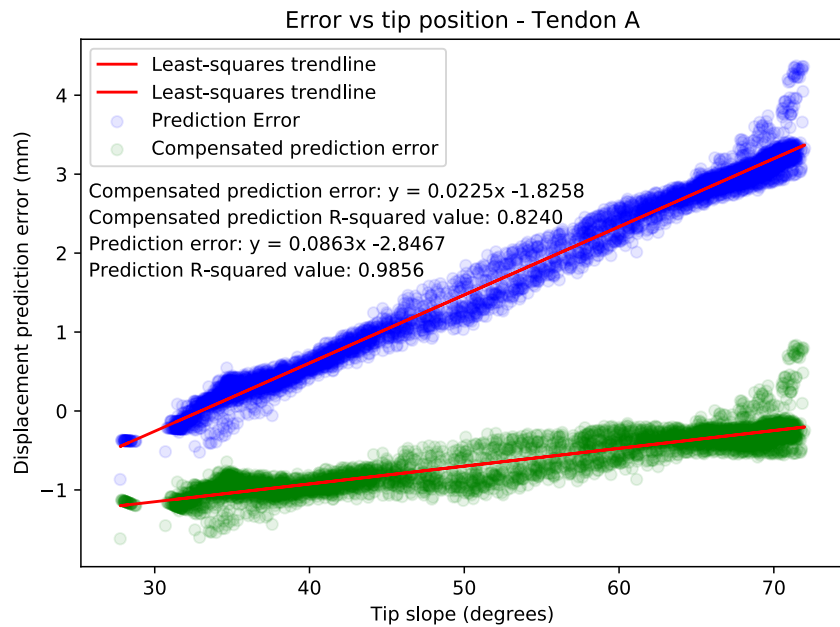


Figure 4.3: Displacement prediction error for Catheter 1, Tendon A

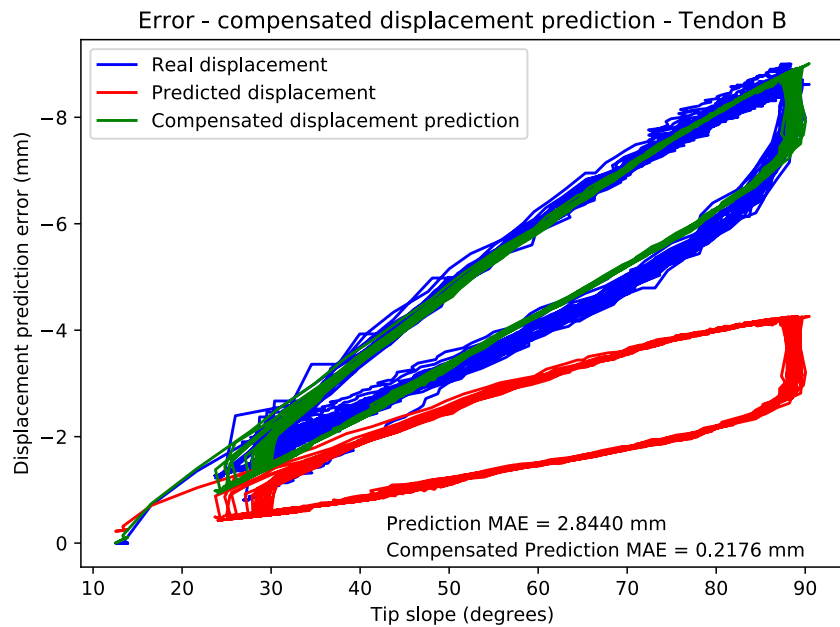


Figure 4.4: Graph of real, predicted and compensated predicted tendon displacement vs. tip deflection angle for Catheter 1, Tendon B

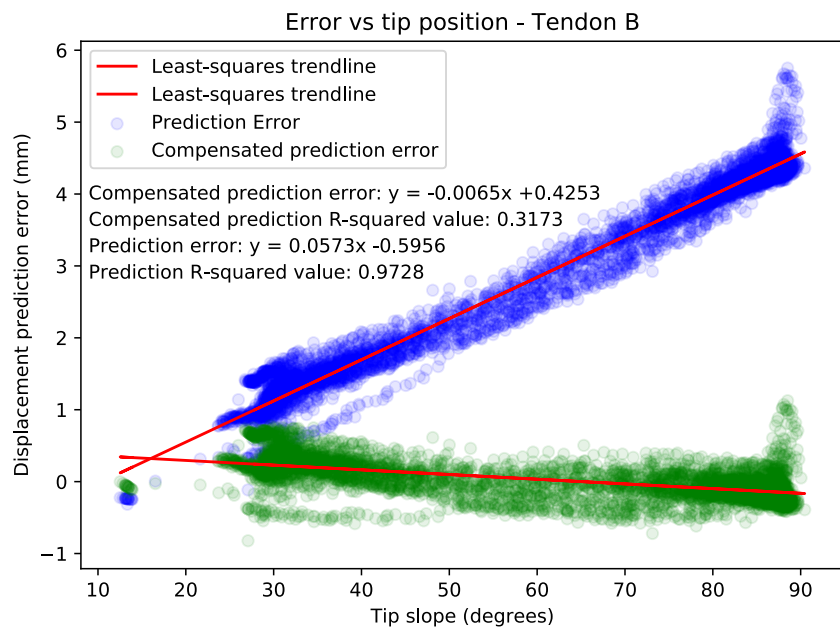


Figure 4.5: Displacement prediction error for Catheter 1, Tendon B

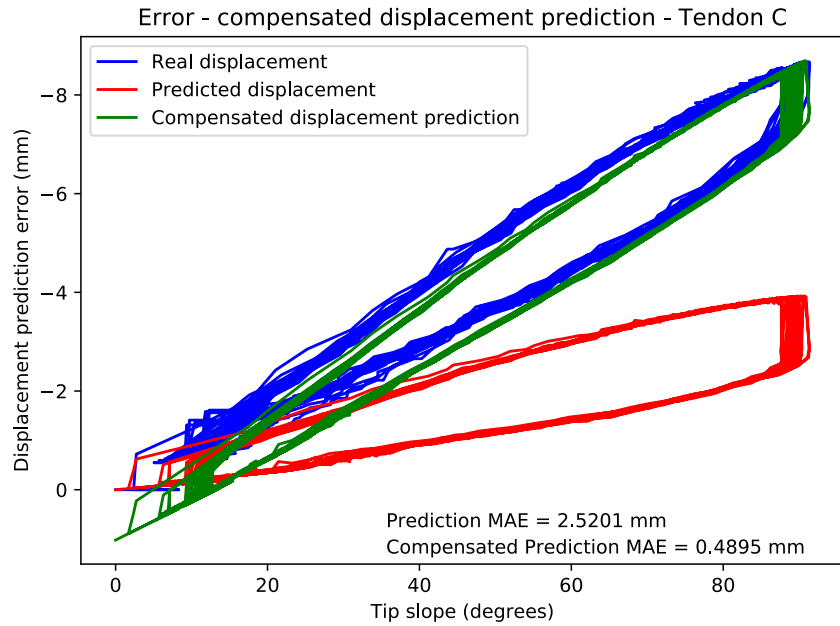


Figure 4.6: Graph of real, predicted and compensated predicted tendon displacement vs. tip deflection angle for Catheter 1, Tendon C

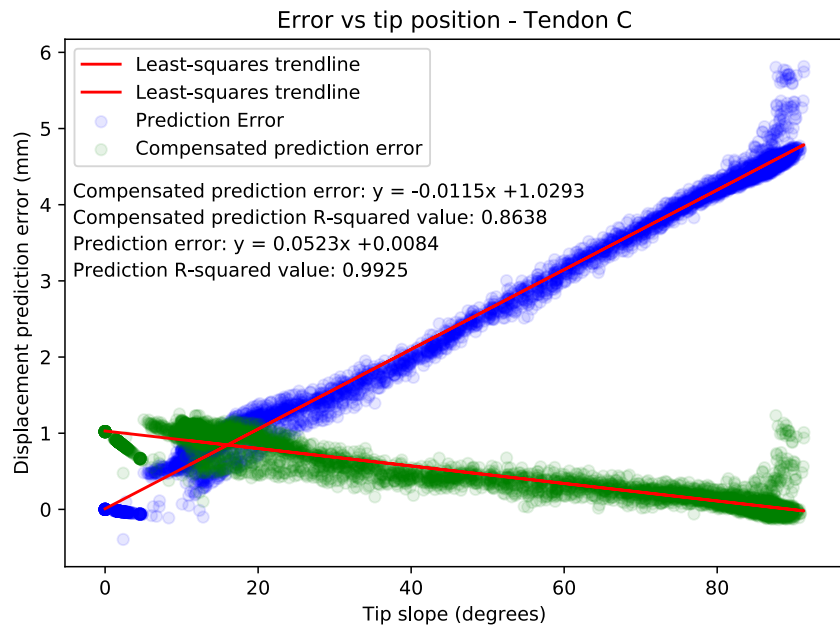


Figure 4.7: Displacement prediction error for Catheter 1, Tendon C

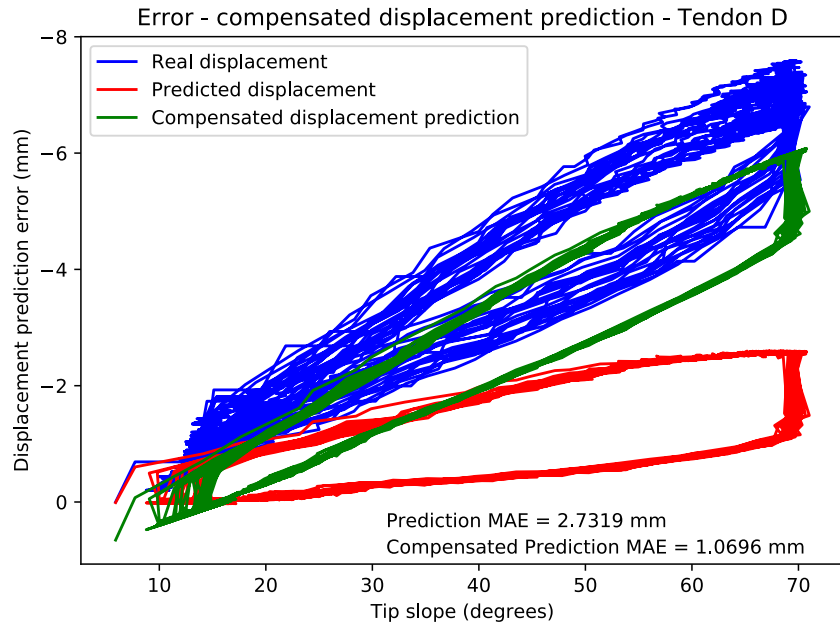


Figure 4.8: Graph of real, predicted and compensated predicted tendon displacement vs. tip deflection angle for Catheter 1, Tendon D

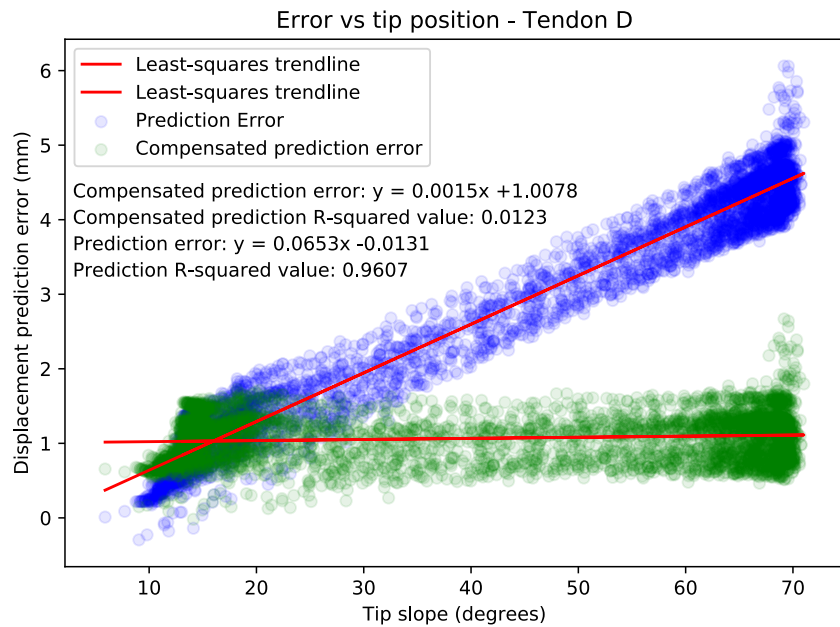


Figure 4.9: Displacement prediction error for Catheter 1, Tendon D

4.1.4 Catheter 2

Table 4.3: Catheter 2 key data

Value	Tendon A	Tendon B	Tendon C	Tendon D
Avg. displacement at 10N (mm)	-5.3835	-6.7524	-8.5320	-7.4859
Avg. displacement at 0N (mm)	-0.0634	-0.6044	-0.9337	-0.7903
Avg. tip angle at 10N (°)	64.8785	61.3217	101.6163	96.2519
Avg. tip angle at 0N(°)	18.8595	20.6164	25.7238	29.5375

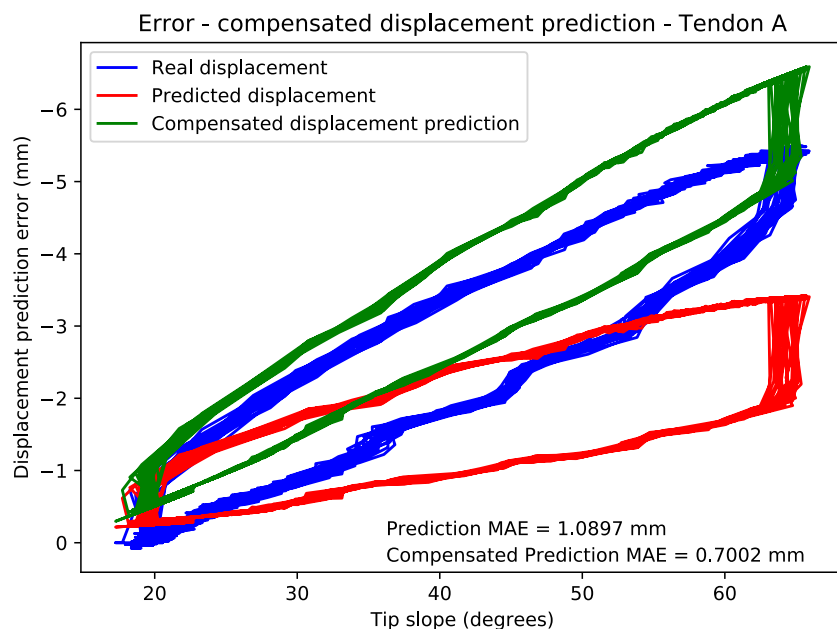


Figure 4.10: Graph of real, predicted and compensated predicted tendon displacement vs. tip deflection angle for Catheter 2, Tendon A

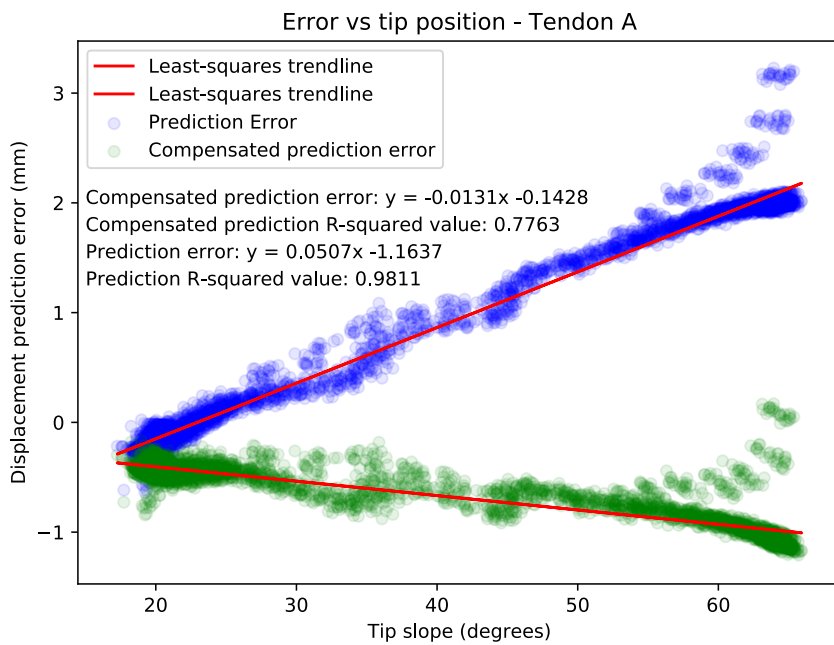


Figure 4.11: Displacement prediction error for Catheter 2, Tendon A

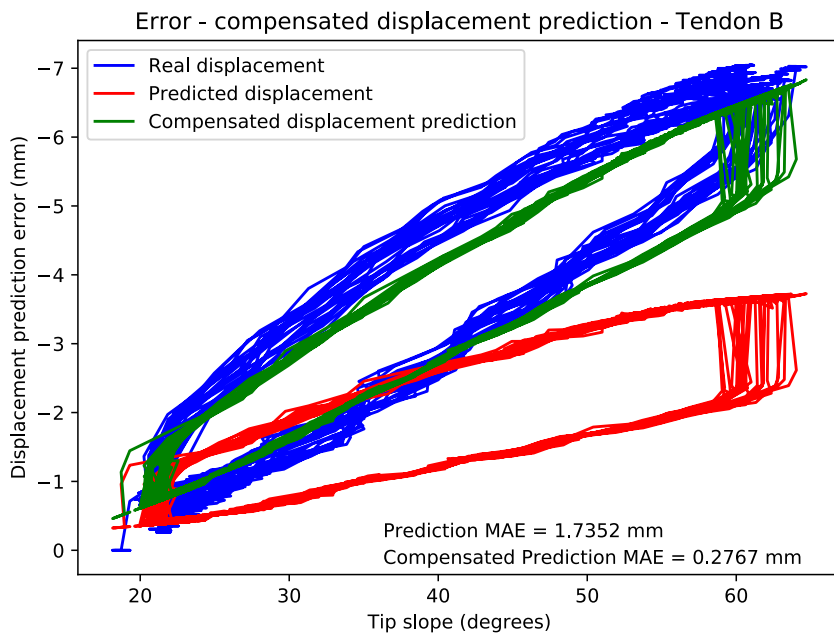


Figure 4.12: Graph of real, predicted and compensated predicted tendon displacement vs. tip deflection angle for Catheter 2, Tendon B

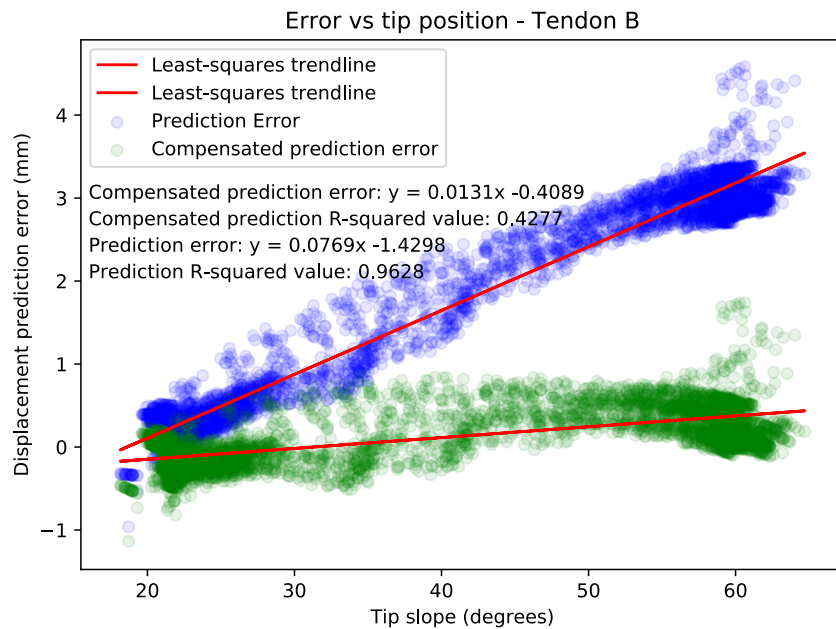


Figure 4.13: Displacement prediction error for Catheter 2, Tendon B

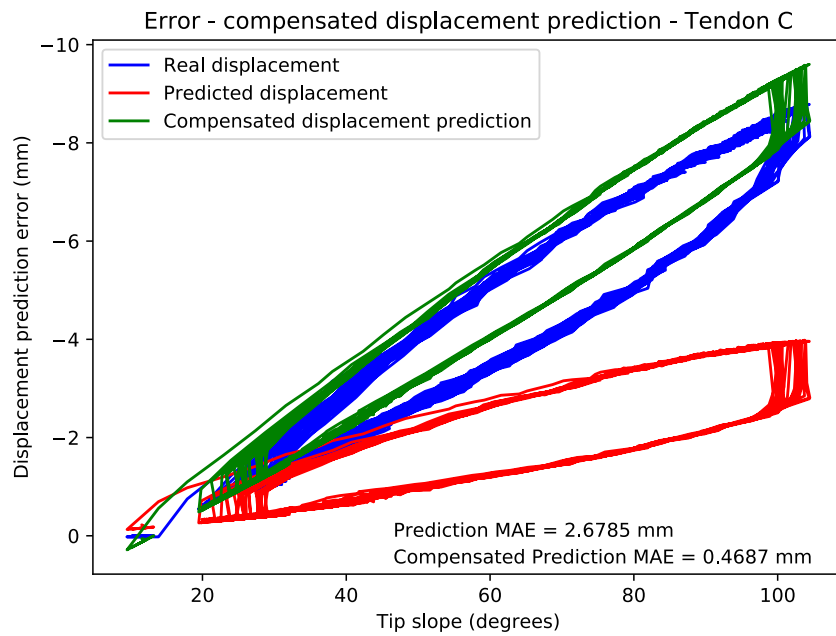


Figure 4.14: Graph of real, predicted and compensated predicted tendon displacement vs. tip deflection angle for Catheter 2, Tendon C

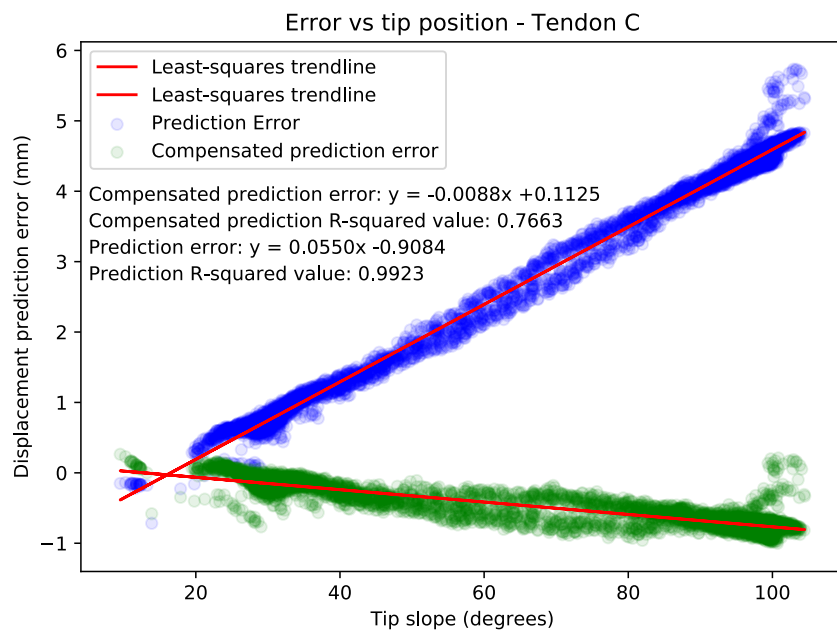


Figure 4.15: Displacement prediction error for Catheter 2, Tendon C

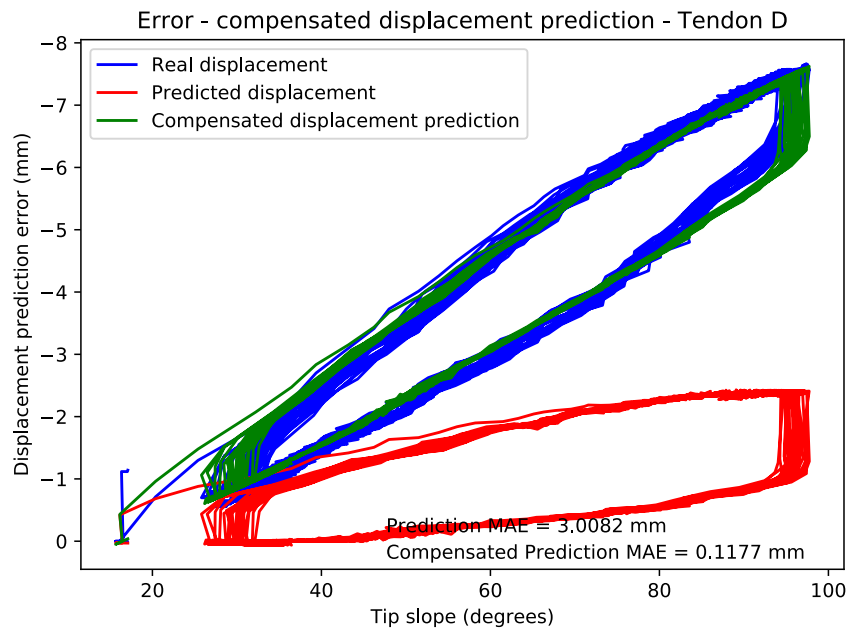


Figure 4.16: Graph of real, predicted and compensated predicted tendon displacement vs. tip deflection angle for Catheter 2, Tendon D

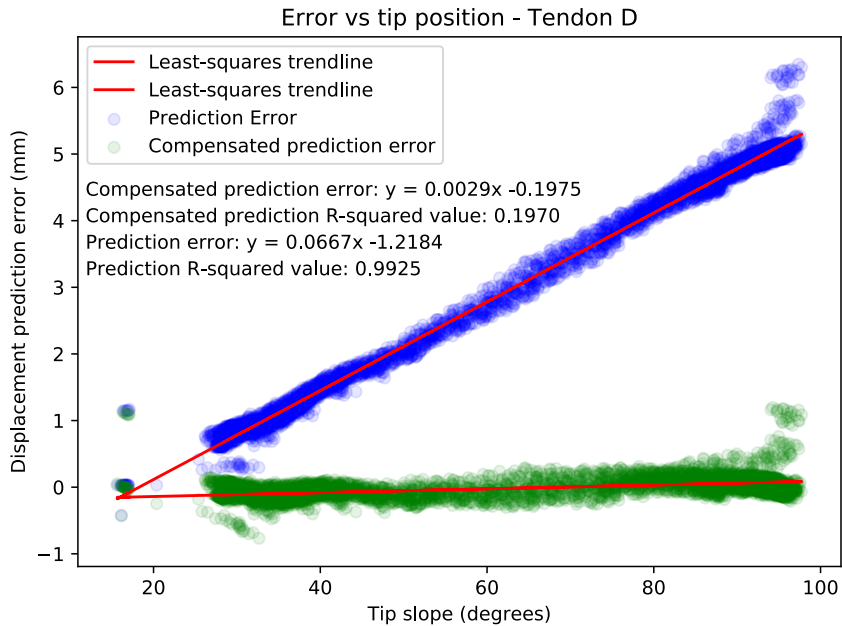


Figure 4.17: Displacement prediction error for Catheter 2, Tendon D

4.1.5 Error compensation

As the hypothesis posited in section 2.2 focuses on tendon displacement, it was decided to use the tendon force and tip angle data collected to predict the tendon displacement and then compare it to the experimental data. The primary metric for this comparison is the mean absolute error (MAE) of the prediction:

$$MAE = \frac{\sum_{i=1}^n |p_i - q_i|}{n} \quad (4.1)$$

where:

p_i Is the predicted value

q_i Is the observed value

n Is the number of prediction / observation pairs.

Collecting and compiling this information results in the data shown in Tbl. 4.4.

Table 4.4: Prediction Error data

Catheter / Tendon	Error Trendline data			
	MAE (mm)	Slope	Y-intercept	R-squared value
1A	1.6712	0.0863	-2.8467	0.9856
1B	2.8440	0.0573	-0.5956	0.9728
1C	2.5201	0.0523	0.0084	0.9925
1D	2.7319	0.0653	-0.0131	0.9607
2A	1.0290	0.0479	-1.1053	0.9768
2B	1.7352	0.0769	-1.4298	0.9628
2C	2.6785	0.0550	-0.9084	0.9923
2D	3.0082	0.0667	-1.2184	0.9925
Minimum	1.0290	0.0479	-2.8467	0.9607
Maximum	3.0082	0.0863	0.0084	0.9925
Mean	2.2773	0.0635	-1.0136	0.9795

The average MAE for the two catheters was 2.28 mm (min: 1.03 mm, max: 3.01 mm). However, this value alone does not capture the nature of the prediction error. Inspection of the the real and predicted tendon displacement vs tip deflection graphs (e.g. Fig. 4.2) shows that the shape of the prediction curve is, by and large, correct. Plotting the error over the tip deflection confirms this suspicion - the error distribution is highly linear (mean r-squared value of 0.9795), increasing in magnitude with increasing tip deflection. As this effect is present and pronounced in both of the tested catheters and in all tendons, it seems safe to assume that this error arises from the nature of our predictive model - in other words, a factor affecting the tendon displacement was overlooked.

There are a few possible error sources that would produce such a regular error - the largest of which is probably that the axial compression of the catheter shaft was not accounted for in the model. Unfortunately, the material specifications for both the catheter shaft material and the lower-durometer articulating section were not supplied by the manufacturer. Alternatively, the specific stainless steel used in the catheter tendons may have had a slightly lower elastic modulus, leading to more strain in the tendon - although this would have had an effect on the order of tenths of millimetres - not the MAE of 2.28 mm observed.

The hypothesis of axial catheter compression could easily be tested in the future - repeating the tests with the catheter fixated immediately proximal to the articulating section should eliminate any axial change in catheter length, as the reaction force is now supplied immediately adjacent to the articulating section and the shaft is not loaded. The mechanical properties of the steel tendons could be confirmed through a simple tensile test.

In the absence of mechanical property data, we can attempt to account for the observed error by adding an offset to the prediction that scales with tip deflection in the same manner as the empirical data:

$$C_t = D_t - \Delta L_t - (m\theta + c) \quad (4.2)$$

where:

C_t is the compensated tendon displacement

D_t is the kinematically predicted tendon displacement in mm

ΔL_t is the change in tendon length under load in mm

m is the slope of the linear regression line resulting from plotting error over tip deflection in mm per degree

θ is the observed magnitude of tip deflection, in degrees

c is the y-axis (error) intercept of the same regression line.

This compensation reduces mean absolute prediction error by between 26% and 96%, with a mean improvement of 72.84%, as shown in the table below:

Table 4.5: Mean Absolute Error data before and after error compensation

Catheter / Tendon	Prediction	Compensated	Difference	Percentage
	MAE (mm)	Prediction MAE (mm)	(mm)	differ- ence (%)
1A	1.6712	0.6632	-1.0080	-60.32%
1B	2.8440	0.2176	-2.6264	-92.35%
1C	2.5201	0.4895	-2.0306	-80.58%
1D	2.7319	1.0696	-1.6623	-60.85%
2A	1.0290	0.7612	-0.2678	-26.03%
2B	1.7352	0.2767	-1.4585	-84.05%
2C	2.6785	0.4687	-2.2098	-82.50%
2D	3.0082	0.1177	-2.8905	-96.09%
Minimum	1.0290	0.1177	-2.8905	-96.09%
Maximum	3.0082	1.0696	-0.2678	-26.03%
Mean	2.2773	0.5080	-1.7692	-72.84%

4.1.6 Tendon load - displacement hysteresis

Figs. 4.2 - 4.17 (as well the raw data in appendix Figs. A.1 - A.8) show significant hysteresis between the loading and unloading cycles, characterised by a lower tensile force experienced during unloading compared to loading of the tendon.

In an attempt to quantify this behaviour, the relationship between tendon load and tendon displacement was examined. In mechanical systems such as this, hysteresis is an effect of friction. Specifically in this case, the friction in the system arises from the nonlinear tendon path, the wall contact between the tendon and the tendon lumen, internal friction in the material of the articulating section, and from the tendon contacting the wall of the articulating section as it bends. All of these sources are very difficult to examine closely and model, so it was decided to simply quantify the size of the effect.

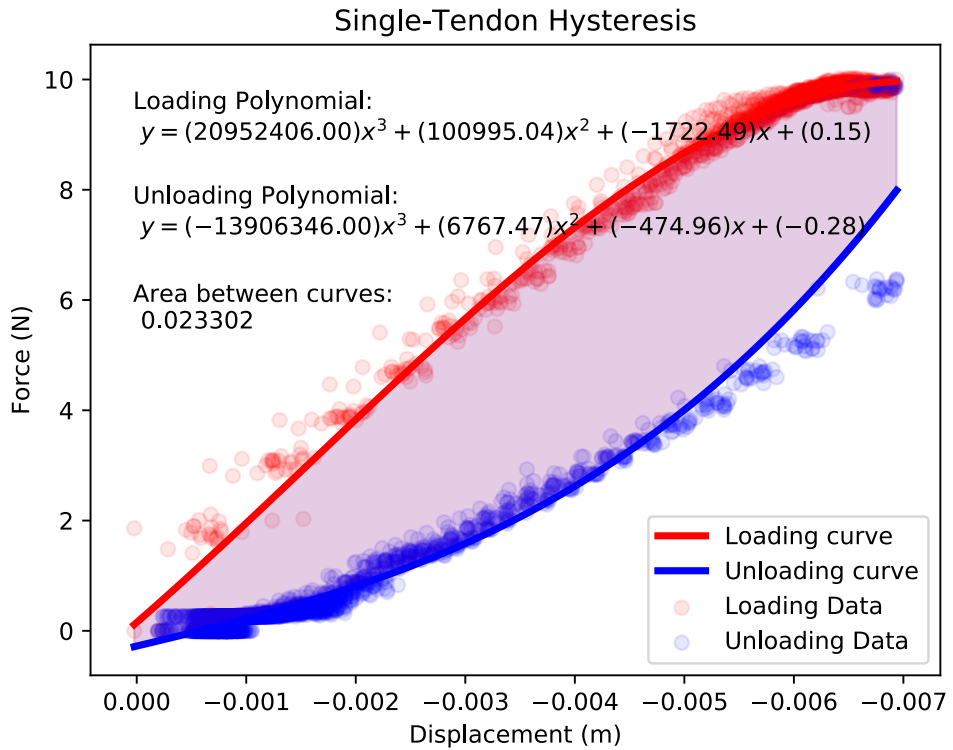


Figure 4.18: Force-Displacement graph of Catheter 1, Tendon A showing the data points, regression curves and area between loading and unloading curves

To correctly plot and calculate tendon force and displacement, the data had to be separated into distinct loading and unloading cycles. In Python, this was achieved by grouping points where the setpoint of the tendon equalled 10N, and the unloading phases were isolated by grouping the data where the setpoint equalled 0N. Next, a third-order polynomial regression was carried out on the force - tendon displacement plot to find a loading and an unloading curve, and integrating each curve to find the area below it. Subtracting these areas from each other yields the area of the graph between the loading and unloading curves. Using this method, the energy loss due to friction in the catheter actuation system was between 0.0166 J and 0.0293 J, with a mean energy loss of 0.0237 J.

Table 4.6: Area of hysteresis curves

Catheter / Tendon	Hysteresis area (J)
1A	0.0233
1B	0.0283
1C	0.0279
1D	0.0236
2A	0.0166
2B	0.0204
2C	0.0293
2D	0.0204
Min	0.0166
Max	0.0293
Mean	0.0237

4.1.7 Tip angle - loading relationship

Kinetostatic analysis, i.e. the determination of the forces acting upon the elements in a mechanism, generally follows the kinematic modelling of a system. The kinematic model proposed in chapter 2 therefore represents just the first step in fully modelling the catheter. While a theoretical kinetostatic analysis was not performed due to time constraints, the data gathered as part of the experimentation described in chapter 4 can be used as a starting point for a future kinetostatic analysis relating tip pose to tendon load. With this in mind, the load applied to a given tendon, F_T , was plotted over θ , the magnitude of tip deflection.

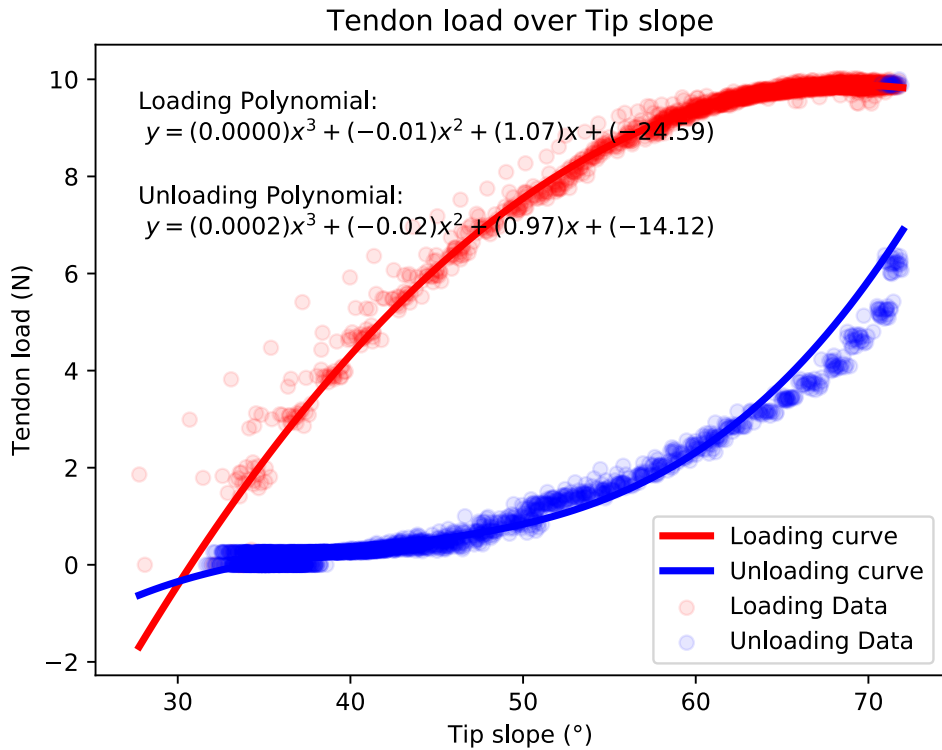


Figure 4.19: A plot of tendon load over tip angle for catheter 1, tendon A. Note the distinct loading and unloading curves.

As with the hysteresis plots in section 4.1.6, the data for each tendon was split into loading and unloading sections, and 3rd-order polynomial regressions were carried out to find the curve of best fit for each loading / unloading curve, respectively. The polynomials express the relationship between tendon force and catheter tip angle in the form:

$$F_T = a\theta^3 + b\theta^2 + c\theta + d \quad (4.3)$$

Where:

F_T is the load on a given tendon;

θ is the currently-observed tip angle;

a, b, c are the polynomial coefficients, and

d is the x-axis intercept of the polynomial.

Table 4.7: Polynomial regression coefficients for tendon loading curves. Matching tendons in separate catheters are grouped to facilitate easy comparison.

Tendon	<i>a</i>	<i>b</i>	<i>c</i>	<i>d</i>
1A	0.0000	-0.01	1.07	-24.59
2A	0.0000	-0.01	0.68	-8.96
1B	0.0000	0.00	0.21	-4.43
2B	0.0000	-0.01	0.69	-9.69
1C	0.0000	0.00	0.17	-0.48
2C	0.0000	0.00	0.26	-3.98
1D	0.0000	0.00	0.22	-1.40
2D	0.0000	0.00	0.29	-5.58

Table 4.8: Polynomial regression coefficients for tendon unloading curves. Matching tendons in separate catheters are grouped to facilitate easy comparison.

Tendon	<i>a</i>	<i>b</i>	<i>c</i>	<i>d</i>
1A	0.0002	-0.02	0.97	-14.12
2A	0.0001	-0.01	0.47	-5.43
1B	0.0001	-0.01	0.37	-5.80
2B	0.0001	-0.01	0.33	-4.40
1C	0.0000	0.00	0.12	-1.05
2C	0.0000	0.00	0.17	-2.79
1D	0.0001	0.00	0.19	-1.80
2D	0.0000	0.00	0.23	-3.99

A cursory examination of Tbls. 4.7 and 4.8 shows that the regression data is not very consistent from catheter to catheter; in part this is due to the limited amount of catheters available, but a large part is also played by the comparatively slow sampling rate of the load cells. Examining Fig. 4.19 reveals a sparsity of data points immediately following the transition from loading to unloading; this is due to a fast change in load that the sample rate simply could not keep up with. Future experiments using this apparatus should either limit the speed of the motors, or attempt to increase the sample rate of the arduino controlling the load cells - although this approach previously caused serial communication issues.

4.1.8 Experiment variability

Despite every tendon and catheter having been tested on the same load cell and linear axis, there was still a visible amount of variation from tendon to tendon. Specifically Catheter 1, Tendon D (Fig. 4.8) and Catheter 2, Tendon B (Fig. 4.12) show a vertical offset, or drift, from one loading / unloading cycle to the next. At first glance, this behaviour could be explained by fatigue causing a change in the mechanical properties of the catheter tip over time, but the absence of this drift in the other tendons' data suggests otherwise. It seems most likely that the tendon slipped slightly in the clamp between iterations. The slippage wasn't immediately obvious during the experiment, as the total movement of the tendon in the clamp over the course of the experiment was between 1 and 2 mm. During the loading cycle, the linear axis moves back to apply tension until the loading setpoint is reached. The load is then maintained for several seconds. If any tendon slip occurs in this phase, the axis will attempt to compensate, causing it to move further than it should. Upon unloading, the axis will reach the 0N point at a different position than in the previous cycle, causing the next cycle to start from this offset position. The resultant effect would be a slow upward drift on the graph as visible in Figs. 4.8 and 4.12.

4.1.9 Mechanical constraints

To actuate the tip of the catheter a force needs to be applied to a tendon - this also means that a reaction force is needed to keep the system static. In this case the reaction force is provided by the catheter clamp (shown in Fig. 4.1). The clamp uses a screw to apply a radially compressive force on the catheter shaft. The resulting friction between the clamp and catheter shaft locks the proximal end of the catheter in place. Although the clamp was designed to match the shaft as closely as possible in diameter, it is unavoidable that the compression causes some local deformation of the catheter's cross-section. It is possible that this deformation causes a narrowing of the tendon lumen. If such a narrowing occurs, the result would be increased friction between the tendon and lumen, in turn causing higher tendon loads for the same tip deflection. To mitigate this effect, each catheter was placed in the clamp and the screw gradually tightened until it could no longer be pulled out of the clamp by hand. While this was a highly subjective approach, it avoided serious overtightening.

Further mitigation of this effect could be achieved by modifying the apparatus to use a machinist's collet instead of a simple clamp; these collets are designed to evenly distribute compressive force onto a cylindrical surface, thus maximising the contact area between the catheter and fixture and allowing lower forces to be used.

Evenly distributing compression additionally helps avoid uneven shaft deformation. Subjectivity of clamping forces could also be eliminated by using a torque wrench to tighten the collet holder, thereby ensuring that the same clamping forces are used every time.

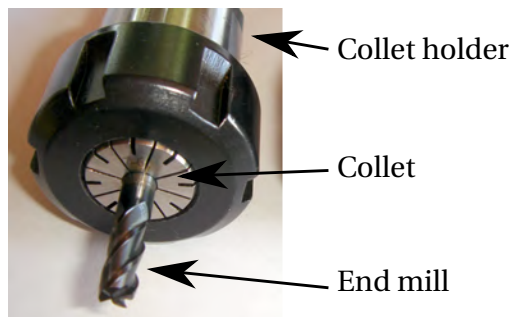


Figure 4.20: Standard ER collet with end mill showing the distribution of clamping points on the cylindrical face of an end mill. Image courtesy of CTC Engineering Ltd, Hong Kong

During these experiments the catheter was left largely unconstrained along its length and was supported by a series of 3D printed holders spaced approximately 20cm apart. The holders were kept aligned by an 8mm steel rod attached to the catheter clamp. This kept the catheter shaft straight and horizontal along its length.

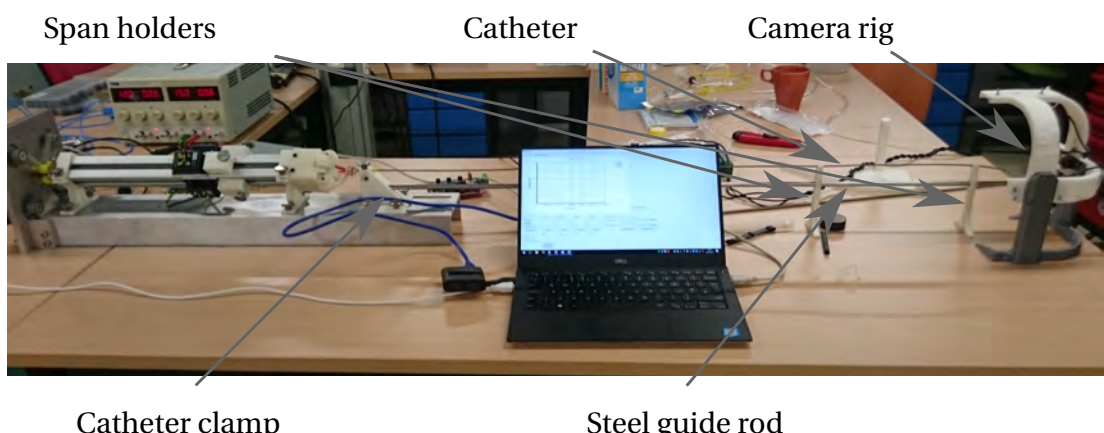


Figure 4.21: Overview of the Testing assembly showing the catheter clamp, guide rod and catheter supports

Some buckling was observed along the catheter shaft during testing, the effect of which is explained in section 4.1.10. Future experiments should be conducted with the catheter constrained inside a rigid tube to avoid this effect.

4.1.10 Limitations

This model is of limited use in real life applications. It assumes that the catheter is straight along its shaft, which is rarely the case. If the shape of the catheter shaft is not known, the relationship between tendon displacement, tip deflection and tendon force breaks down. From an analytical perspective, it becomes almost as if the catheter has one or more articulating sections along the length of its shaft, each with its own magnitude and direction of deflection. This will cause various amounts of tendon displacement before the tip is ever intentionally deflected by actuating the tendons. Furthermore, to make the model correction truly valid, one would have to gather far more data in order to make a statistically valid assumption about the behaviour of the catheter.

4.2 Multi-tendon loading

4.2.1 Methods

The catheter was prepared in much the same way as for the single-tendon experiments - the catheter was clamped into the testing rig on the proximal end (see Fig. 4.1), and the tendons connected to each of the tendon clamps. Instead of using the same computer vision-based tip angle measurement, it was decided to use the Anser electromagnetic tracking system. The catheter to be tested was equipped with two NDI 610099 5-DOF sensors, as described in section 3.3.2. The tendons were then sequentially loaded and unloaded by an AutoHotkey script.

This script first loaded all tendons simultaneously to 1N for a duration of 10s to remove any slack in the tendons, followed by a simultaneous release to 0N. After five seconds, the test itself began. For 360 iterations (one iteration for each degree of α) the script calculated how much of a peak force of 7N to distribute on to each tendon as a function of the target (α) value. It did this by simply calculating the component of the 7N acting in the direction of a given tendon. For example, with a target force of 7N and $\alpha = 70^\circ$:

$$F_A = 7 \cdot \cos(70) = 2.394N \quad (4.4)$$

$$F_B = 7 \cdot \cos(105.73 - 70) = 5.682N \quad (4.5)$$

$$F_C = -1 \cdot 7 \cdot \sin(70) = -0.342N \quad (4.6)$$

$$F_D = 7 \cdot \cos(254.27 - 70) = -6.981N \quad (4.7)$$

However, negative values are discarded since a tendon cannot transmit axially compressive forces, leaving us with $F_A = 2.394N$ and $F_B = 5.682N$.

4.2.2 Multi-tendon results

Fig. 4.22 shows the testing rig tracking the distribution of forces across the tendons of the catheter, with the total tensile force on the catheter in yellow. Fig. 4.23 shows the total displacement of the tendons during the test run. Fig. 4.24 shows the magnitude of tip deflection during the run, and Fig. 4.25 shows the direction of tip deflection during the run. Finally, Fig. 4.26 shows the movement of the distal tip with magnitude and direction of deflection.

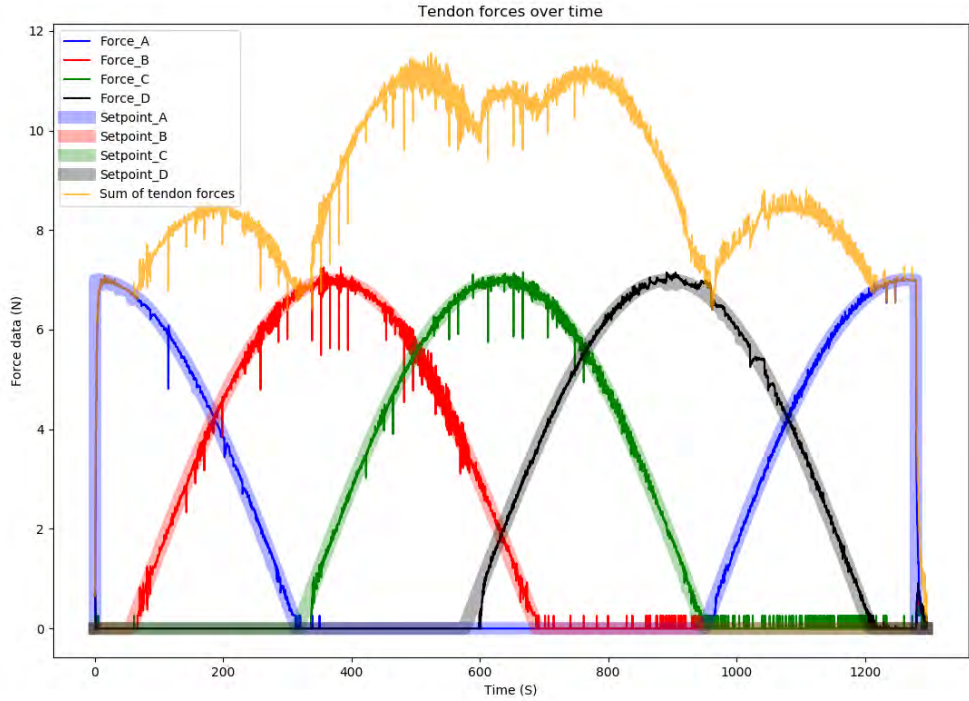


Figure 4.22: Tendon forces over time

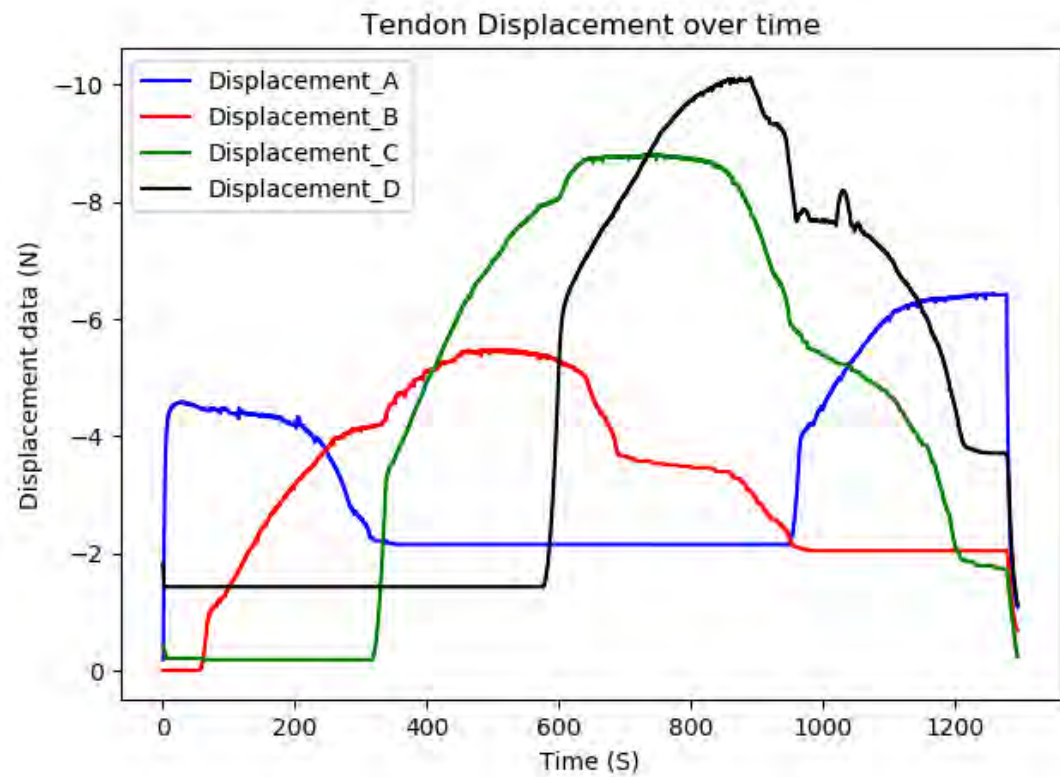


Figure 4.23: Tendon displacement over time

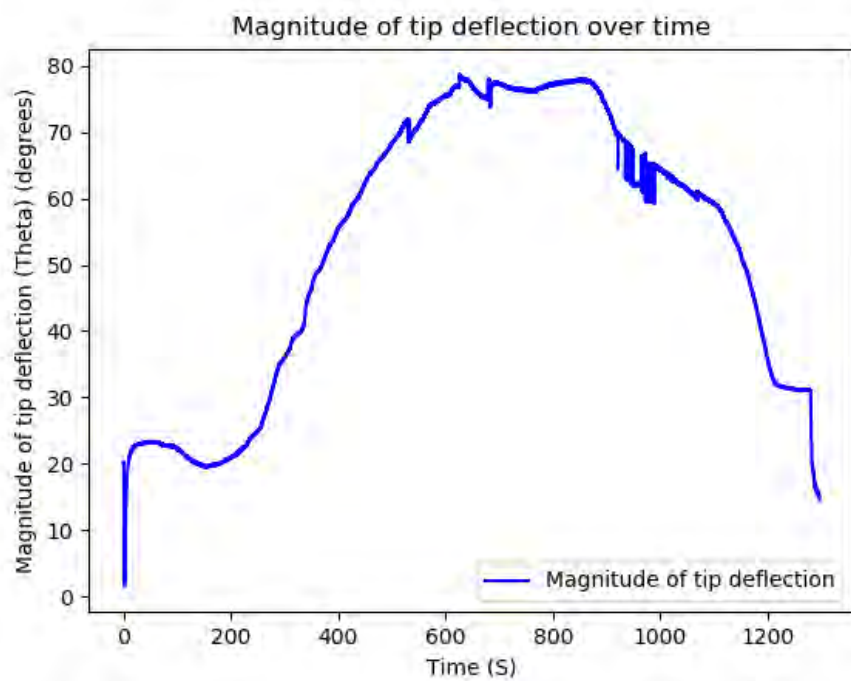


Figure 4.24: Tip Deflection over time

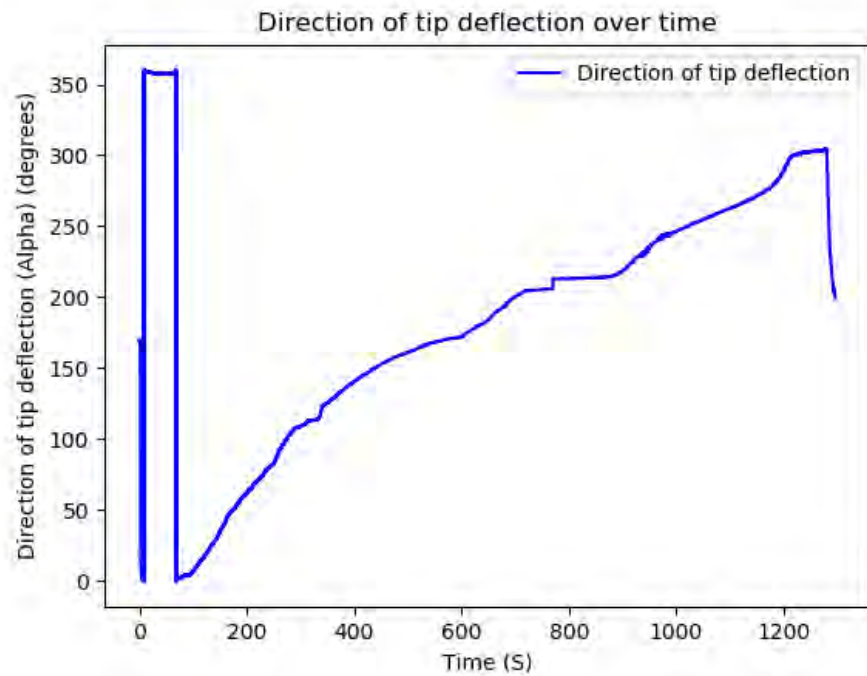


Figure 4.25: Direction of tip deflection over time

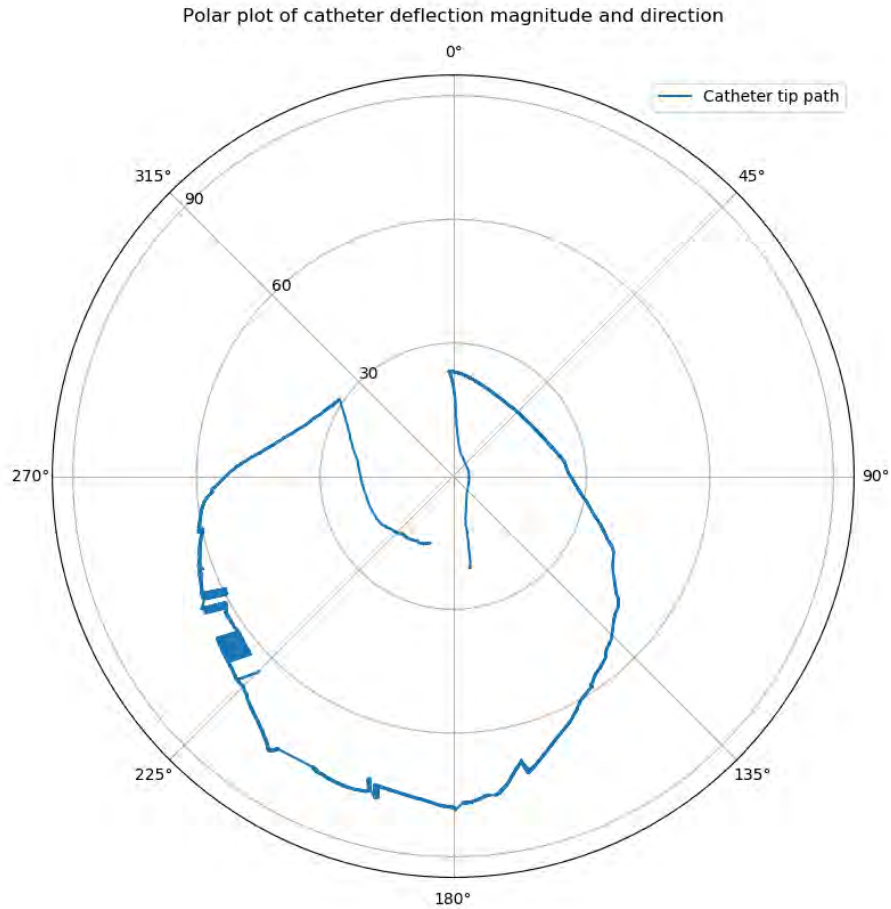


Figure 4.26: Polar plot showing the movement of the distal tip during multi-tendon testing - the radial axis shows the magnitude of deflection θ , while the directional axis shows the direction of tip deflection α

4.2.3 Multi-tendon test observations

The multi-tendon data highlights some interesting features of the catheter that were difficult to observe in the single-tendon data. The most obvious of these may be the fact that the tip of the catheter is not perfectly straight in its relaxed state. Fig. 4.26 shows that the catheter starts with about $\theta = 20^\circ$ at $\alpha = 170^\circ$. This pre-existing bend was also observed in the other catheters, but its source remains unclear - it could be a manufacturing defect, a result of transporting and storing the catheters upright on their tips or a result of repeated bending in a given direction.

There is a possibility that the yellow shrink wrap used to attached the EM tracking sensor to the catheter (see Fig. 3.13) constrained the movement of the articulating

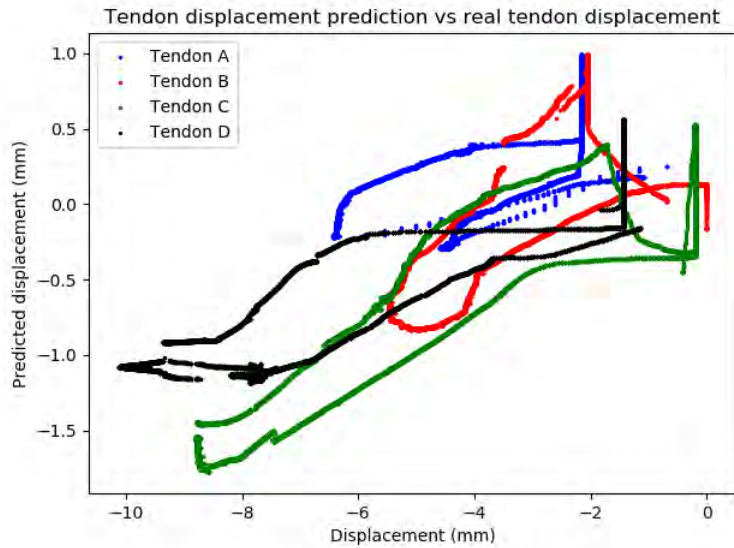


Figure 4.27: A plot of the data showing the correlation between the predicted and real displacements

section. While this is a concern, care was taken to position the heat shrink tubing on the rigid shaft proximal and distal to the articulating section to minimise any potential mechanical interference. It seems more likely that the weight of the sensor cable, while small, could have pulled the tip of catheter downward, presenting a potential explanation for the downward skew seen in Fig. 4.26. Future testing should be carried out with better cable management to ensure that sensor cabling does not interfere with tip deflection.

It is also easily visible from Fig 4.26 that the magnitude of tip deflection varies quite significantly - from just over $\theta = 25^\circ$ at $\alpha = 0^\circ$ to $\theta = 75^\circ$ at $\alpha = 180^\circ$. While it is possible that the pre-existing bend in the catheter tip could be partially responsible for this behaviour, it is far more likely to be a result of the manner in which the catheter was loaded. Fig. 4.22 shows that the sum of applied forces is far higher around $\alpha = 180^\circ$, leading to a higher value of θ .

The model of tendon displacement begins to break down when steering the catheter with more than one tendon at a time. While the prediction does show positive correlation with the empirical data, the errors are far less predictable than under single-tendon loading (see Fig. 4.27), and the data correlation is again highly dependent on the previous state of the system, i.e. there is some degree of hysteresis between the loading and unloading states.

Mean absolute error was also high, as indicated in Tbl. 4.9 - This becomes very clear when looking at Fig. 4.28.

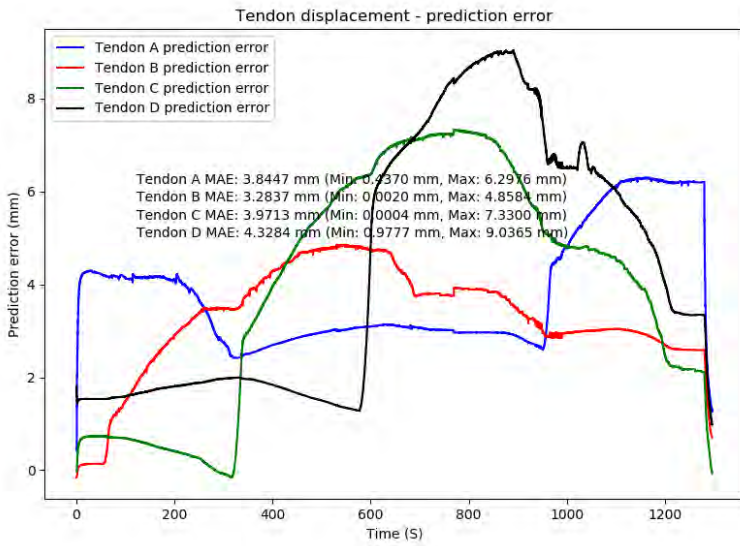


Figure 4.28: Tendon displacement prediction error over time

Table 4.9: Tendon displacement prediction errors

Tendon	Minimum error (mm)	Maximum error (mm)	MAE (mm)
A	0.4370	6.2976	3.8447
B	0.0020	4.8584	3.2837
C	0.0004	7.3300	3.9713
D	0.9777	9.0365	4.3284

In an effort to identify potential error sources, the error was plotted against the direction of tip deflection α , the magnitude of tip deflection θ , the forces on each individual tendon, and the sum of the forces on all tendons.

There is a firm positive correlation between error and tendon force (see Fig. 4.29), and there are clear loading / unloading loops present for each individual tendon. It appears as if the prediction errors are closely tied to the individual tendon forces, and that shortening of the catheter due to axial loading is only a minor contributor to the total prediction error.

One potential explanation for this behaviour could be unwanted deflection of the catheter further up the shaft. Examining the raw electromagnetic tracking data shows that sensor A (proximal to the articulating section) moved during testing (see Fig. 4.30), shadowing the distal tip's movement in a smaller circle.

It is difficult to say exactly how much this affects the data - the shaft of the catheter was not tracked during the experiment and therefore there is no way to determine the size of the effect. We expect that it would increase the observed tendon displacement

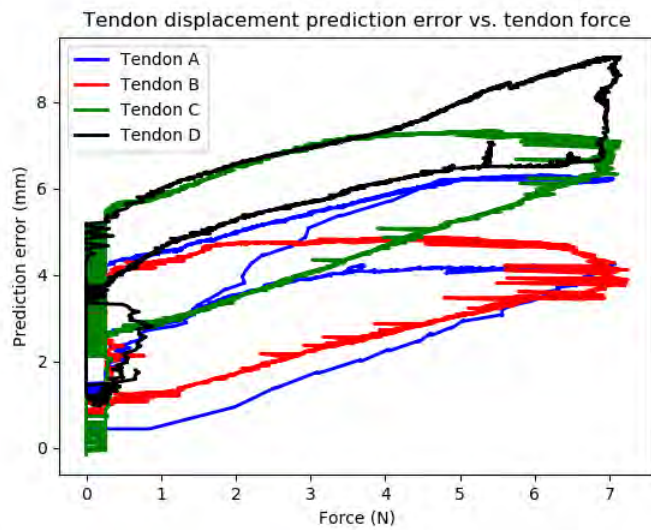


Figure 4.29: A plot of prediction error over tendon force.

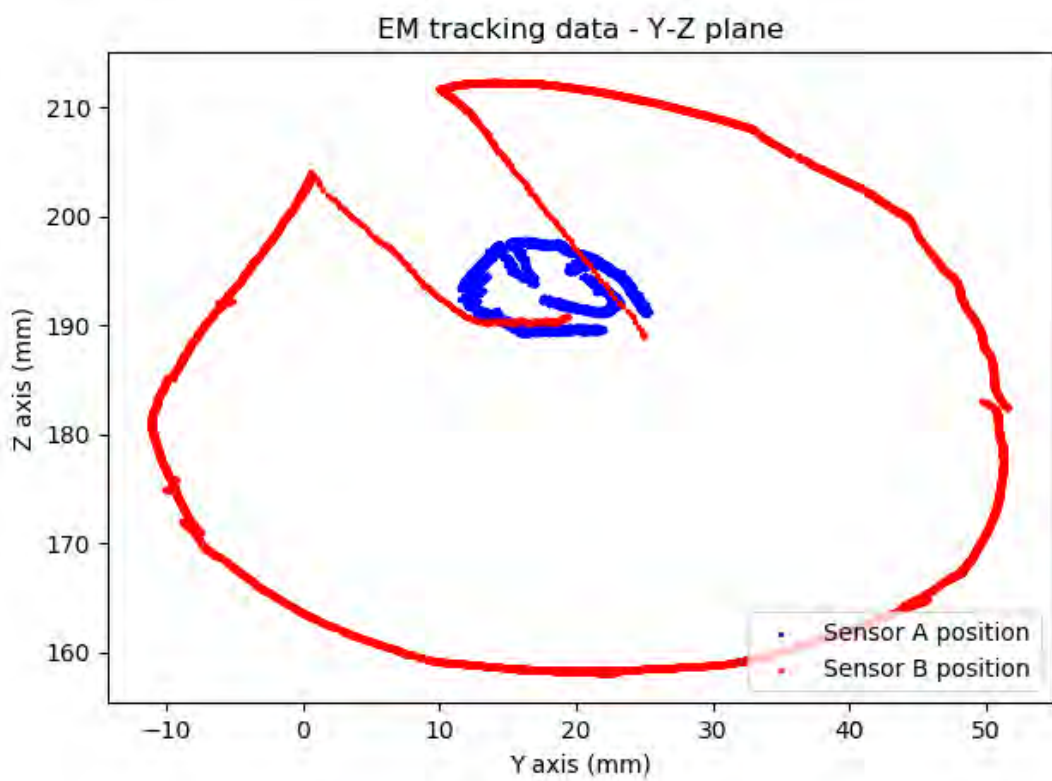


Figure 4.30: Axial view of the tracking data showing the movement of sensors A and B.

for a given applied tension while remaining difficult to identify in the tip tracking data because θ is simply calculated by taking the dot product of \vec{A} and \vec{B} .

In practice, this effect was also observed when trying to use steering handles - if unconstrained, the catheters always deflected significantly along their entire length instead of just at the articulating section, in some cases as much as 30° - 45° . This is a side effect of the construction of the catheter - its shaft is constructed from a monolithic piece of polymer extrusion with no reinforcements or braiding, meaning that the difference in rigidity between the articulating section and the rigid shaft was relatively low. By comparison, the SuperDimension iLogic catheter has a shaft consisting of coiled stainless steel, providing a far more rigid structure.

There is little that can be done about this without totally changing the design of the catheter to a braid-reinforced design. Fortunately, in a real-life scenario the catheter is constrained by the walls of the endoscope working channel, mitigating this effect somewhat.

Chapter 5

Catheter handle design

The starting point for the catheter handle design was a third-party conceptual design proposed by The Design Factor, Belfast, after consulting with the UCC Biodesign group. A plunger and barrel cam actuation mechanism was suggested to the The Design Factor, who created the concept around this mechanism.

5.1 Preliminary catheter handle design

The suggested actuation mechanism consisted of a barrel cam with a sinusoidal profile integrated into a plunger-style handle similar to the SuperDimension iLogic (See Fig. 1.8). The followers were intended to sit in the barrel cam at the 0°, 105.73°, 180°, and 254.27° positions, giving them a similar displacement profile and offset as seen in Fig. 2.10. While the superDimension can only actuate one tendon at a time, the intention of the barrel cam was to provide infinitely-adjustable direction and magnitude of deflection. The resulting designs are picture in Figs. 5.1 - 5.4. While this design formed an input to the following prototype iterations, the final design differed significantly in form and design. In the implementations that followed, 3D printed PLA was used where possible, while other materials were sourced from in-house stock.

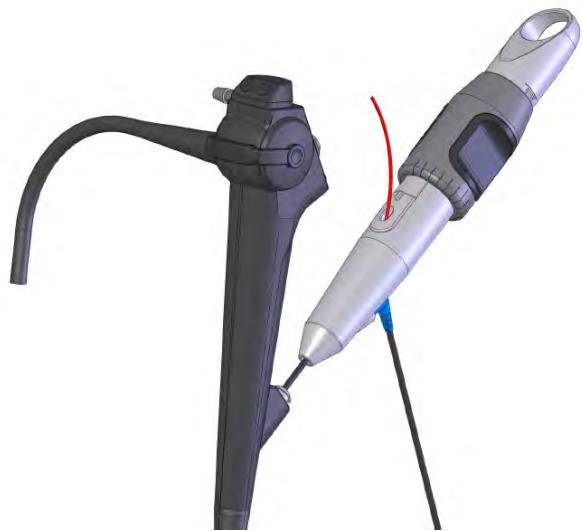


Figure 5.1: Concept 1 designed by The Design Factor. (Rendering courtesy of The Design Factor)



Figure 5.2: Concept 2 designed by The Design Factor. This version features a straight handle with a clip to attach the handle to the bronchoscope. (Rendering courtesy of The Design Factor)



Figure 5.3: Concept 3 designed by The Design Factor. To facilitate easier insertion of tools into the working lumen, the handle is angled. (Rendering courtesy of The Design Factor)



Figure 5.4: Concept 4 designed by The Design Factor. This version is both angled and features a scope attachment clip. (Rendering courtesy of The Design Factor)

5.2 Catheter handle design A

Catheter design A emerged as a fairly natural side-effect of analysing the kinematics of the articulating section, but was designed fairly early on in the project. The key concept that emerged from the model was that while tendon displacement will cause deflection of the articulating section, the same is true in reverse - deflecting the section by hand will cause the tendons to displace. With this in mind, Design A consists of a piece of 15 mm flexible PVC tubing. The catheter is attached axially to the end of the PVC tube. Each tendon is guided through the 3D printed joint piece and runs parallel to the PVC tubing through a series of disc-shaped spacers. These spacers hold the tendons at a constant distance from the tubing while still allowing the tubing to bend, as pictured in Fig. 5.5

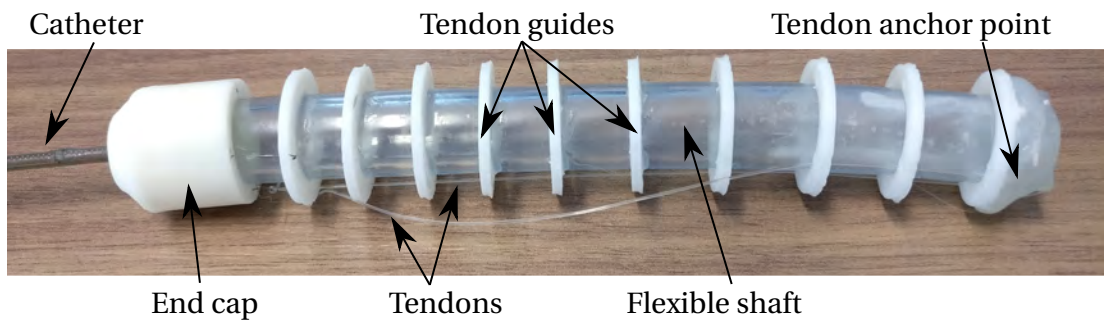


Figure 5.5: Handle Design A : bending handle

The tendons themselves pass through the spacers 9 mm from the longitudinal axis of the tubing. If the tubing is bent, the displacement of the tendon is described by Eqn. 2.4. For this particular size, tendon displacements of up to 14.1 mm could be achieved - more than enough to fulfil the theoretical requirements of the raw, uncompensated catheter model.

Theoretical tendon displacement at $r = 9$ mm vs. magnitude of handle deflection

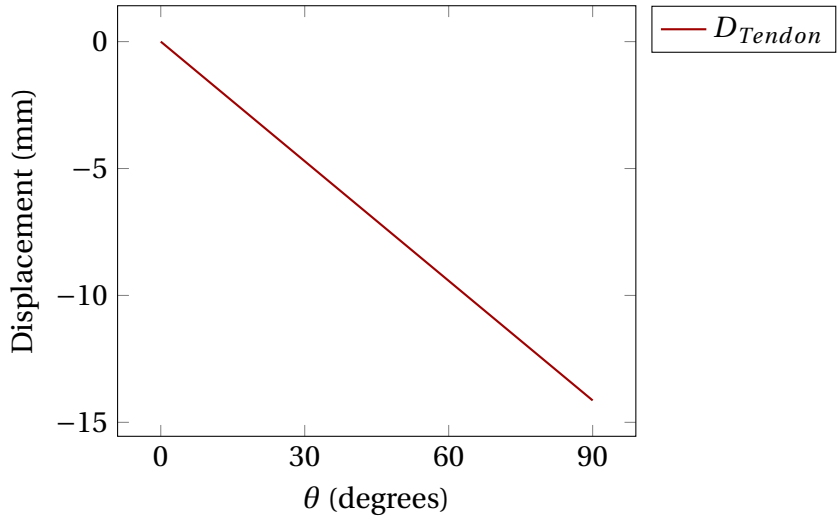


Figure 5.6: A plot of theoretical tendon displacement over handle deflection

5.2.1 Design A observations

Design A was an interesting idea that appeared relatively early on in the project, before the catheters designed for this project were delivered. For this reason, it was only prototyped roughly with one of the previous catheter designs referred to in Section 2.1, the dimensions of which were measured by hand when building this handle prototype. As a result there was a slight mismatch between the tendon positions on the handle and the tendon positions of the catheter itself, which lead to an increased amount of friction in the handle assembly. An intrinsic drawback of this handle is that it will always deflect the tip in the opposite direction to the one in which it is bent. That is to say, if the handle is bent to $\alpha = 0^\circ$, the tip will deflect toward $\alpha = 180^\circ$. To make it deflect in the same direction, the tendons would have to be crossed over inside the handle.

The design was ultimately scrapped after receiving user feedback, mostly due to ergonomic concerns. Handling an endoscope requires a minimum of one hand for the scope and one hand for the tool. Bending the body of the handle was just too awkward a motion to be performed in such a situation. Nevertheless, the handle was able to deflect the tip of the catheter in a reasonably controlled manner, and therefore functioned on a rudimentary level.

5.3 Catheter handle design B

Both the preliminary handle design as well as design B were based on a barrel cam actuation mechanism. A barrel cam is a linkage which converts rotary motion into linear motion, usually by way of an inclined plane cut into one of the axial surfaces of a cylinder. In typical applications, the motion of the barrel is constrained to rotation, while the followers riding on the cam profile are rotationally constrained, but free to move in the axial direction. If we modify this concept by permitting axial motion of the barrel cam, we can modulate the magnitude of displacement of the cam followers.

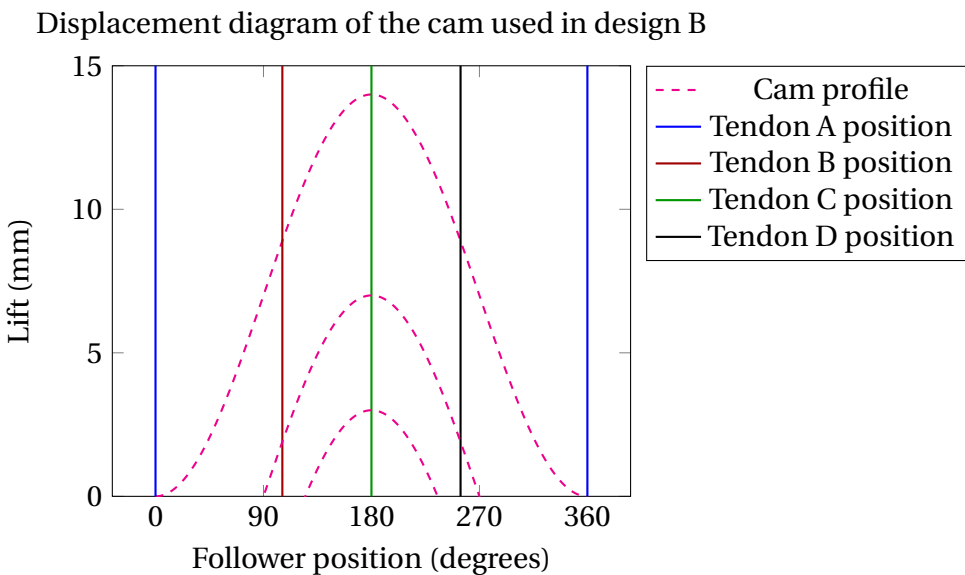


Figure 5.7: Displacement diagram of the cam ring.

The vertical lines on the displacement diagram show the positions of the cam followers. As the cam profile (dotted magenta line) moves upward, the followers are engaged more and more. The direction of deflection is then selected by rotating the cam, which shifts the sinusoid left or right.

At this point it was decided to explore the design in Fig. 5.4 further. A basic handle shell was designed, and as neither the catheters nor a bronchoscope were available at this point in the project, it was designed to fit on a Karl Storz gastroscope (model 13821 PKS, Karl Storz GmbH, Tuttlingen, Germany) that was readily available. This design was considerably smaller than the original concept provided by The Design Factor, but also featured the angled handle / catheter joint and a fixed scope clip.



Figure 5.8: Very early design exploration

End-user feedback was sought and indicated that, from an ergonomic standpoint a fixed scope clip was a bad choice as it forces the user's wrist into an unnatural and uncomfortable position, one from which it would be very difficult to exert the force necessary to actuate the tendons. The next step was to improve the scope attachment - which was done by omitting the fixed clip and replacing it with a groove in the handle body, which permitted a separate clip to be mounted without slipping, pictured in Fig. 5.9.

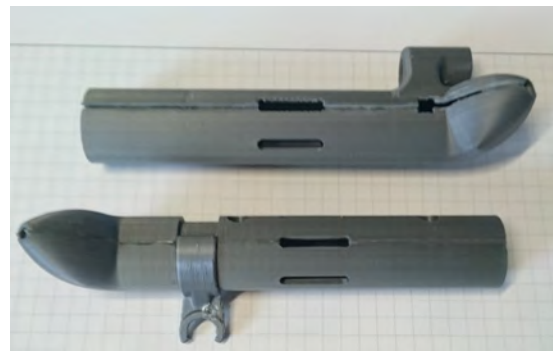


Figure 5.9: Scope attachment improvements

Choosing to move forward with this design, the cam ring was refined into a part

that could sit cleanly on the body of the handle and still be easily held like a biopsy forceps between index and middle fingers:

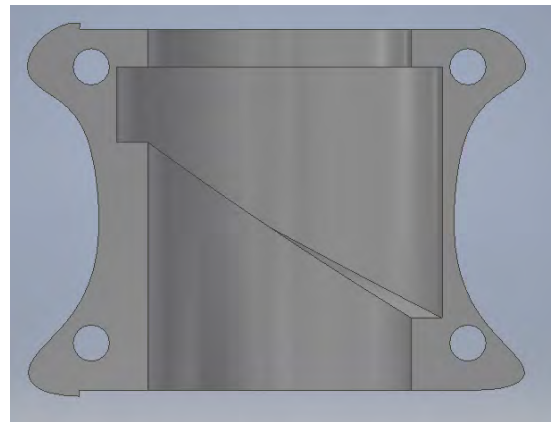


Figure 5.10: Cross-section of the cam ring showing the diagonal cam profile and the rounded outer surface.

Next, the internal mechanism was laid out. The mechanism consists of four followers, each of which is mounted to the end of one tendon. The followers are free to move axially through the handle on a steel guide rail running through the center of the handle body. Each follower has a radial lug which is allowed to protrude outside the handle body through a slot. This lug engages with the cam surface of the cam ring (Fig. 5.10).



Figure 5.11: CAD image of the the catheter handle showing the cam ring (grey), followers (beige), return springs, and scope clip (blue) inside the handle (transparent grey).

Inside the handle, the tendons are connected with the followers via four bowden tubes. These tubes guide the tendons from the catheter mounting point at the front

of the handle body, through the angled section, and into four pass-through holes on a bulkhead inside the handle body.

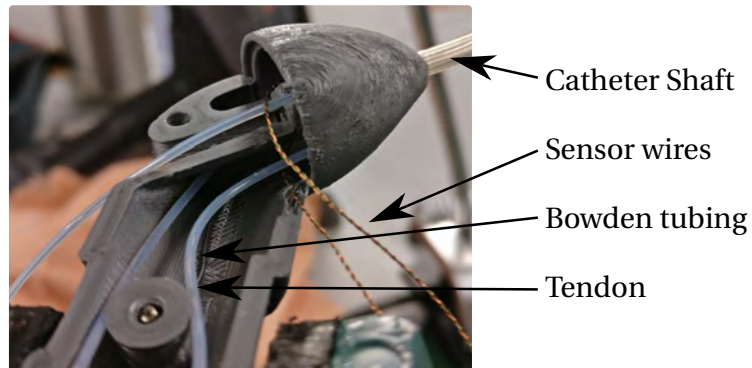


Figure 5.12: Photograph of the internals of the catheter handle showing the tendons, two sensor cables, and PTFE bowden tubes.

At first, PTFE tubing was used as the sleeving for the bowden mechanism, but it soon turned out that the axial compressibility of the PTFE tubing was far too high. Actuating the catheter handle resulted in very little tip deflection as all of the tendon displacement was simply compressing the tubing inside the handle. To remedy this, the PTFE tubing was replaced with coiled stainless steel tubing. Return springs were added to let the cam ring center itself automatically, improving the feel of the mechanism.

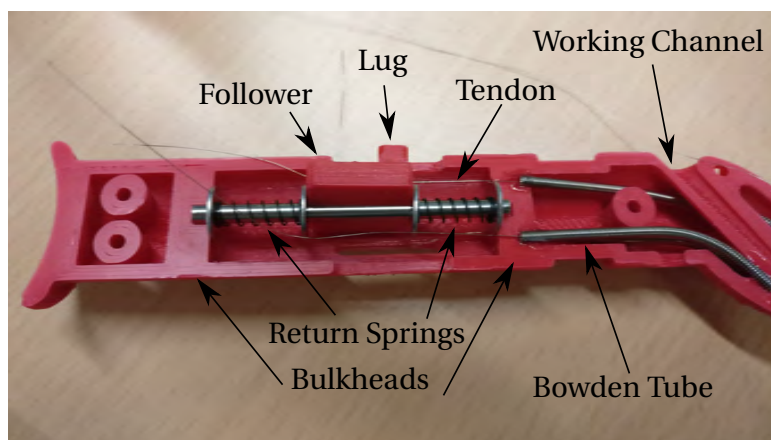


Figure 5.13: Annotated photograph of handle internals

These iterations resulted in the first usable handle prototype, shown in Fig. 5.14



Figure 5.14: Render of the final design iteration of handle design B.

5.3.1 Design B observations

This design proved moderately successful. The barrel cam mechanism performed adequately when attempting to steer the catheter, but only if the catheter was being held straight - if the shaft of the catheter was curved, the curve changed the resting position of the cam followers, shifting them backward or forward and interfering with the barrel cam's operation. From an ergonomic standpoint however, the handle worked very well - it was comfortable to hold with one hand, and gave very easy access to the working channel thanks to the angled tip. During in-vivo testing with clinical experts using this design it became clear that a scope clip was not a necessary design feature - regardless of design, the endoscopist required an assistant to operate the tool in the working channel. In fact, even the need for tip deflection in multiple planes and up to 90°came into question. Observing the clinician at work with the catheter showed that he simply used scope rotation to select a plane of deflection,

and then using very slight tip deflection of less than 30° , was able to successfully navigate the catheter into the peripheral airways.

5.4 Catheter handle design C

Building on the experience of design B, design C forgoes the view of the catheter as one cohesive unit, and gives each tendon its own independent actuation element in order to avoid the loss of control associated with the catheter shaft being in a curved state. It also increases the maximum tendon displacement achievable by each actuation element by a significant margin. This design is also mechanically completely distinct from designs A or B, using a simpler rack-and-pinion mechanism to actuate the tendons.

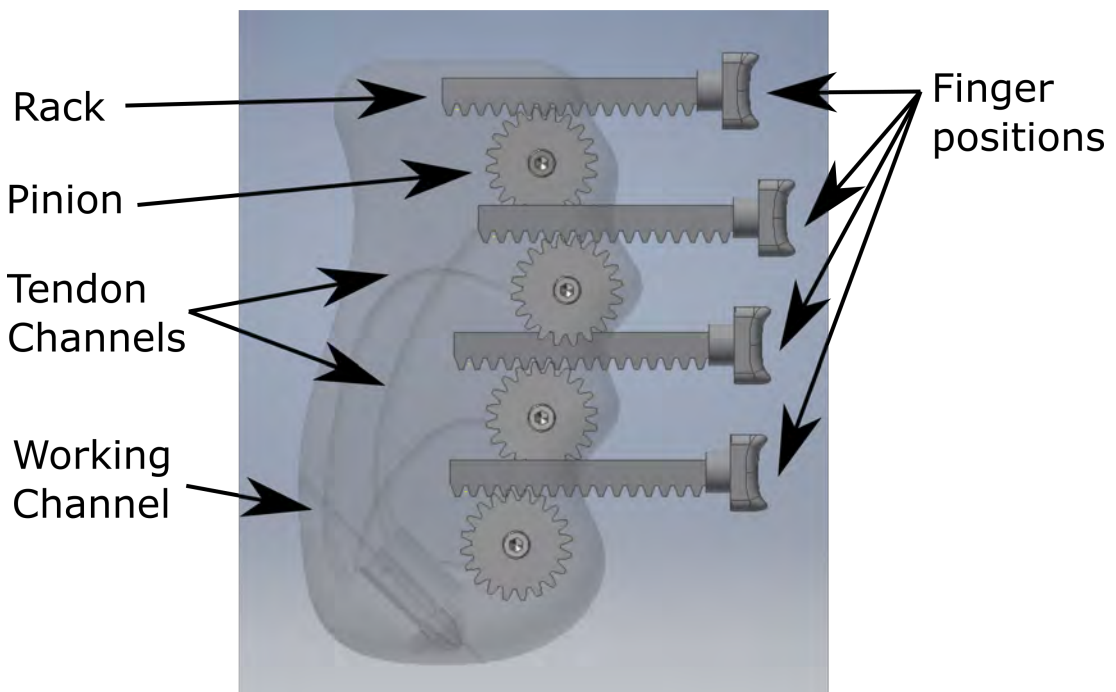


Figure 5.15: Section of handle design C, showing the rack and pinion mechanisms. The catheter is mounted into the handle at an angle at the bottom of the handle.

The tendons themselves run from the catheter's mounting point at the bottom of the handle, through a series of fully enclosed channels, to arrive tangentially aligned with the spools. This is a construction method that is only possible using 3D printing - the tendon channels are otherwise impossible to make, as they are completely internal features.

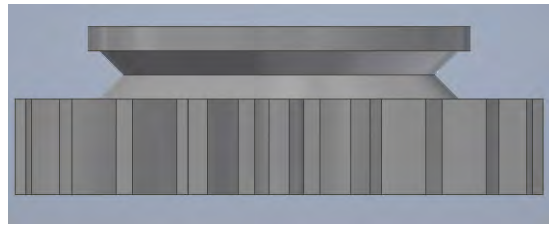


Figure 5.16: Side view of one of the geared spools used in design C. Note the V-groove which centers the tendon on the spool.

If the racks are actuated by hand, the spools rotate and apply force to the tendons, deflecting the tip of the catheter. To begin calculating the tendon displacement afforded by this mechanism we must begin with the size of the rack and pinion used. The module of a metric gear is described by Eqn. 5.1.

$$m = \frac{PCD}{n} \quad (5.1)$$

Where:

m is the module of the gear in mm,

PCD is the pitch circle diameter of the gear in mm, and

n is the number of teeth on the gear.

If the pitch circle diameter is known, the pitch circle circumference is known, and hence the lateral translation of the rack can be easily converted to the number of rotations of the pinion:

$$PCC = \pi \cdot PCD \quad (5.2)$$

Where PCC is the Pitch circle circumference in mm.

Rack displacement can be expressed in terms of pinion rotations by Eqn. 5.3.

$$R = \frac{s}{PCC} \quad (5.3)$$

Where:

R is the number of rotations completed by the pinion, and

s is the lateral displacement of the rack in mm.

Each pinion is rigidly attached to a spool which actuates a tendon. The displacement of this tendon can be calculated using Eqn. 5.4.

$$D = \frac{R}{\pi \cdot SD} \quad (5.4)$$

Where:

D is the displacement of the tendon in mm, and

SD is the spool diameter in mm.

For example, this design uses a module 1 pinion with 20 teeth, a matching rack with an available stroke length of approximately 50 mm, and a spool of 13 mm diameter. From Eqns. 5.1 and 5.2 we know that the pitch circle diameter is 20 mm, the circumference of which is 62.8 mm. Next, the number of pinion revolutions is calculated using Eqn. 5.3. This shows us that depressing the rack 50 mm yields 0.796 rotations of the pinion. Finally, Eqn. 5.4 yields that 0.796 rotations of a 13 mm spool cause 32.5 mm of tendon displacement.

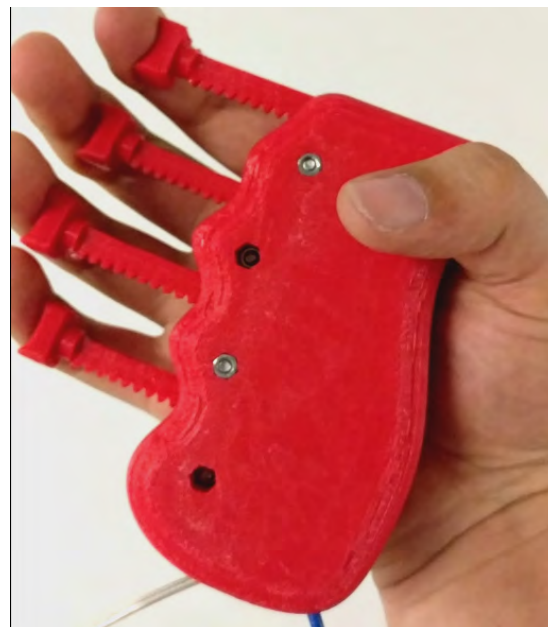


Figure 5.17: Photograph of design C in the hand.

5.4.1 Design C observations

Design C was better than designs A or B at steering the catheter, largely thanks to the hugely increased tendon displacement capacity allowing the user to simply "brute-force" steer the catheter regardless of the shape of the shaft. As a tradeoff,

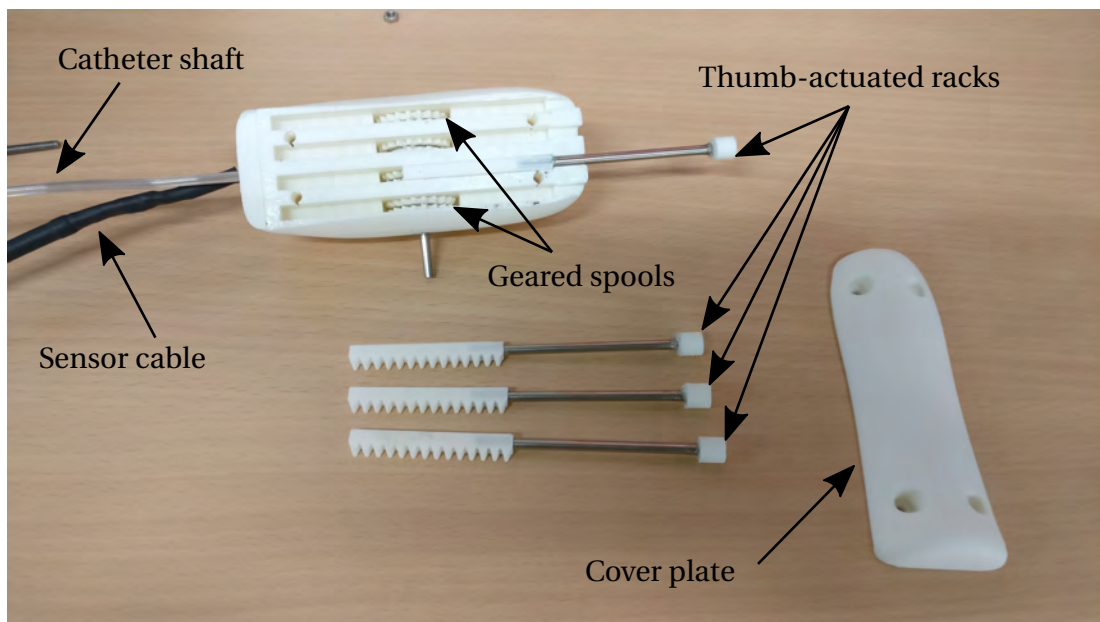


Figure 5.18: Variant of design C

the increased force available through the rack-and-pinion mechanism also tended to occasionally snap the tendons through a combination of overload and friction inside the tendon channels. Ergonomics also worsened by comparison to the previous handle designs, with design C requiring more hand strength and larger hands due to the spacing of the pinions.

Consequently a second handle design was developed as an offshoot of this design (Fig. 5.18). Instead of using the fingers to actuate the rack and pinion mechanism, this variant aligned the racks vertically in parallel and placed all the pinions on the same axis. This brought the controls together at the top of the handle, for actuation by thumb.

This approach was only a partial success. While it improved the feel of the handle, it made actuation more difficult as the controls were spaced too closely to one another to comfortably allow a thumb to pass between them.

Chapter 6

Pre-clinical investigation

As part of the larger Anser project of the UCC biodesign group, the catheters and catheter handles described in this work were used in a pre-clinical investigation combining the Anser EM tracking system, the CustusX imaging platform and the bronchoscopy catheter developed as part of this project. CustusX is a software platform designed to connect the imaging, instrument tracking and visualisations used in image-guided therapy and combine them into a full surgical navigation system. In this study, CustusX was used for the lung segmentation and real-time visualisation of catheter tip position.

The goal of the study was to demonstrate the possibilities of current open-source options in the tracking, visualisation, and targeting of peripheral lung nodules.

The investigation used female large white swine (*sus scrofa*, 25-38 kg) as the pre-clinical model, subject to local and national ethical approvals (APAFIS #9868-20170511 093041 02 v2, Ministère de l'Enseignement Supérieur de la Recherche et de l'Innovation, 2017).

First, each animal was anaesthetised using Propofol (4mg/kg bw) and paralysed using Rocuronium (0.8mg/kg bw). Anaesthesia was maintained using 1.15% Isofluorane in O₂ / N₂O. A pre-procedure CT scan was taken at 0.7 mm slice thickness. Peripheral nodules were simulated by using a radiopaque gel percutaneously injected into the outer lung via dual-lumen needle.

6. PRE-CLINICAL INVESTIGATION

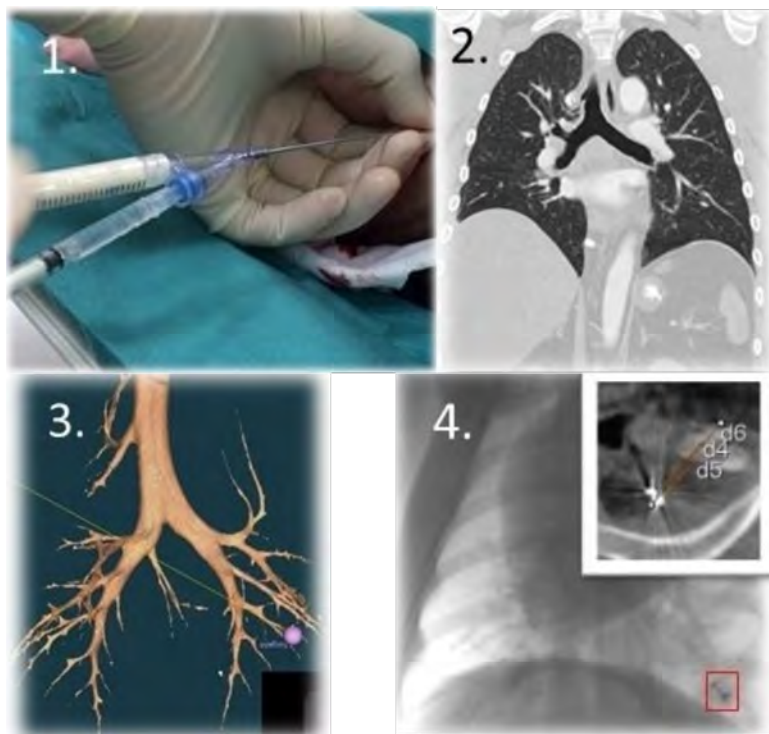


Figure 6.1: Overview of the experimental procedure.

Models were placed at four locations in the lung: the caudal left lobe, cranial right lobe, middle right lobe and caudal right lobe. The animal was again CT scanned, this time noting the "tumour" positions.

Following the second CT acquisition, the lung was segmented to extract a model of the airways using the virtual bronchoscopy plugin for CustusX. A rigid registration to the electromagnetic tracker was performed by means of an airway survey and cloudcompare tool [44].

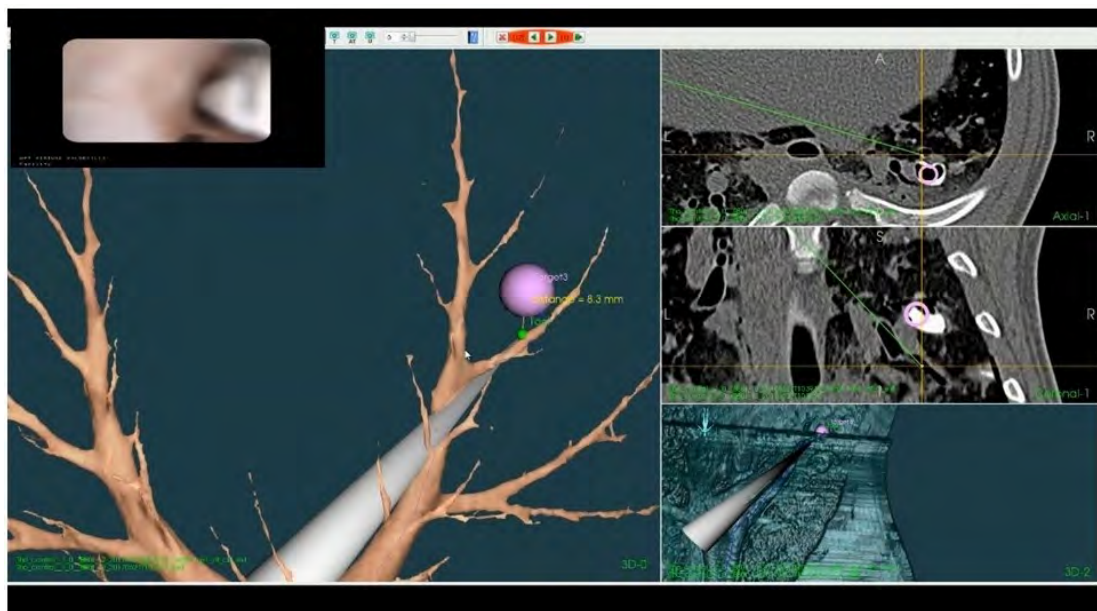


Figure 6.2: Screenshot of the CustusX navigation screen during navigation to a tumour in the lower right lobe. The bronchoscope view, segmented airway with real-time position, CT slices and CT volume render are all visible.

During the bronchoscopy, the operator sequentially navigated to each of the four virtual targets using the catheter / handle assemblies described in this project under electromagnetic guidance. Once the operator felt they could navigate no closer to the target, a 0.035" MReye embolization coil (Cook Medical, Limerick, Ireland) was deployed from the distal tip of the catheter to mark the target.

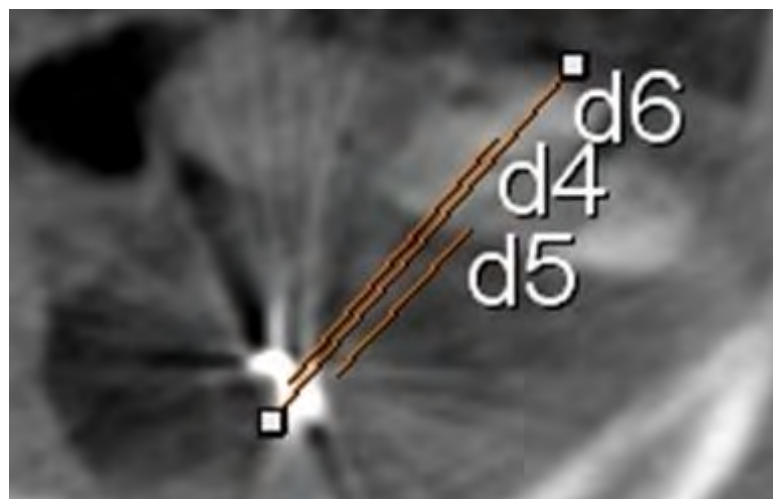


Figure 6.3: CT slice showing the embolisation coil (visible as a bright object in the centre of the image), the shortest distance to the tumour model (d5), the distance to the centre of the tumour model(d4), and the distance to the opposite side of the tumour model (d6).

6. PRE-CLINICAL INVESTIGATION

After navigating to each target site and deploying the marker, marker and tumour model positions were acquired using CT imaging by Artis Zeego. In all cases except for one, the operator was able to navigate to within 1cm of the tumour location (see Tbl. 6.1).

Table 6.1: Closest distance between tumour model and embolisation coil position

Tumour position	User 1	User 2
Upper Right Lung	2.48 mm	5.54 mm
Centre Left Lung	6.95 mm	12.04 mm
Centre Right Lung	3.79 mm	1.97 mm
Lower Right Lung	8.07 mm	1.39 mm

The pre-clinical study was a chance to gain valuable insights into how real users approach electromagnetically-guided bronchoscopy. It was found that a catheter for use as a tool positioning sheath in the airways does not need as high a degree of complexity. Indeed, having four tendons for omnidirectional deflection almost appears like over-engineering. It may have been just as effective to use an EM-tracked catheter with one tendon for unidirectional tip deflection, using the rotation of the bronchoscope to dictate the direction of movement.

Chapter 7

Conclusion

The focus of this project was to develop an actuation system for an electromagnetically guided catheter. As part of this project, a model for the behaviour of this catheter was created. This model was tested using custom-built hardware and software. Several manual actuation handles were designed, prototyped and tested, and a pre-clinical investigation carried out on in-vivo models.

The experience gathered during this project and the pre-clinical study calls into question the need for both 6DOF sensing and significant catheter steerability. Both operators noted that being able to see the roll angle of the catheter would have been of little assistance to the actual act of navigating to the airway target, and neither operator made significant use of the catheter's steerable aspects. To a bronchoscopist, it is far more intuitive to navigate by combining scope rotation and scope position to angle the catheter in such a way that it enters the correct airway when pushed forward through the endoscope channel. The study also showed that EM tracking is a viable technology on open-source platforms. The results of the pre-clinical work suggest an improved set of requirements for the next iteration of the tip-tracked bronchoscopy catheters:

- One 5-DOF EM tracking sensor at the tip of the catheter.
- Single-tendon tip deflection with a short distal tip for navigation in tight spaces, and a maximum deflection of 45°.
- Braided reinforcements to the catheter shaft to improve axial strength and reduce buckling when actuating the tendon.
- A smaller OD of 2.7 mm for improved endoscope compatibility would also be beneficial. While therapeutic bronchoscopes are not uncommon, a 2.8 mm

7. CONCLUSION

working channel is the de facto standard for endoscopic procedures throughout the body.

The preliminary results of the pre-clinical evaluation indicate that EM-tracked bronchial catheters can serve as a platform technology that works well with other diagnostic or therapeutic approaches. One such combination could be a confocal microscope probe mounted to the tip of such a catheter for in-vivo pathology, sparing the need for biopsies which may or may not sample from the correct location - all with minimal radiation exposure for the staff and patient. In terms of therapeutic tools, there is a possibility for combining this platform with RF or cryoablation to diagnose and treat malignant nodules in a single bronchoscopy session, which would present a significant improvement over the current multi-operation approach. This work may provide a worthwhile starting point for such investigations.

Appendix A

Data

Raw data can be found in a google drive folder by scanning this QR code on a mobile device, by clicking the qr code (if you are reading this from a PDF), or if all else fails by manually entering the URL:

<https://drive.google.com/open?id=1pF2TBJOjN6FZC2gvHEarFwqTJztLGV7I> .



A.1 Catheter 1 single-tendon deflection

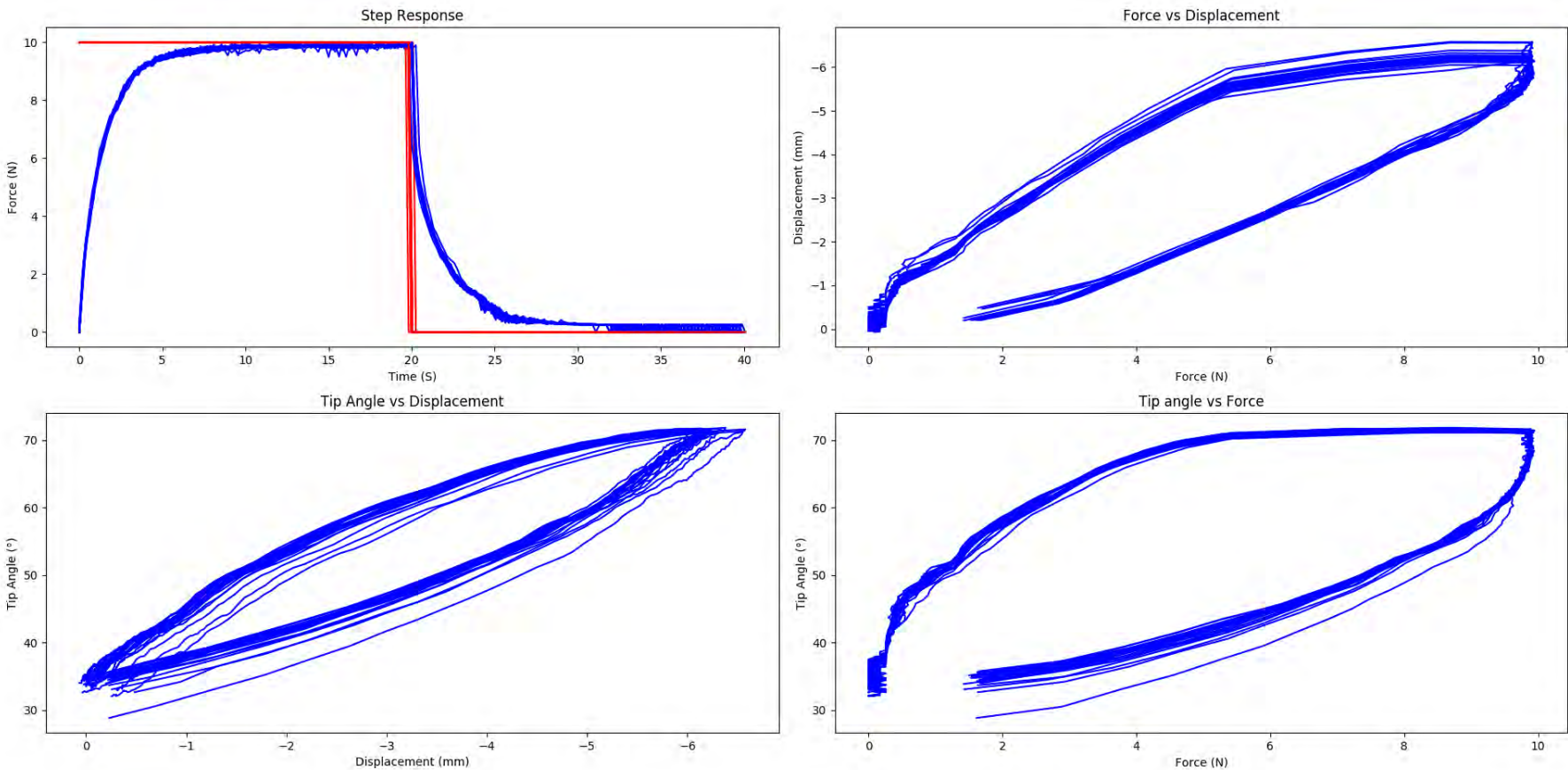


Figure A.1: Catheter 1, tendon A raw data plots

A. DATA

A.1 Catheter 1 single-tendon deflection

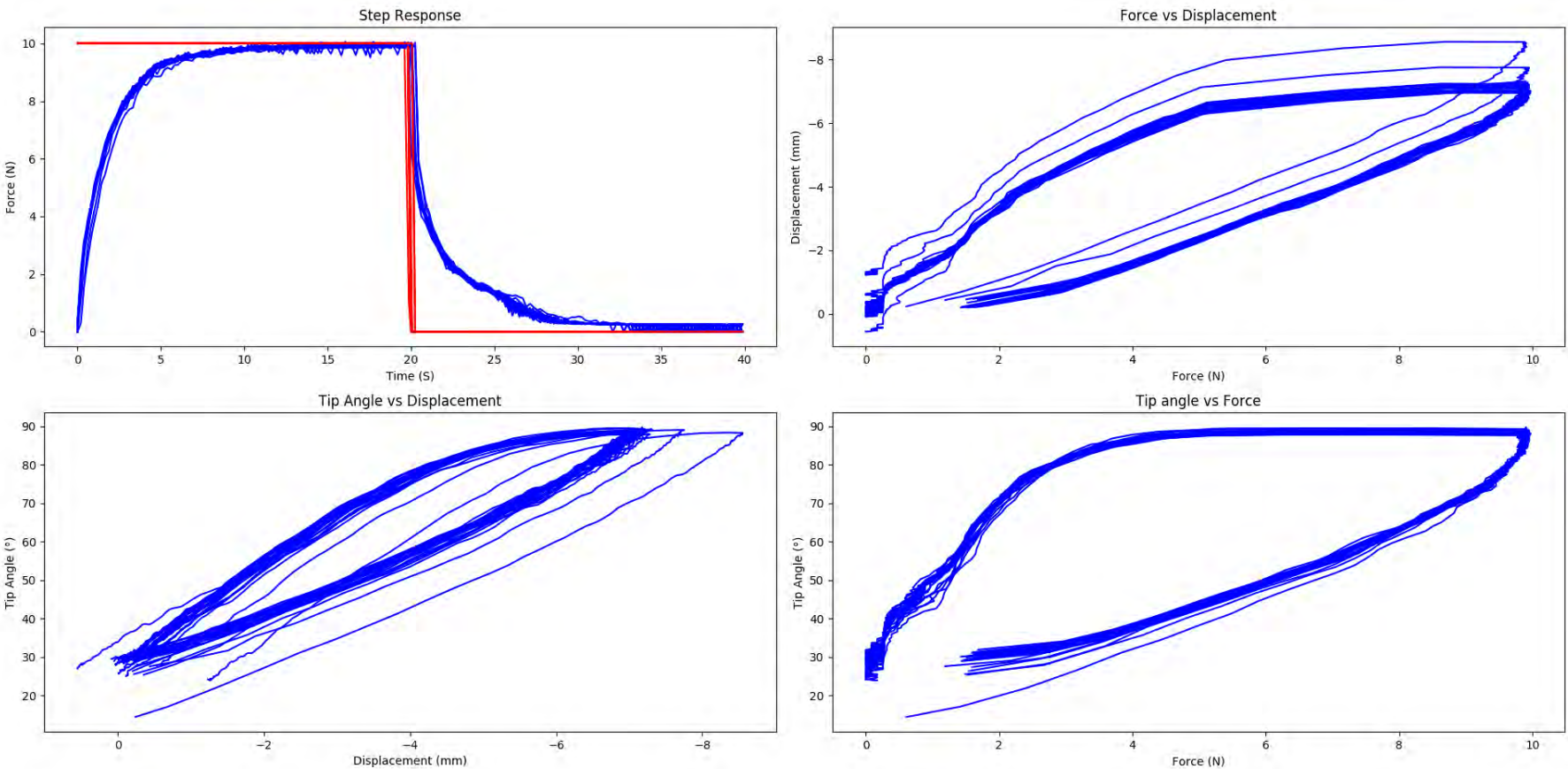


Figure A.2: Catheter 1, tendon B raw data plots

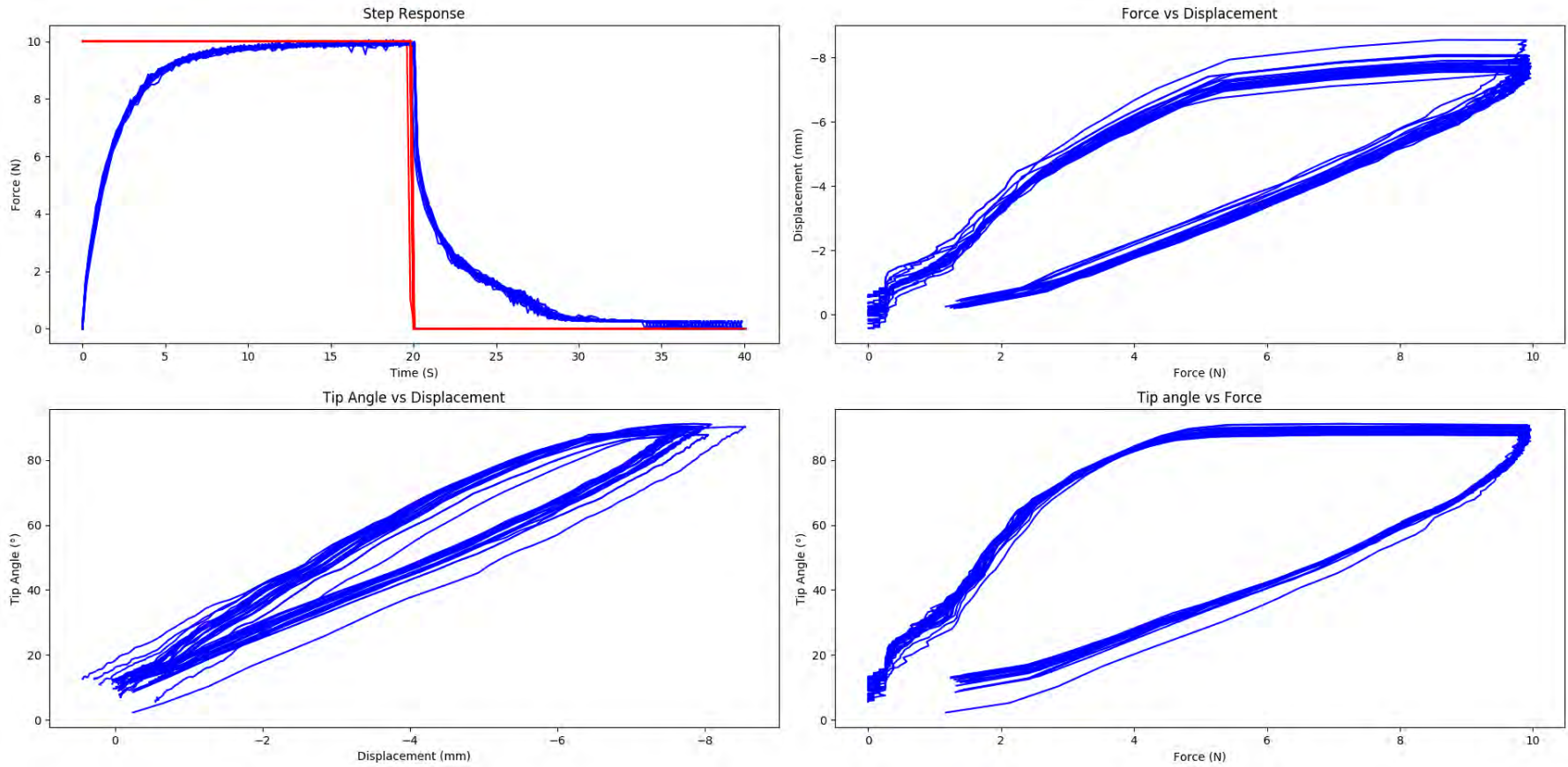


Figure A.3: Catheter 1, tendon C raw data plots

A. DATA

A.1 Catheter 1 single-tendon deflection

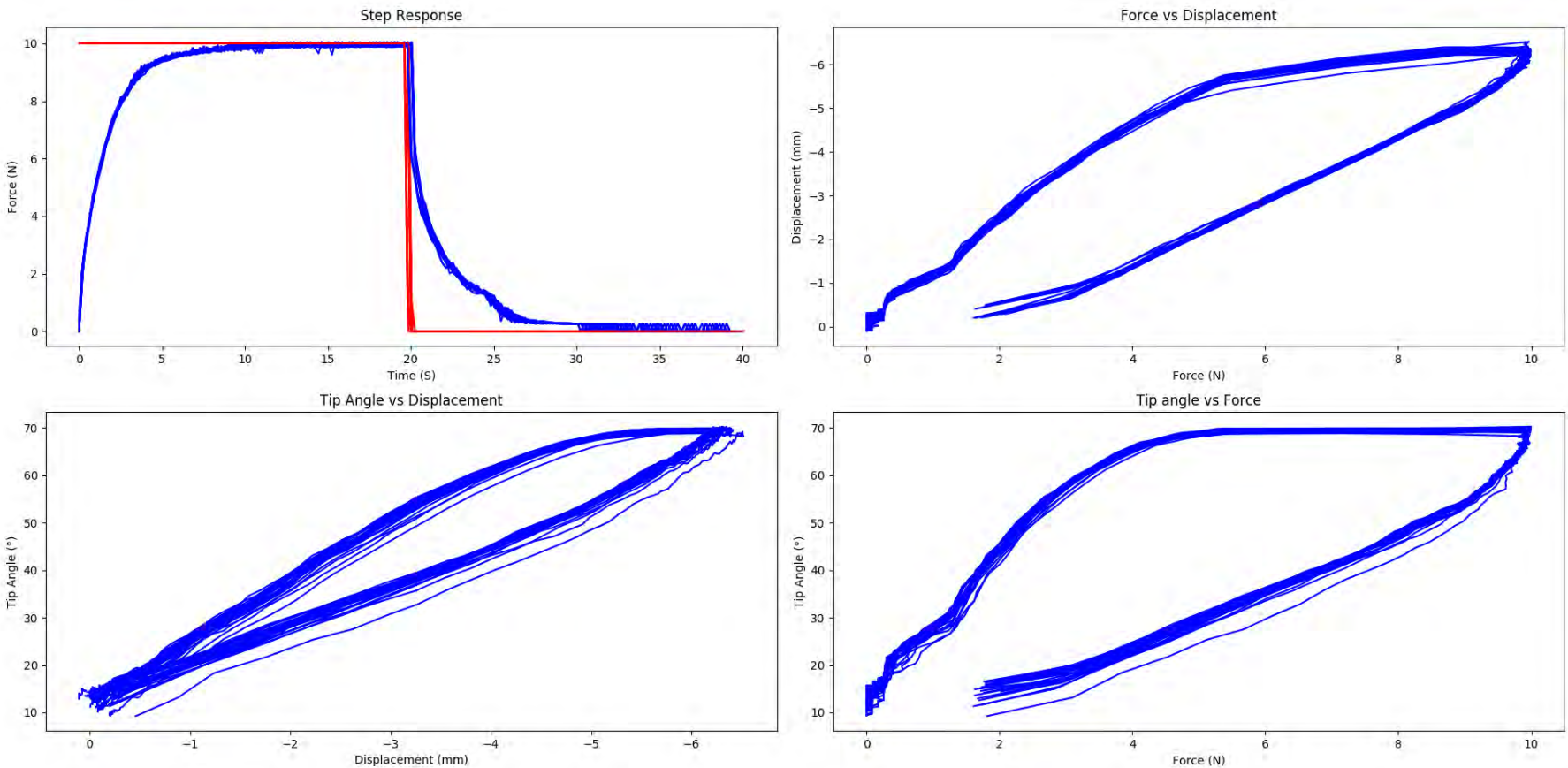


Figure A.4: Catheter 1, tendon D raw data plots

A.2 Catheter 2 single-tendon deflection

116

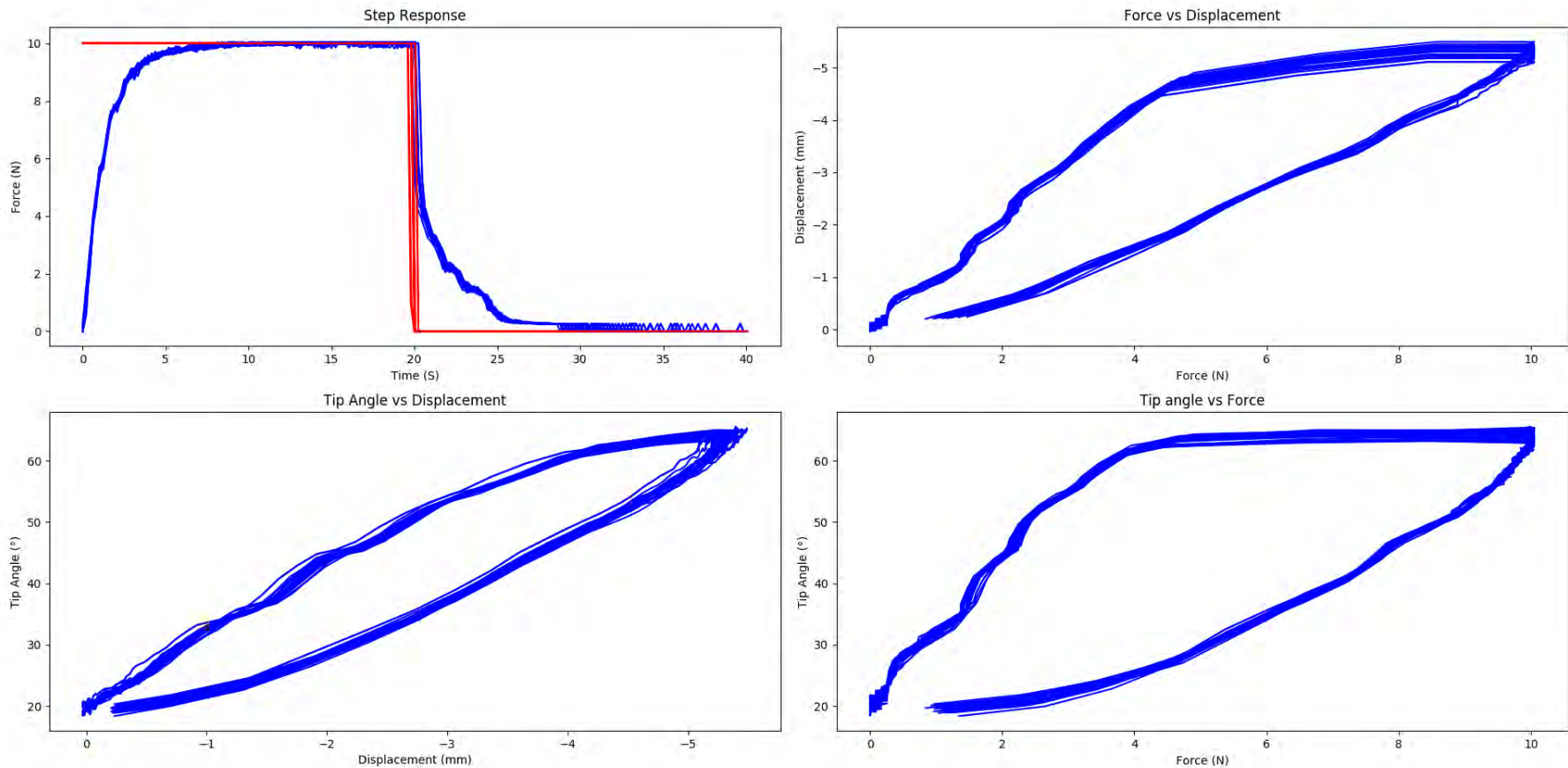


Figure A.5: Catheter 2, tendon A raw data plots

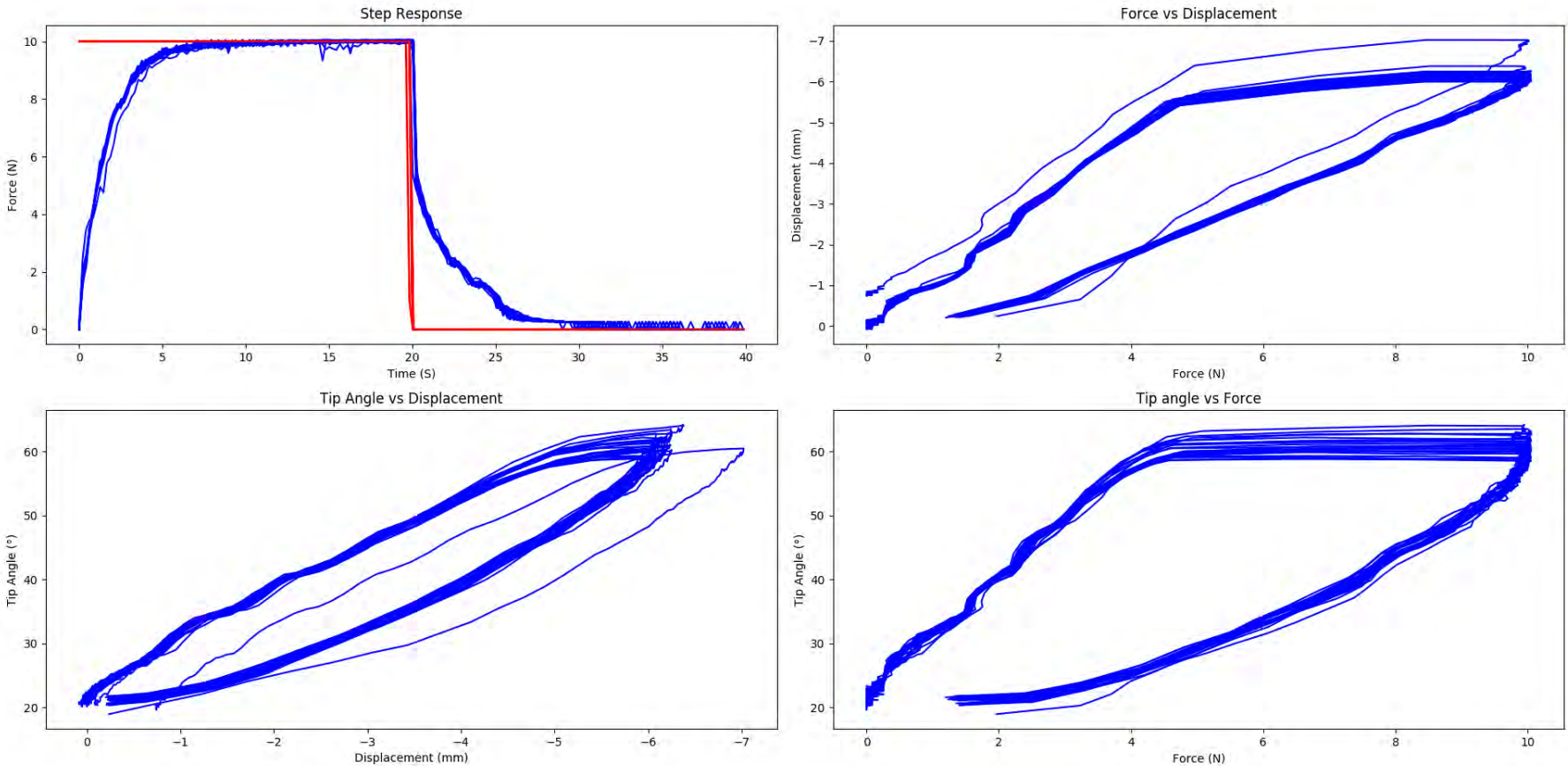


Figure A.6: Catheter 2, tendon B raw data plots

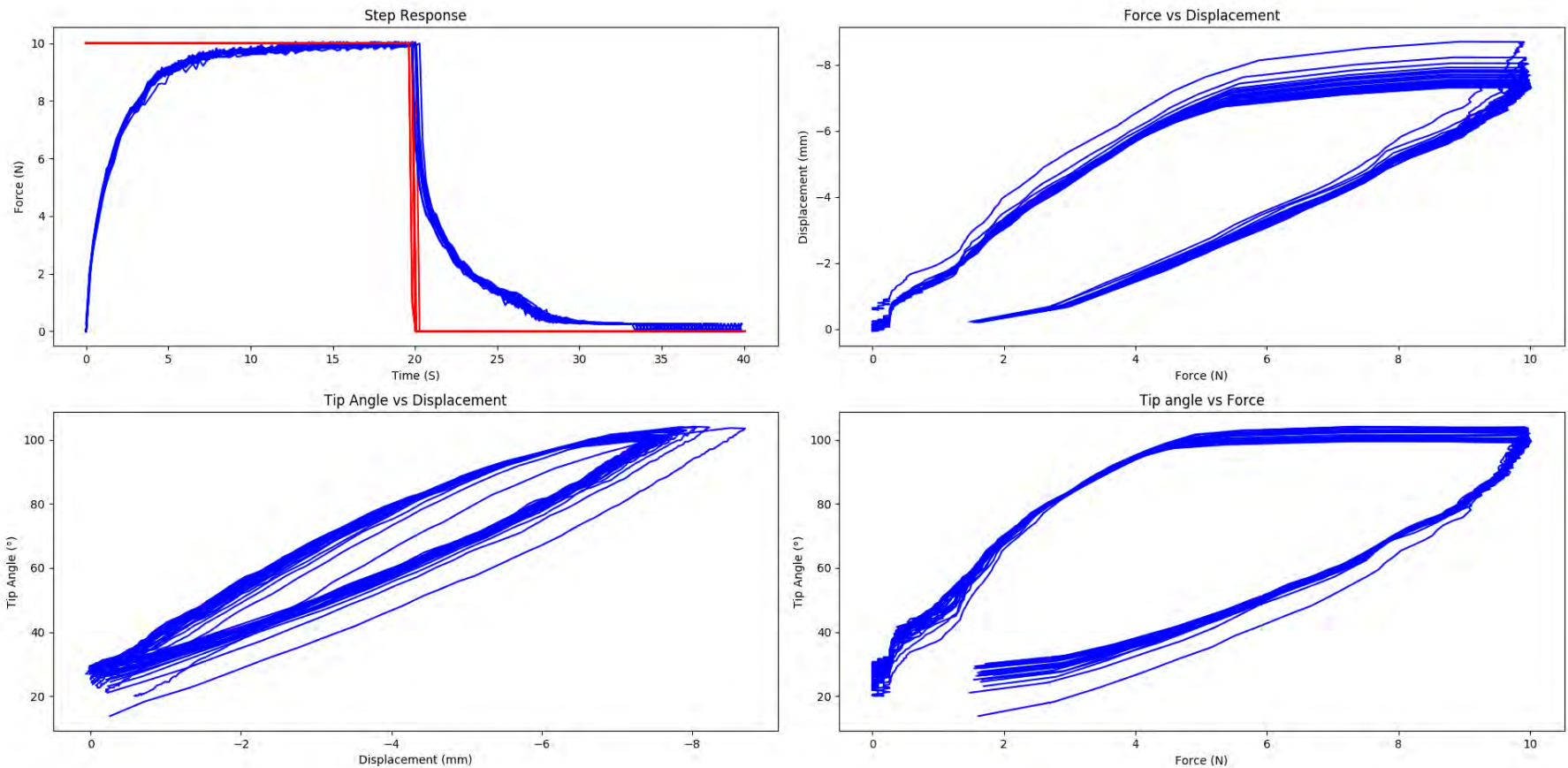


Figure A.7: Catheter 2, tendon C raw data plots

A. DATA

A.2 Catheter 2 single-tendon deflection

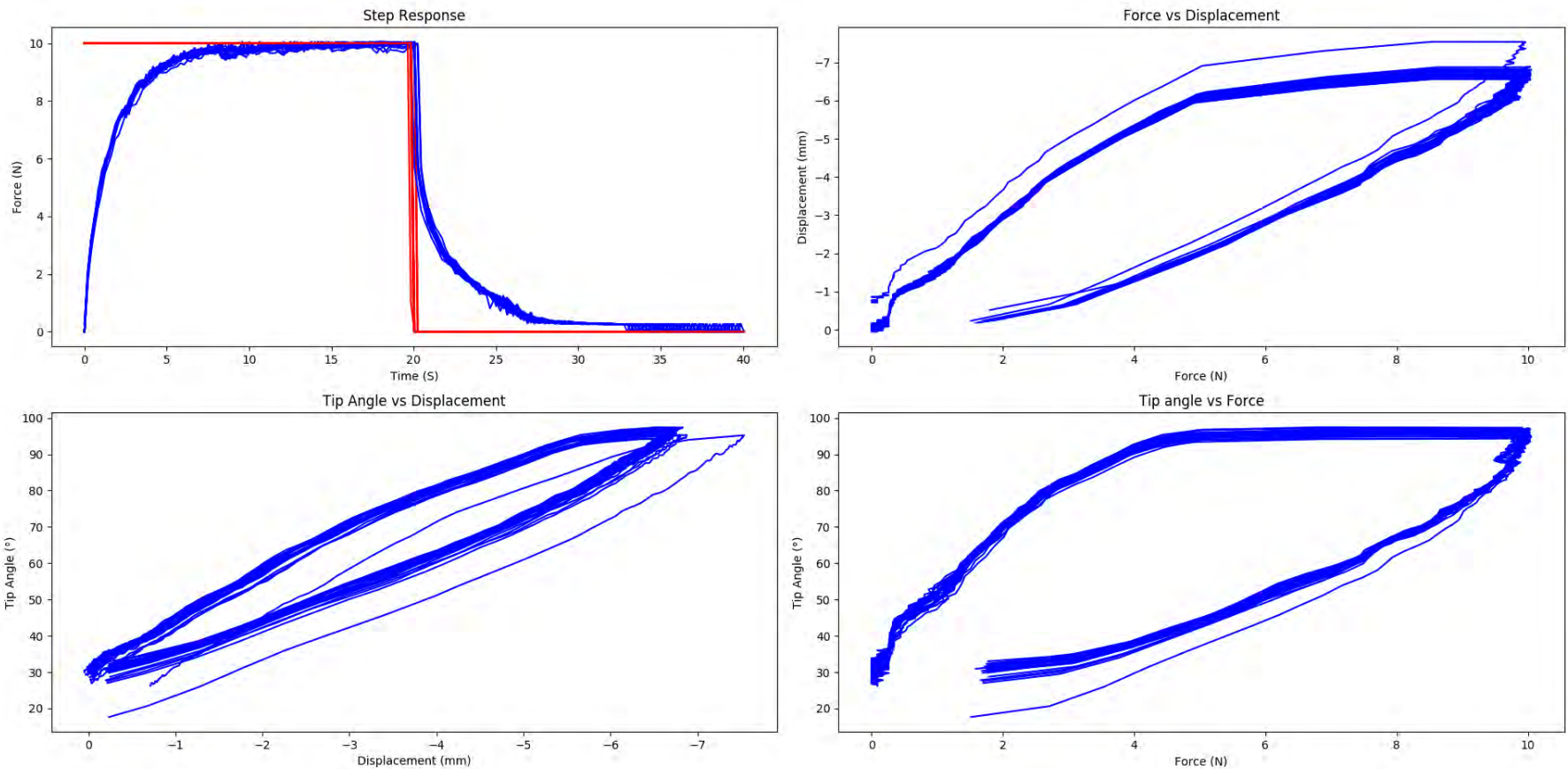


Figure A.8: Catheter 2, tendon D raw data plots

A.3 Catheter 1 hysteresis

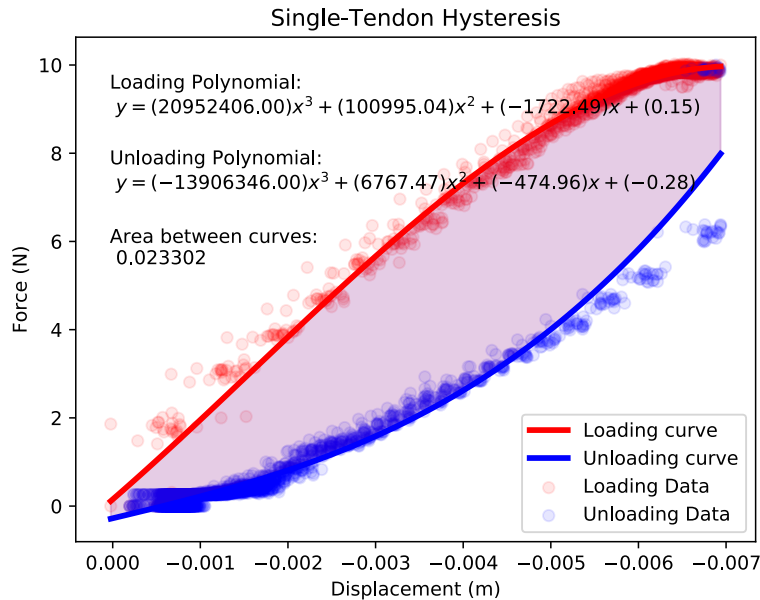


Figure A.9: Force-Displacement graph of Catheter 1, Tendon A showing the data points, regression curves and area between loading and unloading curves

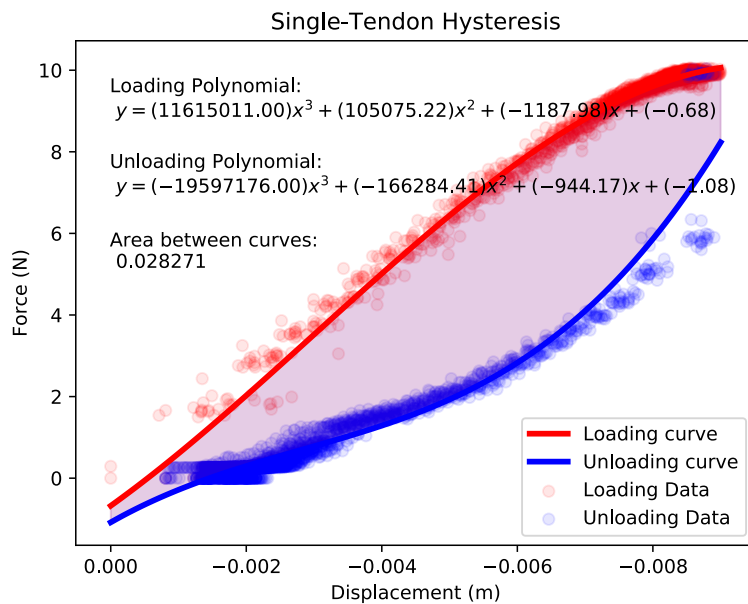


Figure A.10: Force-Displacement graph of Catheter 1, Tendon B showing the data points, regression curves and area between loading and unloading curves

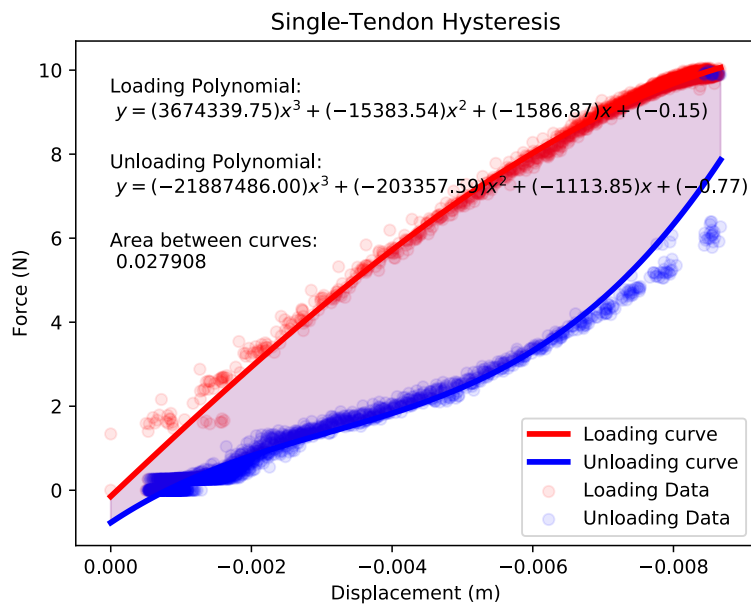


Figure A.11: Force-Displacement graph of Catheter 1, Tendon C showing the data points, regression curves and area between loading and unloading curves

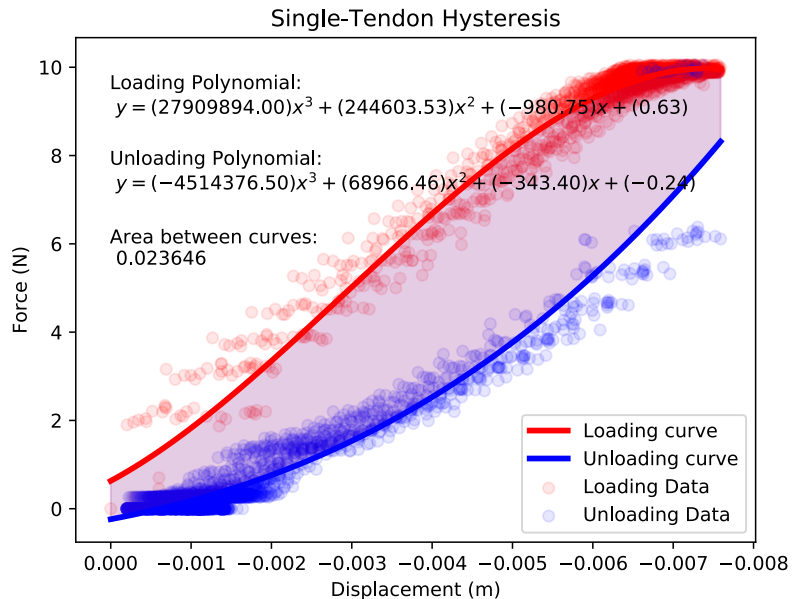


Figure A.12: Force-Displacement graph of Catheter 1, Tendon D showing the data points, regression curves and area between loading and unloading curves

A.4 Catheter 2 hysteresis

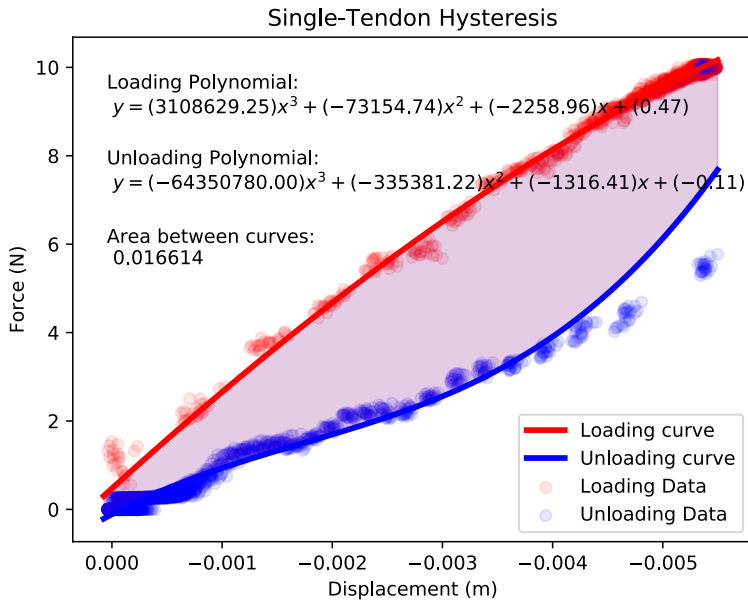


Figure A.13: Force-Displacement graph of Catheter 2, Tendon A showing the data points, regression curves and area between loading and unloading curves

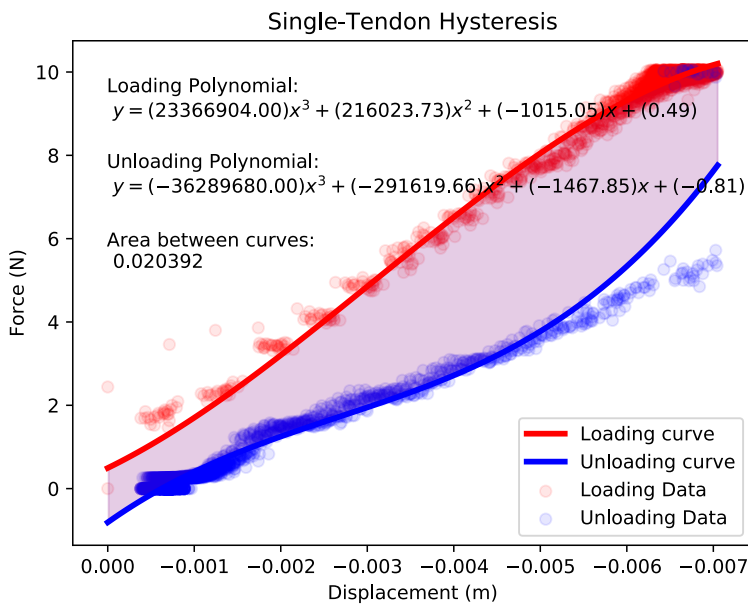


Figure A.14: Force-Displacement graph of Catheter 2, Tendon B showing the data points, regression curves and area between loading and unloading curves

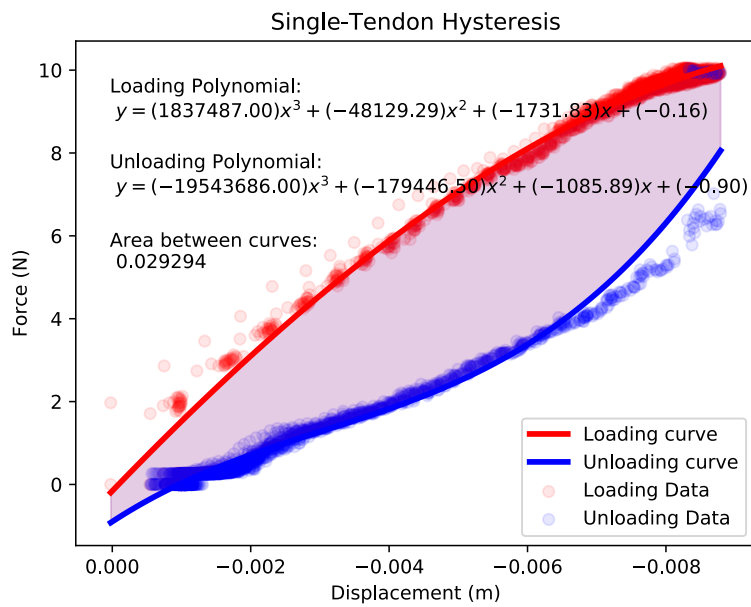


Figure A.15: Force-Displacement graph of Catheter 2, Tendon C showing the data points, regression curves and area between loading and unloading curves

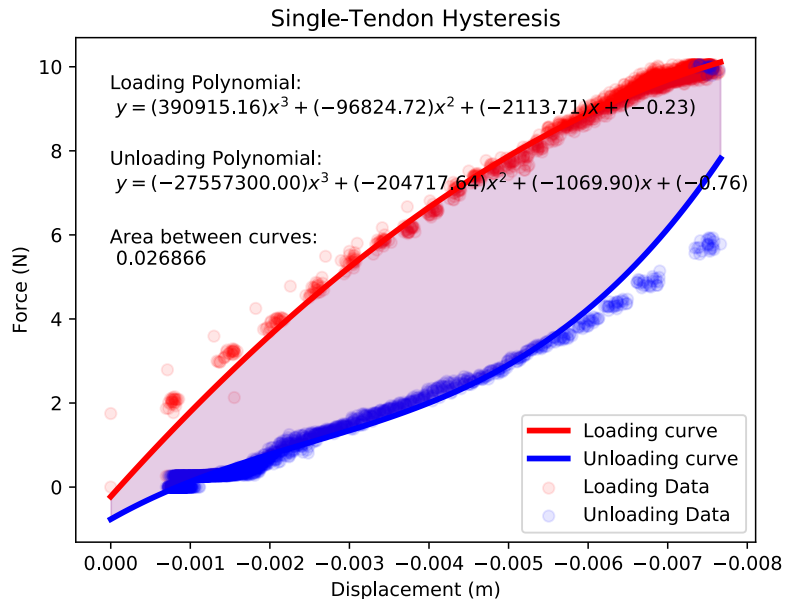


Figure A.16: Force-Displacement graph of Catheter 2, Tendon D showing the data points, regression curves and area between loading and unloading curves

A.5 Catheter 1 tip angle - load relationship

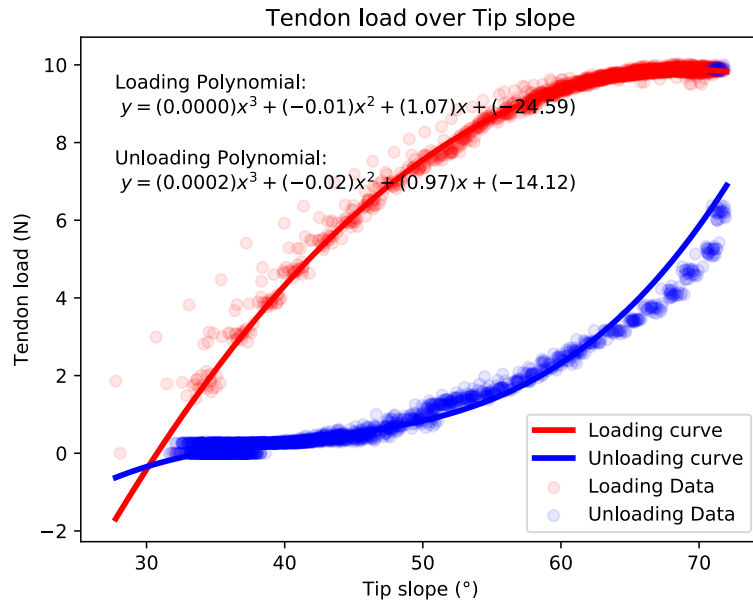


Figure A.17: A plot of tendon load over tip angle for catheter 1, tendon A. Note the distinct loading and unloading curves.

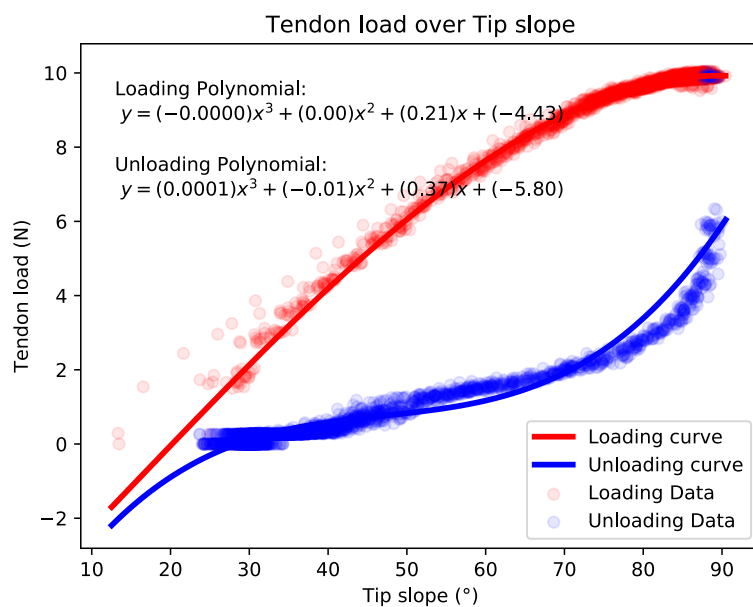


Figure A.18: A plot of tendon load over tip angle for catheter 1, tendon B. Note the distinct loading and unloading curves.

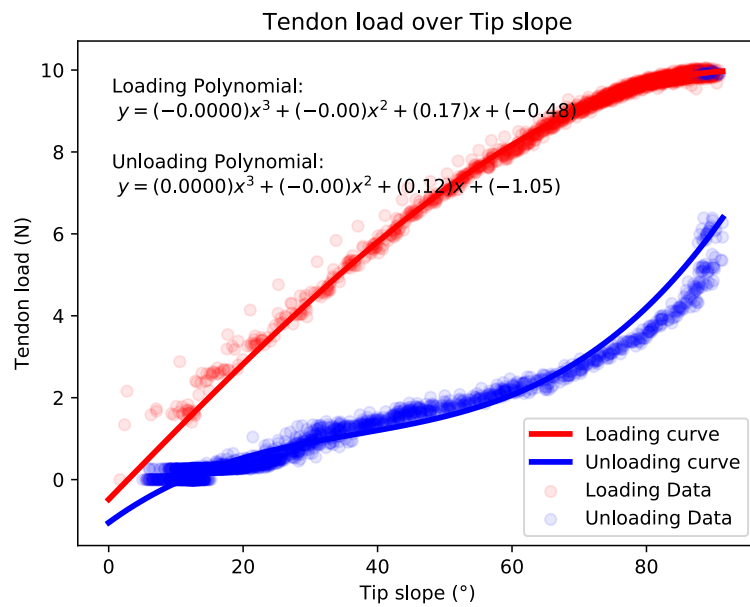


Figure A.19: A plot of tendon load over tip angle for catheter 1, tendon C. Note the distinct loading and unloading curves.

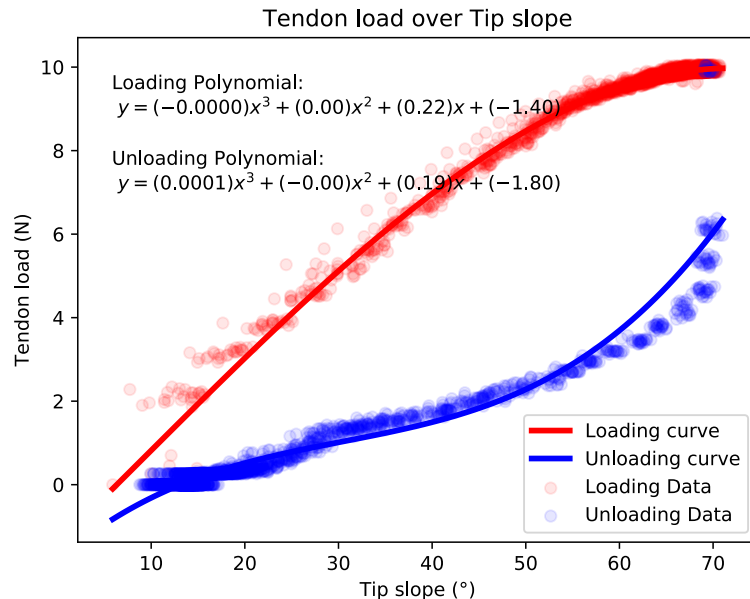


Figure A.20: A plot of tendon load over tip angle for catheter 1, tendon D. Note the distinct loading and unloading curves.

A.6 Catheter 2 tip angle - load relationship

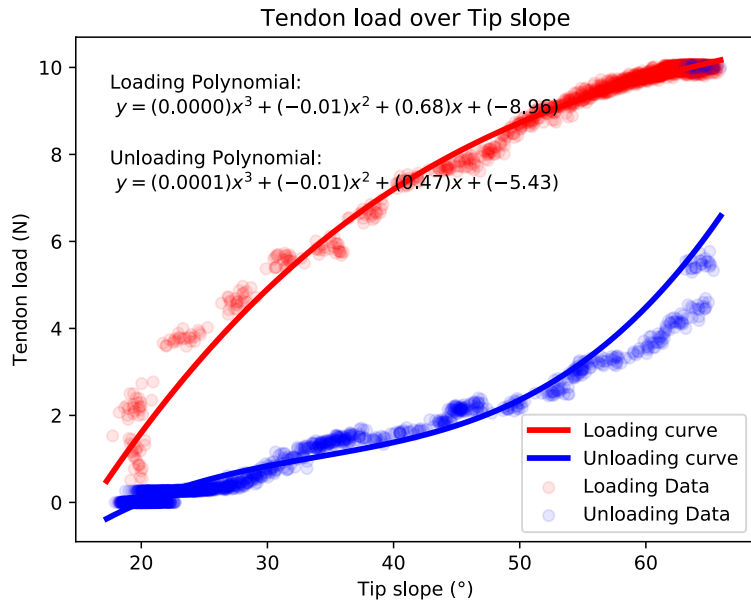


Figure A.21: A plot of tendon load over tip angle for catheter 2, tendon A. Note the distinct loading and unloading curves.

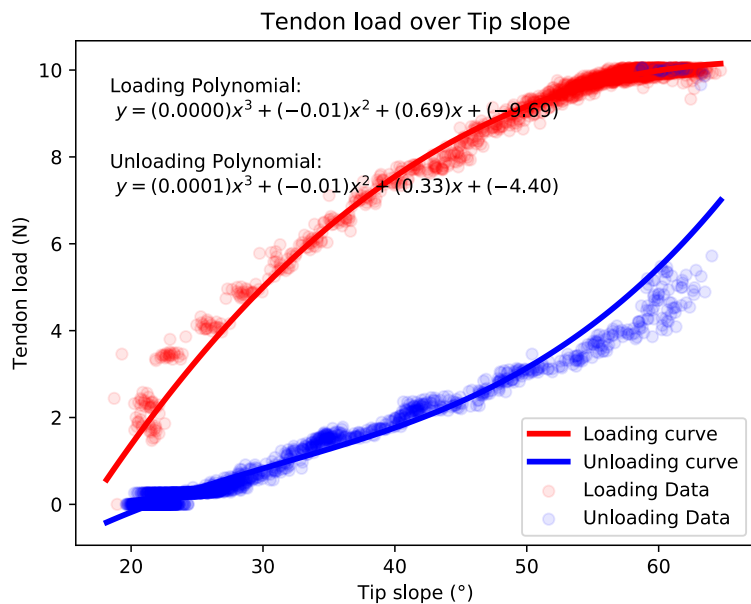


Figure A.22: A plot of tendon load over tip angle for catheter 2, tendon B. Note the distinct loading and unloading curves.

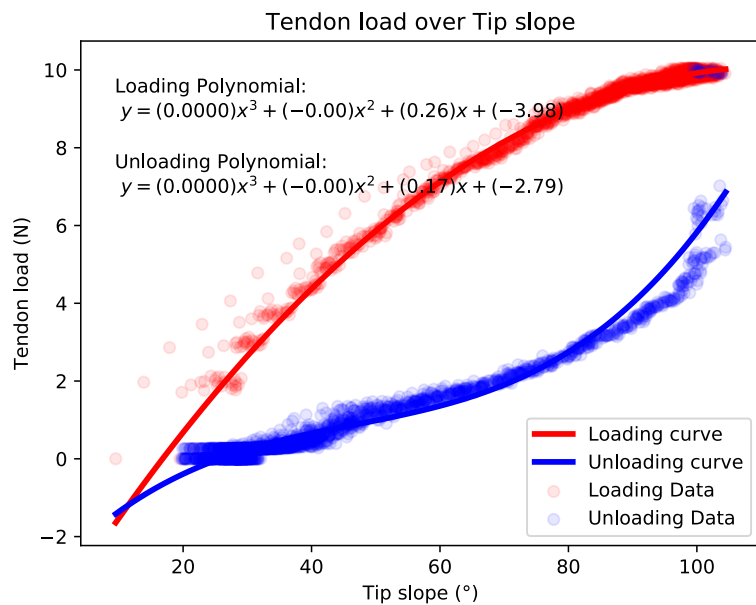


Figure A.23: A plot of tendon load over tip angle for catheter 2, tendon C. Note the distinct loading and unloading curves.

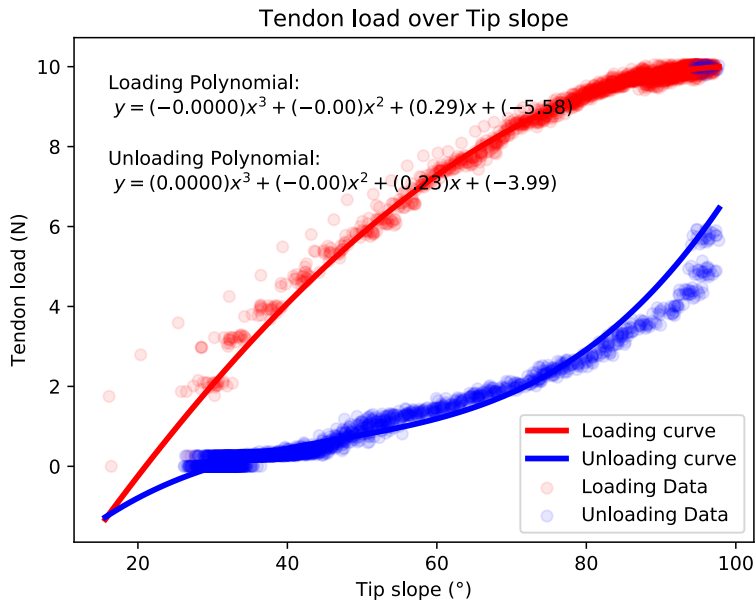


Figure A.24: A plot of tendon load over tip angle for catheter 2, tendon D. Note the distinct loading and unloading curves.

A.7 Multi-tendon error plots

128

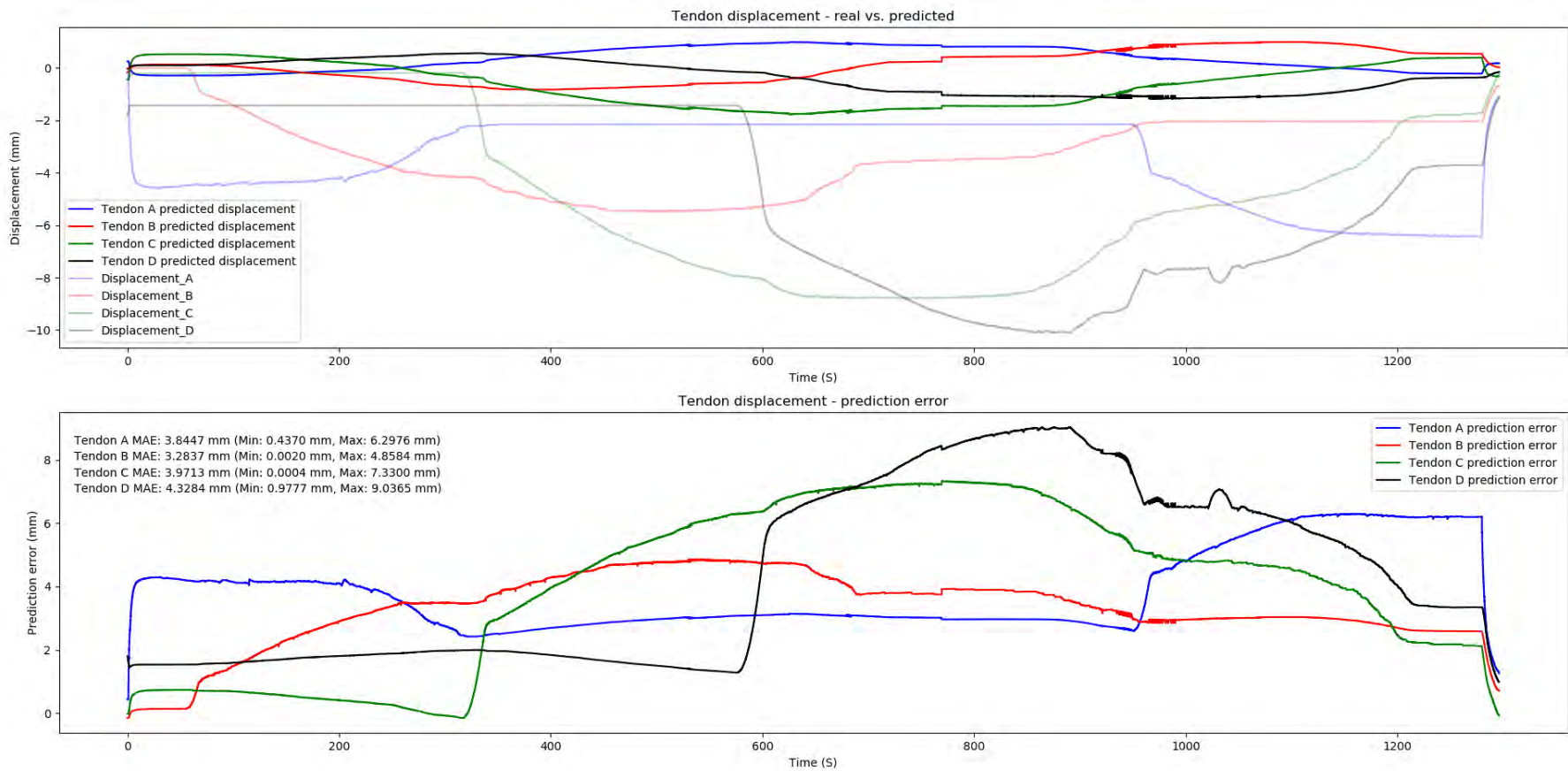


Figure A.25: Plots of real and predicted deflection, as well as the prediction error over time

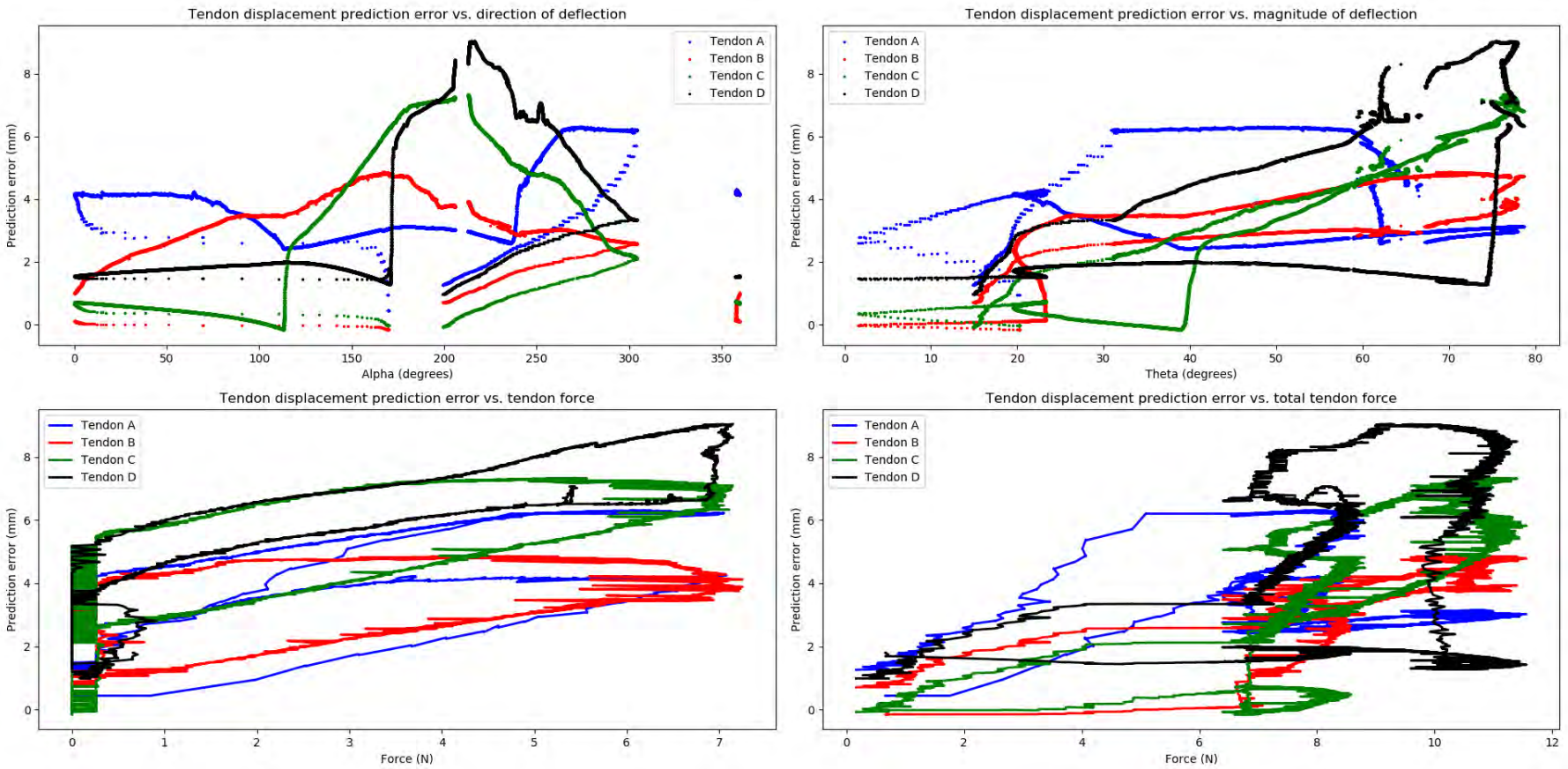


Figure A.26: Plots of displacement prediction error vs: direction of tip deflection, magnitude of tip deflection, individual tendon force, and total tendon force.

Appendix B

Code

All code can be found in a google drive folder by scanning this QR code on a mobile device, by clicking the qr code (if you are reading this from a PDF), or if all else fails by manually entering the URL:

<https://drive.google.com/open?id=1pF2TBJOjN6FZC2gvHEarFwqTJztLGV7I> .



Bibliography

- [1] American Cancer Society, “Key Statistics for Lung Cancer,” 2017. [Online]. Available: <https://www.cancer.org/cancer/non-small-cell-lung-cancer/about/key-statistics.html> [Accessed: 2018-09-10]
- [2] ——, “What Is Non-Small Cell Lung Cancer?” pp. 1–4, 2018. [Online]. Available: <https://www.cancer.org/cancer/non-small-cell-lung-cancer/about/what-is-non-small-cell-lung-cancer.html> <https://www.cancer.org/cancer/non-small-cell-lung-cancer/about/what-is-non-small-cell-lung-cancer.html#{refere> [Accessed: 2018-09-10]
- [3] “CustusX - Home.” [Online]. Available: <https://www.custusx.org/> [Accessed: 2018-04-06]
- [4] H. A. Jaeger, A. M. Franz, K. O’Donoghue, A. Seitel, F. Trauzettel, L. Maier-Hein, and P. Cantillon-Murphy, “Anser EMT: the first open-source electromagnetic tracking platform for image-guided interventions,” *International Journal of Computer Assisted Radiology and Surgery*, Mar 2017. [Online]. Available: <http://link.springer.com/10.1007/s11548-017-1568-7> [Accessed: 2018-04-06]
- [5] “SwiftNINJA Steerable Microcatheter.” [Online]. Available: <https://www.merit.com/peripheral-intervention/angiography/microcatheters/swiftninja-steerable-microcatheter/> [Accessed: 2018-04-06]
- [6] “Electrophysiology Products Catalog,” 2014. [Online]. Available: <http://www.bostonscientific.com/content/dam/bostonscientific/ep/general/Boston%20Scientific%202014%20Electrophysiology%20Products%20Catalog.pdf> [Accessed: 2018-04-06]
- [7] A. Ali, D. H. Plettenburg, and P. Breedveld, “Steerable Catheters in Cardiology: Classifying Steerability and Assessing Future Challenges,” *IEEE Transactions on Biomedical Engineering*, vol. 63, no. 4, pp. 679–693, Apr 2016. [Online]. Available: <http://ieeexplore.ieee.org/document/7399367/> [Accessed: 2018-04-06]

- [8] T. Liu, N. L. Poirot, D. Franson, N. Seiberlich, M. Griswold, and M. Cavusoglu, "Modeling and Validation of the Three Dimensional Deflection of an MRI-Compatible Magnetically-Actuated Steerable Catheter," *IEEE Transactions on Biomedical Engineering*, no. 99, pp. 2142 – 2154, 2016. [Online]. Available: <http://ieeexplore.ieee.org/document/7361993/> [Accessed: 2018-04-06]
- [9] P. Chastagner, "Medical catheters thermally manipulated by fiber optic bundles," Patent US5 152 748 A, 1991. [Online]. Available: <http://www.google.com/patents/US5152748> [Accessed: 2018-04-06]
- [10] T. Eidenschink, J. Weber, K. A. Jagger, and M. Heidner, "Embedded electroactive polymer structures for use in medical devices," Patent US7 951 186 B2, 2006. [Online]. Available: <http://www.google.com/patents/US7951186> [Accessed: 2018-04-06]
- [11] "Blazer Dx-20 Bidirectional Duodecapolar Diagnostic Catheter." [Online]. Available: <http://www.bostonscientific.com/en-US/products/catheters--diagnostic/blazer-dx-20.html> [Accessed: 2018-04-06]
- [12] B. D. Heinzelman and C. J. Brooks, "Catheter steering mechanism," Patent US5 364 351 A, Also published as US5 456 664, 1992. [Online]. Available: <http://www.google.com/patents/US5364351> [Accessed: 2018-04-06]
- [13] "RADIA Bidirectional Steerable Diagnostic Catheter | Boston Scientific." [Online]. Available: <http://www.bostonscientific.com/en-US/products/catheters--diagnostic/radia.html> [Accessed: 2018-04-06]
- [14] "POLARIS X Steerable Diagnostic Catheters| Boston Scientific | Boston Scientific." [Online]. Available: <http://www.bostonscientific.com/en-US/products/catheters--diagnostic/polaris-x.html> [Accessed: 2018-04-06]
- [15] "ORBITER ST Steerable Diagnostic Catheter | Boston Scientific." [Online]. Available: <http://www.bostonscientific.com/en-US/products/catheters--diagnostic/orbiter-st.html> [Accessed: 2018-04-06]
- [16] "News Releases," 2011. [Online]. Available: <http://news.bostonscientific.com/2016-05-03-Boston-Scientific-Announces-U-S-FDA-Approval-of-Navigation-Enabled-Ablation-Catheters> [Accessed: 2018-04-06]
- [17] "IntellaNav XP Temperature Ablation Catheter." [Online]. Available: https://www.bostonscientific.com/content/dam/Manuals/us/current-rev-en/90902676-01B_IntellaNav_XP_DFU_en-USA_S.pdf [Accessed: 2018-04-06]

- [18] W. A. Baaklini, M. A. Reinoso, A. B. Gorin, A. Sharafkaneh, and P. Manian, “Diagnostic yield of fiberoptic bronchoscopy in evaluating solitary pulmonary nodules.” *Chest*, vol. 117, no. 4, pp. 1049–1054, apr 2000. [Online]. Available: <http://www.ncbi.nlm.nih.gov/pubmed/10767238>
- [19] T. R. Gildea, P. J. Mazzone, D. Karnak, M. Meziane, and A. C. Mehta, “Electromagnetic navigation diagnostic bronchoscopy: A prospective study,” *American Journal of Respiratory and Critical Care Medicine*, vol. 174, no. 9, pp. 982–989, nov 2006. [Online]. Available: <http://www.atsjournals.org/doi/abs/10.1164/rccm.200603-344OC>
- [20] “3D Slicer.” [Online]. Available: <https://www.slicer.org/> [Accessed: 2018-07-05]
- [21] “All Product Catalog Pages.” [Online]. Available: <https://professional.sjm.com/resources/all-product-catalogs> [Accessed: 2018-04-06]
- [22] “Products.” [Online]. Available: <https://www.merit.com/products/> [Accessed: 2018-04-06]
- [23] Medtronic, “Steerable Sheath - Overview - FlexCath Advance.” [Online]. Available: <https://www.medtronic.com/us-en/healthcare-professionals/products/cardiac-rhythm/ablation-atrial-fibrillation/flexcath-advance-steerable-sheath.html> [Accessed: 2018-04-06]
- [24] P. J. Snoke, M. J. Mark, and D. S. Rowley, “Steerable catheter having disposable module and sterilizable handle and method of connecting same,” Patent US6 007 531A, 1999. [Online]. Available: <https://patents.google.com/patent/US6007531A> [Accessed: 2018-04-06]
- [25] C. Oskin, I. Ostrovsky, D. W. Robertson, and M. Barenboym, “Steering mechanism,” Patent US8 834 357 B2, Also published as CA2 743 301A1, EP2 355 885A1, US9 380 930, US20 100 121 147, US20 140 350 342, WO2 010 056 638A1, 2008. [Online]. Available: <http://www.google.com/patents/US8834357> [Accessed: 2018-04-06]
- [26] D. Freed, “Handle for steerable catheter,” Patent US20 130 253 469 A1, Also published as US8 465 442, US20 050 256 375, WO2 005 113 050A1, 2013. [Online]. Available: <https://www.google.com/patents/US20130253469> [Accessed: 2018-04-06]
- [27] J. Marescaux and F. Rubino, “Transcontinental robot-assisted remote telesurgery, feasibility and potential applications,” in *Teleophthalmology*. Lippincott,

- Williams, and Wilkins, Apr 2006, vol. 235, no. 4, pp. 261–265. [Online]. Available: <http://www.ncbi.nlm.nih.gov/pubmed/11923603> [Accessed: 2018-04-06]
- [28] C. V. Riga, C. D. Bicknell, A. Rolls, N. J. Cheshire, and M. S. Hamady, “Robot-assisted fenestrated endovascular aneurysm repair (FEVAR) using the magellan system,” *Journal of Vascular and Interventional Radiology*, vol. 24, no. 2, pp. 191–196, Feb 2013. [Online]. Available: <http://linkinghub.elsevier.com/retrieve/pii/S1051044312010354> [Accessed: 2018-04-06]
- [29] M. Khoshnam and R. V. Patel, “Robotics-assisted catheter manipulation for improving cardiac ablation efficiency,” in *Biomedical Robotics and Biomechatronics (2014 5th IEEE RAS & EMBS International Conference on*, Aug 2014, pp. 308–313. [Online]. Available: <http://ieeexplore.ieee.org/document/6913794/> [Accessed: 2018-04-06]
- [30] M. Khoshnam, A. C. Skanes, and R. V. Patel, “Modeling and estimation of tip contact force for steerable ablation catheters,” *IEEE Transactions on Biomedical Engineering*, vol. 62, no. 5, pp. 1404–1415, May 2015. [Online]. Available: <http://ieeexplore.ieee.org/document/7005453/> [Accessed: 2018-04-06]
- [31] A. Ataollahi, R. Karim, A. S. Fallah, K. Rhode, R. Razavi, L. Seneviratne, T. Schaeffter, and K. Althoefer, “3-DOF MR-Compatible Multi-Segment Cardiac Catheter Steering Mechanism,” *IEEE Transactions on Biomedical Engineering*, no. 99, Nov 2015. [Online]. Available: <http://ieeexplore.ieee.org/document/6575109/> [Accessed: 2018-04-06]
- [32] T. Cooper, C. Julian, and S. J. Blumenkranz, “Adaptor for a medical instrument,” Patent USD441 076 S1, 1998. [Online]. Available: <http://www.google.com/patents/USD441076> [Accessed: 2018-04-06]
- [33] “Catheter Robotics – Other Resources.” [Online]. Available: <http://catheterrobotics.com/product-main.htm> [Accessed: 2018-04-06]
- [34] “Stereotaxis Vdrive system.” [Online]. Available: <http://www.stereotaxis.com/products/vdrive/> [Accessed: 2018-04-06]
- [35] H. A. Jaeger, P. Nardelli, C. O’Shea, J. Tugwell, K. A. Khan, T. Power, M. O’Shea, M. P. Kennedy, and P. Cantillon-Murphy, “Automated Catheter Navigation with Electromagnetic Image Guidance,” *IEEE Transactions on Biomedical Engineering*, pp. 1972 – 1979, 2017. [Online]. Available: <http://ieeexplore.ieee.org/document/7866849/> [Accessed: 2018-04-06]
- [36] “Olympus -BF-XT160| Medical Systems.” [Online]. Avail-

- able: https://www.olympus-europa.com/medical/en/medical_systems/products_services/product_details/product_details.jsp?product_id=5955 [Accessed: 2018-04-06]
- [37] “Pulmonology | PENTAX Medical (EMEA).” [Online]. Available: <https://www.pentaxmedical.com/pentax/en/95/1/70K-Series-Video-Bronchoscopes> [Accessed: 2018-04-06]
- [38] “EB-530XT | Fujifilm Europe.” [Online]. Available: <https://www.fujifilm.eu/eu/products/medical-systems/endoscopy/endoscopy-products/p/eb-530xt#specifications> [Accessed: 2018-04-06]
- [39] P. Cantillon-Murphy and H. A. Jaeger, “OSF | Anser EMT.” [Online]. Available: <https://osf.io/47q8q/> [Accessed: 2018-04-06]
- [40] “Medical » Aurora Tools and Sensors, and Accessories.” [Online]. Available: <http://www.ndigital.com/medical/products/tools-and-sensors/> [Accessed: 2018-04-06]
- [41] “ASM Material Data Sheet.” [Online]. Available: <http://asm.matweb.com/search/SpecificMaterial.asp?bassnum=mq304a> [Accessed: 2018-04-06]
- [42] “Pololu - DRV8825 Stepper Motor Driver Carrier, High Current.” [Online]. Available: <https://www.pololu.com/product/2133> [Accessed: 2018-04-06]
- [43] “LM117, LM317-N Wide Temperature Three-Pin Adjustable Regulator.” [Online]. Available: <http://www.ti.com/lit/ds/symlink/lm117.pdf> [Accessed: 2018-04-06]
- [44] “CloudCompareWiki.” [Online]. Available: http://www.cloudcompare.org/doc/wiki/index.php?title>Main_Page [Accessed: 2018-07-03]